AN ANALYSIS OF SOUTHERN GREAT PLAINS ARM CLOUDINESS AND SURFACE RADIATION DATA

by Robert C. Levy

David A. Randall, Principal Investigator

Colorado State University

DEPARTMENT OF ATMOSPHERIC SCIENCE

PAPER NO. **627**

AN ANALYSIS OF SOUTHERN GREAT PLAINS ARM CLOUDINESS AND SURFACE RADIATION DATA

by

Robert C. Levy

Research supported by the
U.S. Department of Energy
under Grant number DE-FG03-95ER61968
and by the Office of Naval Research
under Contract number N00014-91-J-1422

Department of Atmospheric Science
Colorado State University
Fort Collins, CO

December 1996

Atmospheric Science Paper No. 627

Abstract

AN ANALYSIS OF SOUTHERN GREAT PLAINS ARM CLOUDINESS AND SURFACE RADIATION DATA

One scientific question that the ARM (Atmospheric Radiation Measurement) program hopes to answer is, "What are the direct effects of temperature and atmospheric constituents, primarily clouds, water vapor and aerosols on the radiative flow of energy through the atmosphere and across Earth's surface?" (ARM Science Team, 1996). The purpose of this project is to construct a detailed analysis of the clouds over the Central Great Plains (SGP) site and to study their effects on surface radiation. Using data from the October/November 1994 Intense Observation Period at the Central Facility (CF), "composite" daily time series plots have been made, relating cloud levels (cloud base and cloud top), liquid and precipitable water amounts, and the downwelling solar and infrared irradiances. From these pictures interesting time periods were selected, such as periods of completely clear skies, nearly uniform single-layer clouds, or multi-layered clouds. For each of these periods, one-hour "averages" or "characteristic values" of CF data were computed to run the CSU GCM (Colorado State University General Circulation Model) radiation parameterization, and modeled flux results were compared with solar and infrared fluxes observed at the CF.

Data were grouped into "cloud" and "clear" cases, depending on whether or not a ground-based micro-pulse lidar detected clouds during the one-hour interval. For clear cases, the parameterization needed vertical water vapor, ozone, and carbon dioxide profiles. For cloud cases, additional inputs included cloud fraction and ice/water mixing ratios in cloud layers. The water and ice profiles were obtained using lidar and sounding estimates of cloud base and top (pressure and temperature), along with microwave radiometer estimates of liquid water path and climatological values of cloud ice content. Statistics were used to determine whether the clouds present were one layer or multi-layer.

Under clear skies, the resulting modeled downwelling solar fluxes were about 10% larger than observed. The longwave fluxes agreed well with observations, although the simulated downwelling longwave was consistently too low, and the simulated outgoing (top of atmosphere) longwave was too high. For one-layer cloudy sky cases, the trends were similar to the clear sky cases. That is, the solar fluxes were calculated higher than observed, the downwelling fluxes were generally modeled too low and the outgoing longwave was generally too high. However, the errors for individual calculations were much larger, likely due to the uncertainty of cloud base and top, the assumptions used in distributing the liquid and ice in the cloud, the values of cloud particle optical parameters used in the model runs, and the simplified physics used in the parameterization itself.

Acknowledgments

First, I would like to thank my advisor, Dr. David Randall, for all his help and encouragement. He expected realistic progress and patiently answered my questions (or suggested where I might look for answers). We also had honest coversations about the atmospheric science field, about our past east coast lives, and about the future.

Thanks goes to my committee members, Drs. Bill Cotton and Jorge Ramirez. They gave me substantial comments on my thesis drafts, as well as substantial advice about the world outside CSU.

Without help from group members Doug Cripe, Scott Denning, and Cindy Carrick, I would never learned how to use the ARM data, write this document or deal with CSU deadlines. Kelley Wittmeyer made my computer invincible; Don Dazlich, the "GCM Guru," answered my programming and parameterization questions; and Laura Fowler helped me with the cloud optical parameter subroutines. Office-mates Mike Kelly and Cara-lyn Lappen were always willing to answer questions and entertain me.

I am grateful for all the help I received from members of the ARM program. Ric Cederwall, Jim Liljegren, and Marty Leach provided invaluable assistance with each dataset, and answered questions sometimes on a minute's notice (via e-mail). Jim Teske provided me an enjoyable and complete tour of the ARM Central Facility.

Finally, I want to thank my friends and family for being there and supporting me, especially when my self-confidence was down (as my phone bill will confirm). Thanks goes to the disc players on the Village Idiots, Sluggo, and Fat Chance for letting me burn off stress with them. And last but not least I want to thank Mother Nature for making my last two years in Colorado a very pleasant experience.

This work was supported by the Office of Naval Research, Contract N00014-91-J-1422, and by the U.S. Department of Energy, Grant DE-FG03-95ER61968.

Table of Contents

List of Figures

List of Tables

CHAPTER 1

Introduction

The Earth's climate system is sensitive to changes in the radiation budget (solar-shortwave and earth/atmosphere-infrared). Results from General Circulation Models (GCMs) suggest that a mere 4 W m^{-2} change (about 1%) of radiation flux at the tropopause is capable of dramatically changing Earth's present climate. Current radiation measurements are precise only to tens of Watts per square meter, and so are not adequate for climate studies. Models have also shown that the radiation budget and clouds are very closely linked, and have complicated positive and negative feedbacks, but neither the magnitude nor direction of these feedbacks are well known (ARM, 1996).

The Atmospheric Radiation Measurement (ARM) Program is a Department of Energy supported program, created to better understand and model the processes and properties which affect atmospheric radiation. One of ARM's top priorities is obtaining detailed and continuous observations, for use in GCMs and parameterizations, of the atmospheric constituents which could affect radiation (ARM, 1996). Instrumentation within each cloud and radiation test bed (CART) provide nearly continuous observations, over many years, of variables including: surface and upper air meteorology (temperature, wind, humidity, pressure), cloud properties (base, top, optical depths, composition), liquid and vapor water column amounts, spectral and directional radiative fluxes (up/down, short/long/IR, direct/diffuse), aerosol, ozone, and other variables. Satellite and airborne instruments complement the ground-based instruments. During an Intensive Observation Period

(IOP), the CART site provides additional observations that would be too expensive or too personnel-intensive to be provided normally. ARM has selected three CART sites, based on climatology, topographical homogeneity, accessibility, and synergism with other atmospheric measurement projects. The first operational CART is the Southern Great Plains site (SGP-CART), which straddles the Kansas-Oklahoma border. The SGP-CART's Central Facility, (located near Lamont, OK), is where the highest concentration of observations are taken.

This report work used data observed at the SGP-CART Central Facility during the IOP from 24 October to 14 November 1994. Goals for this project include:

- Develop a composite "picture" of the atmosphere during this ARM IOP;
- Use data from specific time intervals of the IOP, to test a simple radiation parameterization;
- Identify key relations between cloud properties and atmospheric radiation.

This report is divided into nine chapters. In chapter 2, the scientific background to this project, including discussions of radiation and cloud processes in the atmosphere is introduced. Details of the ARM project, instruments and data are found in Chapters 3 through 6. The CSU GCM radiation parameterization, and results obtained by feeding ARM data through the parameterization are discussed in Chapters 7 and 8. A summary and conclusions are found in Chapter 9.

CHAPTER 2

Scientific Background

2.1 Radiation

Observations of the earth's mean temperature have shown that the earth is neither greatly heating or cooling. In order to maintain this state of quasi-equilibrium, the amount of energy absorbed from external sources must balance emitted energy from the earth. Two important types of radiation are solar radiation and terrestrial radiation. Because the sun is much hotter than the earth, it radiates mostly in the "shortwave" spectral region at wavelengths between 0.2 μm and 4 μm, while the cooler earth emits mostly at wavelengths longer than 4 μm. Thus we can treat the sun's and the earth's radiation as separate entities to simplify the discussion.

Nearly all energy received at the top of the atmosphere originates from the sun, but it is then partially scattered, partially absorbed and partially reflected by the material in the atmosphere by the time it reaches the surface. The remainder that reaches the surface is then partially scattered, partially absorbed and partially reflected by the material (gases, hydrometeors and aerosols) on the surface. By the first law of thermodynamics, any energy absorbed can be transformed into heat or converted to kinetic or potential energy.

Because the solar radiation comes from a distant point-like source (the sun), it can be treated as parallel, unidirectional radiation. However, the terrestrial radiation comes from all directions, because each molecule (on the surface and in the atmosphere) is essentially a point-like source.

A black body is defined as a radiating object that is a perfect absorber and emitter of radiation. In other words, all energy incident upon it will be absorbed, and it will emit the maximum possible energy at its given temperature. A combination of "laws" relate radiation intensities and fluxes to the absolute temperature of the radiating object, and the absorptivity, reflexivity and transmissivity of the material between the radiating object and the collecting object. These include Planck's Law, the Stefan-Boltzmann Law, the Wein Displacement Law, Kirchoff's Law, and the Beer-Bouger-Lambert Law.

2.1.1 Solar Radiation

Most solar radiation is found in the ultraviolet, visible and near infrared regions (between 0.15 and 4 μm). Long-term observations show that the intensity of solar radiation received at the top of the atmosphere is nearly constant, approximately 1367 Wm^{-2}, and spectrally resembles a blackbody with a temperature about 5800 Kelvin.

The 1367 Wm^{-2} received at the top of the atmosphere, normal to the radiation beam, is called the *solar constant*, although in actuality it varies by about 10%, due to the elliptical orbit of the earth, and the very small day-to-day variations of the sun's output. The flux received on a horizontal surface, tangent to the top of the atmosphere, is called the *solar insolation*, and is calculated by multiplying the solar constant by the cosine of the *solar zenith angle* (angle of the sun from the vertical). The solar zenith angle is in turn dependent on the *latitude* on earth, the *declination* (seasonal tilt) of the earth, and a factor called the *hour angle*, which is based on the time difference between local time and local noon. These concepts can be summarized in the equation:

$$F_{SW} = Q_0 \left(\frac{d_m}{d}\right) cosZ, \tag{2.1}$$

where F_{sw} is the solar insolation, Q_O is the Solar Constant, d_m is the earth-sun mean distance, d is the actual earth-sun distance, and Z is the solar zenith angle, related by the equation

$$cosZ = sin\phi \, sin\delta + cos\phi \, cos\delta \, cosh, \tag{2.2}$$

where ϕ is the latitude, δ is the solar declination, and h is the hour angle.

As solar radiation comes down through the earth's atmosphere, it is scattered and absorbed by gases, aerosols and hydrometeors. Each type of material has to be treated differently when modeling the extinction (absorption + scattering) of solar radiation.The main atmospheric gases absorbing solar energy are water vapor, carbon dioxide, and ozone, and oxygen; nitrogen and nitrogen oxides are less absorptive. The radiation coming directly from the sun, received at earth's surface, normal to the sunbeam, is called the *direct normal* solar radiation. By multiplying this direct normal radiation by *cosZ*, cosine of the zenith angle (in essence, aligning the collecting surface so that it is horizontal with respect to the earth's surface or laying the collecting surface on the ground), we obtain *direct* solar radiation. The scattered radiation from all angles is called the *diffuse* solar radiation, and the sum of the direct and the diffuse radiation is called the *global* or *total hemispheric* solar radiation (see Fig 2.1).

Once the radiation reaches the surface, a percentage of it is reflected back into the atmosphere. The percentage of the total incoming solar that is reflected, called the *albedo*, is affected by the nature of the surface (roughness, vegetation type and color, snow cover, etc.) and the solar zenith angle. It turns out that the average albedo of the earth's surface is about 15%, whereas the planetary albedo (including the atmosphere and the surface) is

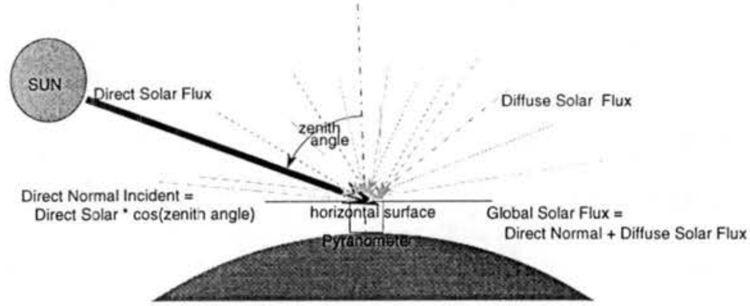

FIGURE 2.1: Diagram of the Different Components of Downward Solar Flux

about 30%. These average values are highly variable, however. For example, the albedos of clouds range from 20% -30% for thin cirrus or stratus, to over 70% for thick nimbostratus or cumulonimbus. The surface albedos range from 2% for a noon-time water surface, to over 95% for a fresh snowfield in late afternoon.

2.1.2 Terrestrial Radiation

Wien's displacement law implies that the cool earth emits the bulk of its radiation in the longwave spectral (wavelengths greater than 4 μm) region. To fit the observed radiation near-balance of the earth, the amount of solar radiation absorbed by the planet must equal the amount of terrestrial radiation emitted back to space. Measured emissivities at the surface are on the order of 0.92-0.98. So, although the earths's surface is not a real black-body (emissivity = 1), for most simple calculations the earth may be assumed to act as one.

All constituents of the atmosphere are selective of the wavelengths of energy that they absorb and re-emit. For example, water vapor acts nearly as a black body at some wavelengths, while at other wavelengths it is completely transparent (unaffected) by the radiation. At still other wavelengths, it absorbs/emits a percentage of the radiation. For solids and liquids, the variation of emissivity with wavelength is small, while for gases, the variation is large. Atomic gases absorb and emit radiant energy in *spectral absorption* *lines*, narrow distinct wavelength intervals resulting from quantized changes in electronic state. Molecular gases absorb and emit radiant energy in *spectral absorption bands*, each one formed by a collection of side-by-side lines. The locations of the lines and bands in the continuous spectrum are thus a superposition of all the gases in the atmosphere.

Absorption and emission of radiation by a gas occurs at specific wavelengths according to its atomic and molecular structure, and only at discrete energy states of the gas. Quantum mechanics predicts that the interaction of a gas with radiation can take place only at well-defined frequencies characteristic of a molecule, analogous to a harmonic oscillator having a "natural" period of oscillation. It turns out that the molecular or atomic structure of the gas governs the spectral distribution of the lines and bands.

The spectral lines in the emission (absorption) spectrum of an isolated molecule have a very small, but finite frequency width, due to the Heisenberg Uncertainty Principle (stating the impossibility of simultaneously obtaining exact measurements of both the position and velocity of a particle). The exact location of spectral lines are therefore "fuzzy," so a spectral line at a discrete frequency is governed by a probability distribution function. This fuzzyness, called *line broadening*, is increased when molecules collide, dependent on the rate at which collisions take place, the number of the molecules, the mean molecular speed (proportional to the square root of temperature), and the atmospheric pressure. In thermodynamic terms, the broadening is proportional to the product $p/T^{0.5}$ and so it is more affected by the pressure than the temperature. Thus this phenomena is called *pressure broadening* (see Goody and Yung, 1989). Other factors influence line broadening, but they are negligible compared to the pressure broadening effect in the troposphere.

The most commonly used model for the shape of the probability function of the spectral line is the Lorentz line shape model (see Fig 2.2):

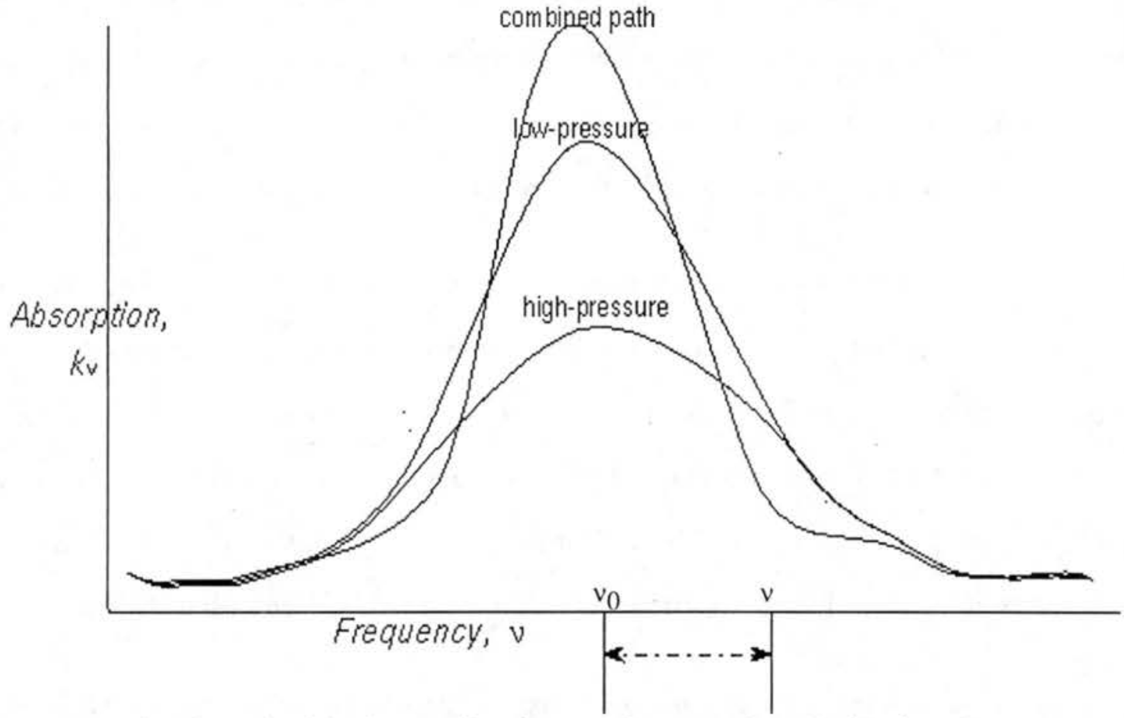

FIGURE 2.2: A schematic of the Lorentz line shape and pressure broadening, for a low-pressure path, a high pressure path, and the combination of both paths.

$$k_\nu = \frac{S}{\pi}\left(\frac{\alpha}{(\nu-\nu_0)^2+\alpha^2}\right), \tag{2.3}$$

where k_ν is an *absorption coefficient*, S is a characteristic *line intensity*, ν_0 is the central (most probable) frequency of the line, and α is a *half-width*. The half-width is one-half the distance between the two frequencies where $k_\nu = k_{\nu,0}/2$ (one half that of the coefficient at the center of the line). The half-width of the line is directly proportional to the pressure and inversely proportional to the square root of the temperature:

$$\alpha = \alpha_0\left(\frac{p}{p_o}\right)\left(\frac{T_o}{T}\right)^{1/2}, \tag{2.4}$$

where p_0 and T_0 are a standard temperature and pressure. Therefore, the transmission of a wavelength, ν, between two levels, through a substance with a characteristic absorption coefficient k_ν, scaled (by pressure and temperature) optical path $\overline{u}$, and diffusivity factor $\beta = 1.66$ (to convert radiance to flux), is given by (Goody and Yung, 1989)

$$T_\nu^{flux}(p_1,p_2) = exp(-\beta k_\nu \tilde{u}) . \quad (2.5)$$

In theory then, all one would have to do to calculate total fluxes would be to multiply this transmission function by the Blackbody Planck function, integrate over all pressure layers, and finally integrate over all wavelengths (see Fig 2.3):

$$F^{up}(p) = \int_\nu \left[B_\nu(T_{sfc}) T_\nu(p,p_{sfc}) + \int_{psfc}^{p} B_\nu(T_{p'}) \frac{dT_\nu(p,p')}{dp'} dp' \right] d\nu , \quad (2.6)$$

and

$$F^{down}(p) = \int_\nu \left[\int_0^p B_\nu(T_{p'}) \frac{dT_\nu(p',0)}{dp'} dp' \right] d\nu . \quad (2.7)$$

Net flux at a level p is be given by

$$F^{net}(p) = F^{up}(p) - F^{down}(p) , \quad (2.8)$$

and the heating in a layer is given by

$$\frac{dT}{dt} = \frac{g}{C_p} \frac{d}{dp} (F^{net}(p)) , \quad (2.9)$$

where g is gravity (9.81 m s^{-2}), C_p is the specific heat at constant pressure, $B_\nu(T_p)$ is the Planck function of wavelength ν at temperature T (at pressure p), and $T_\nu(p_1, p_2)$ is the transmission between two pressure levels (see Fig 2.3).

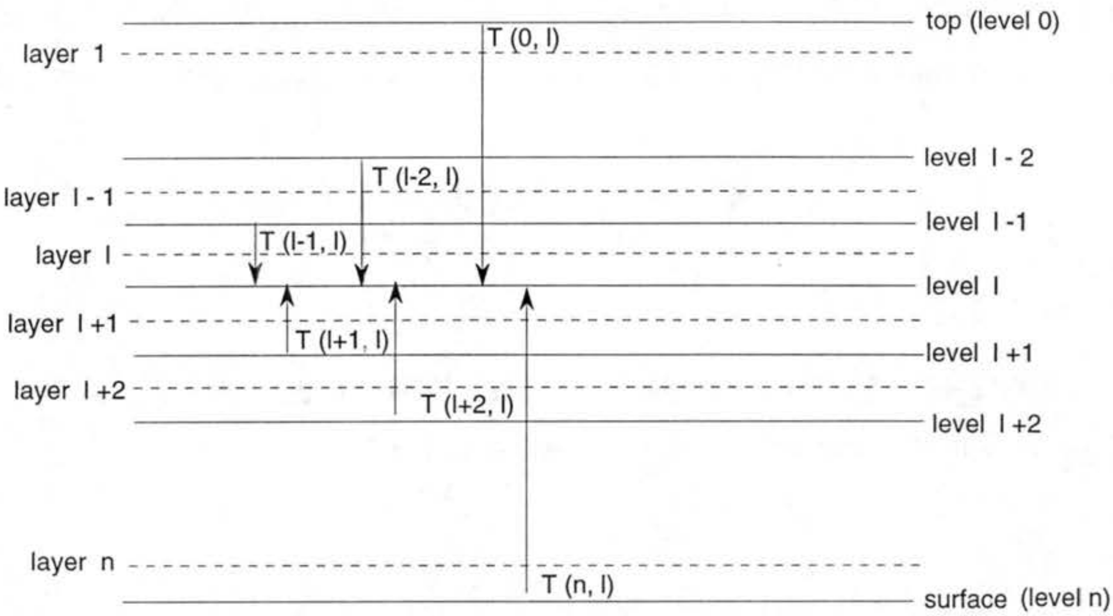

FIGURE 2.3: Schematic of Radiative Transfer in the atmosphere. F_up is the sum of all the upward pointing arrows and F_down is the sum of all the downward pointing arrows. Note that T*(p', p)* represents the Transmission function from pressure p' to pressure *p*, for a particular wavelength ν.

Unfortunately, the spectral bands of the various atmospheric transmitters (absorbers) are irregularly distributed, meaning that the Lorentz line is only an approximate form. Moreover, the complete radiation spectrum contains infinitely many Lorentz emission lines with widely varying absorption coefficients, meaning the transmission can not be numerically solved. Therefore, if we want to model the transmission over the whole atmospheric radiation spectrum, using a reasonable computational effort, we must split up the spectrum into *bands* and describe some sort of characteristic absorption coefficient and optical path for each band. For example, the parameterization in the CSU GCM splits up the infrared spectrum into four bands: two for H_2O, and one each for CO_2 and ozone (Harshvardhan et al., 1987). Details may be found later in chapter 6.

2.2 Clouds

When looking from a satellite, the most distinctive feature of the earth is its cloud cover. Clouds cover half of the globe and have high albedos. Clouds in the atmosphere have a profound effect on both the solar and the terrestrial radiation, yet individual cloud effects vary due to differences in formation, level, composition, temperature, and horizontal placement.

Clouds form in the presence of many types of meteorological phenomena. Local ascent of warm buoyant air parcels in a conditionally unstable environment produces *convective clouds*, having diameters from 0.1 to 10 km and vertical updraft velocities on the order of 1-50 meters per second. These clouds have high water or water and ice contents, (0.1 to 1 g m^{-3} for small cumulus and up to 20 g m^{-3} for severe cumulonimbus), and have lifetimes of minutes to hours. Forced lifting of stable air produces *layer clouds*, having diameters of 10 to 100 km or more and found at every level of the atmosphere. These layer clouds have small water or water/ice contents (0.001 - 0.1 g m^{-3})and lifetimes of many hours. *Orographic clouds* are formed when air is forced to ascend over a mountain, and have variable updraft velocities, water contents, and lifetimes. Finally, *fog* can be produced by radiative cooling of the surface below its dewpoint or when warm air moves over cold surfaces. Fogs usually have extremely low water contents and updraft velocities, and have variable lifetimes (Wallace and Hobbs, 1977).

Clouds can form at all levels of the troposphere, so that they have various temperatures and compositions, thus controlling the radiative effects. Clouds are sometimes grouped into "low" (below 2 km) "middle" (2 km to 6 km) and "high" (above 6 km). Depending on the formation process and level, the cloud may be all liquid water, all ice, or a combination of both. Liquid water and ice particles interact differently with radiation due to the size and shape of the particles. Obviously, temperature affects radiation due to the Planck and Stefan-Boltzmann functions ($F = \sigma T^4$). Pressure differences between layers act to "scale" the transmission through a cloud.

Finally, the horizontal placement of the cloud has major, but relatively unknown effects on the radiation. The same type of cloud covering a spot in the sky has very different radiative profile than a cloud covering the whole sky. Even two skies with the same "cloud fraction" can be radiatively different depending on how the clouds are distributed. For multilevel clouds, large radiation differences can be measured, depending on the degree of cloud overlap.

Classification of the radiative effects of clouds is a very difficult problem. Usually, the problem is considered to have two parts: the radiative effects caused by the *extrinsic* (macrophysical) properties of the cloud's position in space and the effects caused by the *intrinsic* (microphysical) properties of the individual cloud particles.

2.2.1 Extrinsic (Macrophysical) Optical Properties

For the longwave radiative transfer problem, the most dominant influence by clouds is through the contrast between the radiation received from above and below the cloud to the radiation emitted by the cloud. Unlike for the clear sky (which is dominated by band absorption by gases), the cloudy sky is dominated by the spectral window bands not absorbed by gases. The net longwave budget of a cloud is the difference between emission from cloud top (cooling) and cloud-base absorption of the flux from below (warming). This difference changes sign as the cloud altitude changes, i.e., a low cloud acts to cool the atmospheric column, while a high cloud warms the column. An analogy is a person (atmosphere - warm) sleeping on a bed with a blanket (cloud) in a cold room (space). If the person sleeps on top of the blanket, he emits to the room and gets cold. However, if he is covered by a blanket, the effect is to keep him warm. The thicker the blanket, the warmer he sleeps. He can adjust his sweat/shiver ratio by partially covering himself with the blanket (adjusting the fractional cover of the cloud).

2.2.2 Intrinsic (Microphysical) Optical Properties

Cloud particles are similar in size to infrared wavelengths; thus the effects of particle size and shape on infrared radiation are generally assumed to be negligible. This assumption is quite false for high thin clouds, yet it is often assumed anyway (Stephens, 1984).

Ignoring at first the effects of scattering, the grey body assumption (spectrally flat absorption and reflection for all infrared, IR, wavelengths) is a good approximation. This means that the IR optical depth of a cloud is only a function of the liquid water path, i.e. $\tau = kW$, where k is an absorption coefficient and W is the *liquid (or ice) water path*, analogous to the water vapor path, u, discussed above. Therefore the flux emissivity would be

$$\varepsilon = 1 - exp(-\beta k W) , \tag{2.10}$$

where $\beta = 1.66$ is the flux diffusivity coefficient.

The influence of cloud intrinsic optical properties is much more complicated for solar radiation transfer because scattering effects can not be ignored. The *effective radius* r_e of a cloud particle is,

$$r_e = \frac{V}{A}, \tag{2.11}$$

where V is the volume of the water in the cloud and A is total cross-sectional area of the particles. The optical depth of a cloud is estimated by

$$\tau \sim \frac{3W}{2r_e} \tag{2.12}$$

(Stephens, 1978, 1984). This means that for two clouds with the same liquid water path, the one with the smaller particles has the larger optical depth.

The *single-scatter albedo*, ω_0, is a measure of the reflectivity of a single cloud particle, that is, the ratio of scattering to total extinction. A value of 1 means all radiation is scattered, while a value of 0 means all radiation is absorbed by the particle. Values of ω_0 ~ 0.99 (see Figure 2.4) are typical for most cloud particles at wavelengths less than 1.5

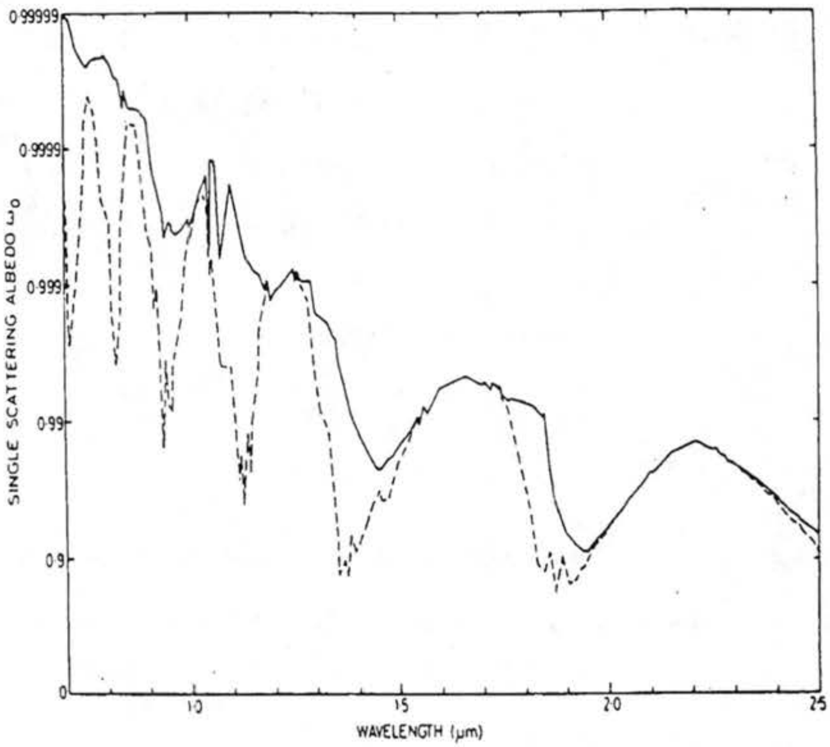

FIGURE 2.4: Typical values of the single-scatter albedo ω_0 of a model cloud as a function of wavelength. The solid line refers to droplet absorption along while the dashed line refers to droplet plus vapor absorption (in Stephens, 1984, adopted from Twomey and Seton, 1980)

μm. The *asymmetry parameter*, g, describes the ratio of forward scatter to backscatter, so that a value of 1 means that a particle scatters all light forward, $g = 0$ means a particle scatters symmetrically and $g = -1$ means all light is backscattered. It turns out that larger particles scatter more light forward, and a typical value for 10 μm cloud particles is $g \sim 0.85$ (see Figure 2.5) at solar wavelengths. The "diffuseness" factor D, estimates the effective extra path length a diffuse radiation field travels versus a direct field.

We may relate these cloud optical parameters to solar transfer by considering limits as cloud optical depth τ varies between 0 and ∞. The albedo (reflectivity) of a cloud de-

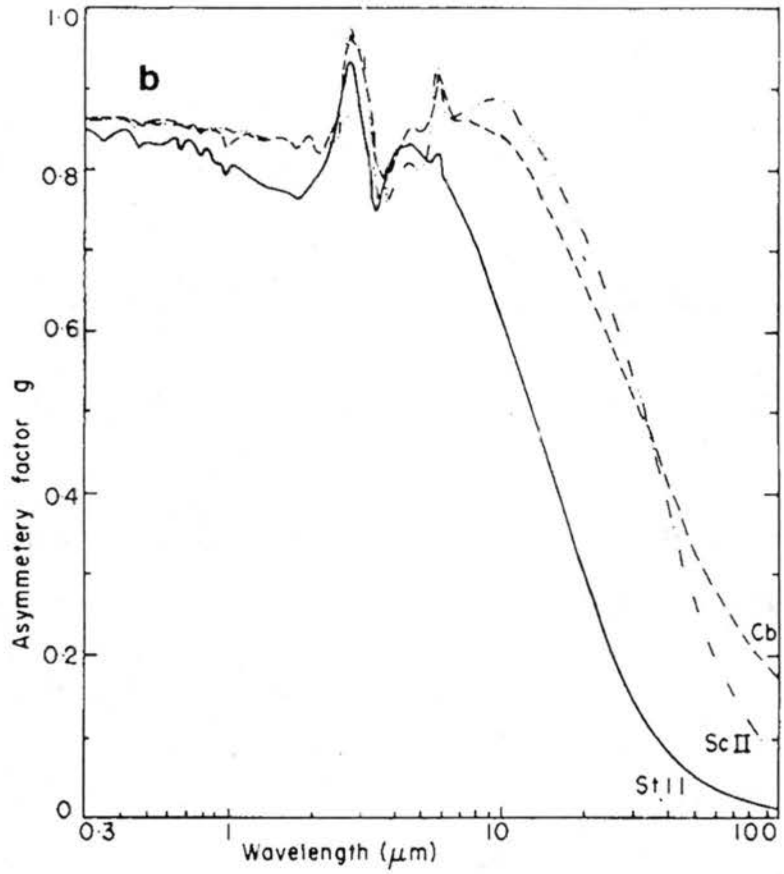

FIGURE 2.5: Typical values of the asymmetry parameter, g, for three types of model clouds, Stratus, Strato-cumulus and Cumulo-nimbus. (from Stephens, 1984)

pends on the single-scatter albedo ω_0, the *backscatter efficiency*, b, (given by $b = (1\text{-}g)/2$), the diffusivity, D, and the cosine of the solar zenith angle μ_0:

$$R = R(\omega_0, b(g), D, \mu_0) \; . \qquad \textbf{(2.13)}$$

For optically thick clouds ($\tau \rightarrow \infty$),

$$R_\infty = 1 - A_\infty , \qquad \textbf{(2.14)}$$

because nearly all flux that is not absorbed by the cloud can be assumed to be reflected. Characteristic combinations of effective particle radius and water path are 0.1 μm and

0.2 mm, respectively, to categorize a cloud as "optically thick." For these clouds, absorption depends mostly on the single scatter albedo and can be shown to asymptotically approach

$$A_{\infty} \approx const \times (1 - \omega_0)^{0.4}, \tag{2.15}$$

and transmission through the cloud becomes negligible; i.e., as $\tau \rightarrow \infty$,

$$T_{\infty} \rightarrow 0. \tag{2.16}$$

For thin clouds ($\tau^* \rightarrow 0$), forward scattering is important, so we need the asymmetry parameter and the solar zenith angle in our calculations:

$$A_0 = \frac{\tau}{\mu_0}(1 - \omega_0), \tag{2.17}$$

$$R_0 = \frac{\tau}{\mu_0} b\omega_0 \tag{2.18}$$

and

$$T_0 = \frac{\tau}{\mu_0}(1 - f\omega_0); \tag{2.19}$$

where f is the *forward scatter efficiency* given by $f = (1+g)/2$. Thus, both the albedo and absorption of thin clouds vary linearly with optical thickness, along with the backscatter and absorption properties of the individual cloud particles.

CHAPTER 3

Atmospheric Radiation Measurement Program (ARM)

3.1 ARM - Objectives

Climate modelers need to accurately parameterize subgrid phenomena, specifically the transfer of radiation within the atmosphere and the processes which govern cloud formation, composition and dissipation. Accurate cloud and radiation observations, over an area comparable to a GCM grid-box or a SCM (Single Column Model), are needed to test these parameterizations. With these objectives in mind, the Department of Energy assembled a comprehensive program, known as ARM:

> "The Atmospheric Radiation Measurement (ARM) Program is a major program of atmospheric measurement and modeling intended to improve understanding of the processes and properties that affect atmospheric radiation, with a particular focus on the influence of clouds and the role of cloud radiative feedback" (Stokes and Schwartz, 1994).

The main goals of ARM are (Stokes and Schwartz, 1994):

1) to relate radiative fluxes in the atmosphere, spectrally resolved and as a function of position and time, to the atmospheric temperature, composition (specifically water vapor and clouds) and surface radiation properties; and

2) to develop and test parameterizations that describe water vapor, clouds and the surface properties governing atmospheric radiation, with the objective of incorporating these parameterizations into general circulation and related models.

The research components of ARM, including the development and testing of the instrumentation and parameterizations, are the duties of the ARM Science Team. Specifically, the Science Team is made up of 50 research groups, split into three main categories: 1) The "modelers" - to develop and test the parameterizations, 2) the "inventors" - to develop and test instruments suitable for future deployment, 3) and the "field scientists" - to oversee data collection and quality at the site. To meet the data requirements of the Science Team members, the Cloud and Radiation Testbed (CART) is designed to collect continuous, long-term and detailed field observations of radiation and cloud properties over an area comparable to the size of a GCM gridbox.

3.2 The CART and IOPs

The CART was designed to meet the observational needs of the Science Team. The choices of the CART sites were made in light of several radiation influencing factors, such as latitude/longitude, altitude, terrain, clouds, precipitation, temperature and humidity. Additional criteria for CART sites were: large temporal weather variability, homogeneity of terrain within the gridbox-size area, accessible but un-influenced by urban environments (i.e. the region should supply roads, power, communications, and living accommodations, but not be negatively influenced by urban-generated climate factors), and proximity to other measurement projects in the area (Cripe, 1994). The ARM program decided on three CART sites:

- The Southern Great Plains (SGP) Site,
- The Tropical Western Pacific (TWP) Site,
- The North Slope of Alaska/Adjacent Arctic Ocean (NSA/AAO) Site.

ARM will collect data at each site over a period of years, in order to capture interesting or extreme phenomena and to build up the statistics of an "Atmospheric Radiation Climatology" for each site (ARM Science Team, 1995). Other reasons for extended observations include: better inter-comparison and calibration between instruments, better incentive to purchase and develop more accurate and expensive instruments, higher probability of getting "good" data sets, and more time to tackle problems as they arise.

Because data will be collected over a long time, quasi-permanent facilities are needed, including provisions for power, living accommodations, etc. Also, some types of instruments may be too expensive to operate continuously, and so Intensive Operating Periods (IOPs) are necessary.

3.3 The SGP-CART

Currently, only the SGP-CART (Southern Great Plains-CART) is operational. This site, centered near the town of Lamont, OK (36° 36'N, 97° 29'W, 320 meters above sea level), occupies a 365 km by 300 km box covering much of south-central Kansas and north-central Oklahoma. The SGP meets the Science Team's characteristics for climate, homogeneity, accessibility, and collaborative projects in the region. Due to its continental climate influences, the region experiences highly variable temperature, cloudiness, and precipitation. The terrain is spatially homogenous, that is, not broken up with mountains or coastlines. There are roads and other "civilized" structures in the area, yet it is not highly populated. Finally, the area is well served by wind profilers, NEXRAD, the Global Energy and Water Cycle Experiment (GEWEX) and other projects that increase the data coverage.

The SGP-CART site (Figure 3.1) consists of a central facility, an auxiliary station network, an extended observation network and boundary facilities. Because the central facility aims to construct as detailed a characterization of the atmospheric column as possible, and is the "center" of the column, it collects more data than any of the other facilities. These data include measurements of upwelling and downwelling spectrally analyzed radiances, cloud base height, cloud fraction and cloud optical properties, liquid and vapor water paths, aerosols and gaseous composition, surface and eddy energy fluxes, and standard meteorological parameters at the surface and upper atmosphere (temperature, wind, humidity, etc., from ground-based and balloon-borne instruments). The auxiliary, extended and boundary facilities collect additional data to three-dimensionalize the atmospheric column.

3.3.1 My Personal Experience at the ARM-SGP

FIGURE 3.3: Yes, that is the author at the SGP site!

During the summer of 1995, I had the privilege of visiting the SGP-site near Lamont, Oklahoma. I toured the site, attaining an understanding of the instrumentation (like what

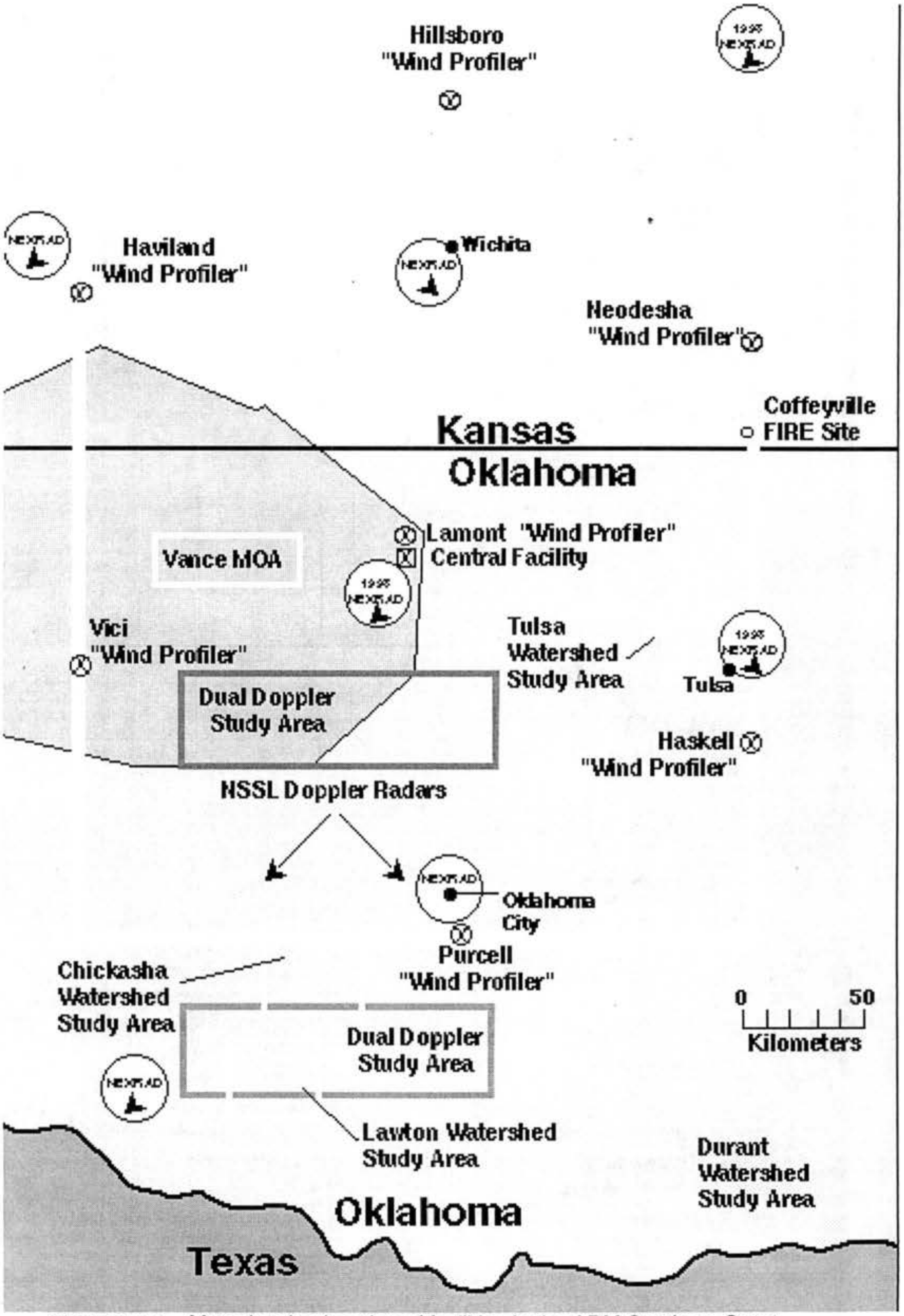

FIGURE 3.1: Map showing location of facilities in the ARM Southern Great Plains CART site (from ARM web page)

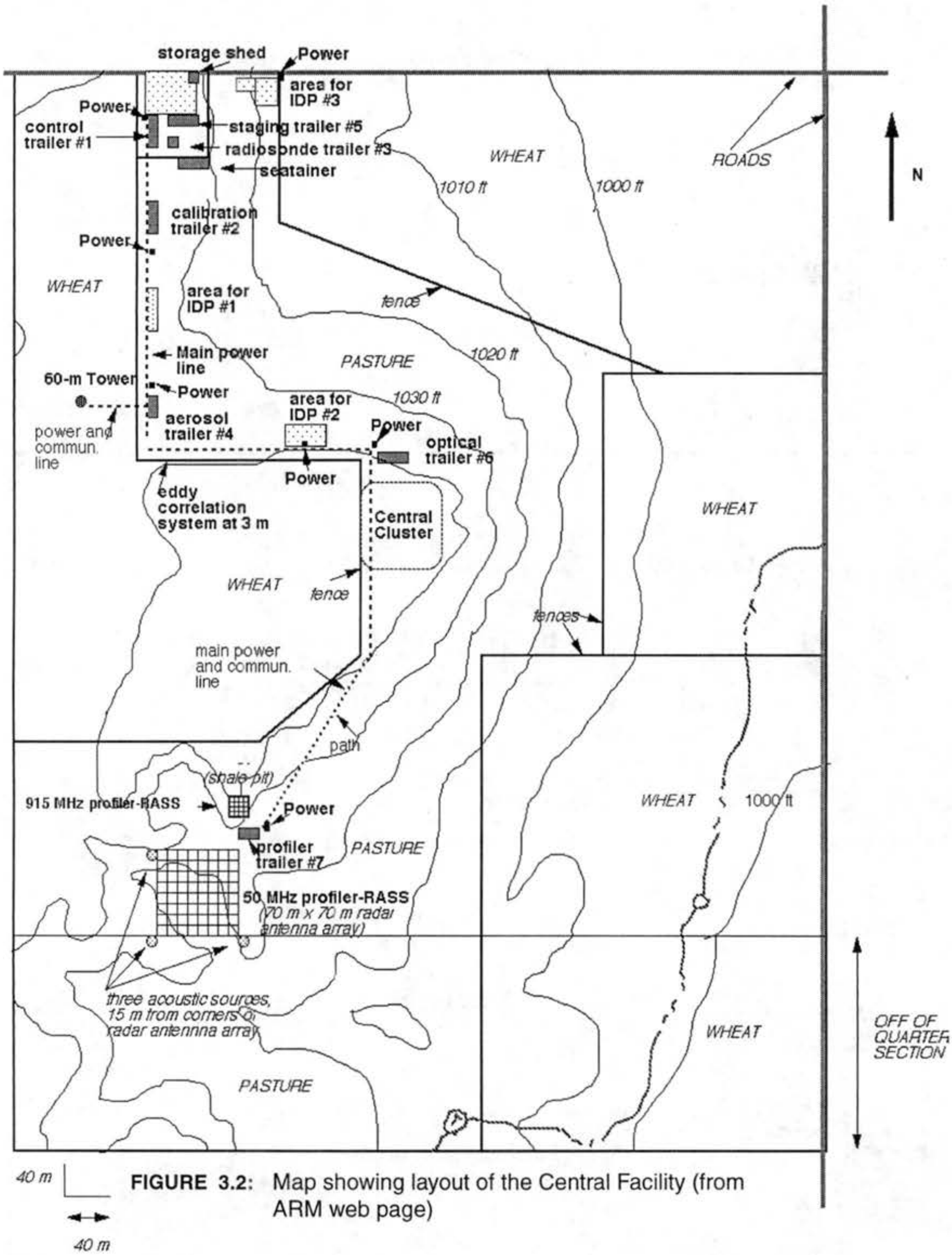

FIGURE 3.2: Map showing layout of the Central Facility (from ARM web page)

a radiometer looked like and how it worked) and of the general layout of the site (that it was farmland, in the middle of cow-grazing pasture). I also launched radiosondes, and helped take down and take apart the 10 meter tower (lightning struck the site the day before I arrived, wreaking havoc over one of the radiometer systems).

But the real value in this visit was the resulting more sober view I had of the data and data collection. As I mentioned before, lightning struck the 10-meter tower, thereby knocking out all the radiometers connected (in parallel) to the SIROS system, as well as the Whole-Sky Imager. This was the beginning of the July IOP, and nearly a week passed before dependable SIROS observations were taken again. A few days after I left the site, heavy rains made the dirt roads approaching the site all but impassible, and part of the July 1995 IOP had to be scratched. These were the dramatic events, but I also observed more mundane concerns as well. For example, I realized that people could not be observing every instrument at all times. Examining datasets at a later date (such as from the solar-tracking pyrheliometer), it was obvious that it was extremely possible that the solar-tracker could "stick" for an instant, or longer. The tracker might resume working the next instant, or it might not, and only an experienced technician might ever notice the problem. A little bit of dust, or a bird dropping on an instrument might go unchecked for 24 hours until a knowledgable person could fix the problem. Because of my visit to the ARM site, I could examine data more critically.

3.4 Data Processing

Datasets from the ARM-SGP are processed and packaged into a Unidata-developed format called NetCDF (Network Common Data Format). An introduction to NetCDF is given in an Appendix of this report. Data stream and quality are managed at the site by the Site Scientists with data processing with packaging managed by the Data and Science Integration Team (DSIT). Currently (as of the Science Plan writing) the ARM data are collected at the rate of 400 megabytes per day, with additional data collected during the IOPs.

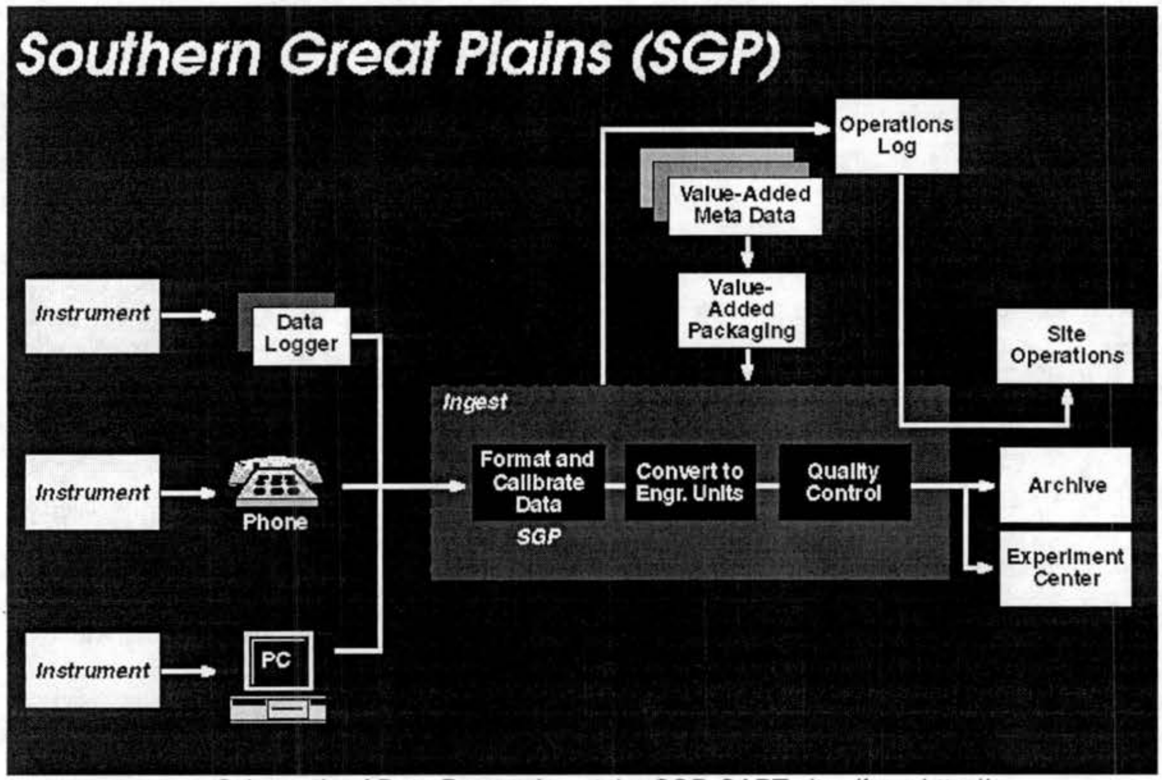

FIGURE 3.4: Schematic of Data Processing at the SGP-CART site. (from http://www.arm.gov/docs/data.html)

A DSIT goal is to ensure the ARM data to be of "known and reasonable quality" (ARM, 1996). ARM performs three levels of data management. Raw data from the instrument is first checked for self-consistency within the data stream. Next, the data goes through processing, including smoothing, interpolation, extrapolation, and time averaging. Finally, the data are reprocessed, by comparing with inputs from other data streams, and inputs from models (best-fit models for radiometers, etc.). All three processing levels take place as long as there are feeds of data, and the final "value-added product" is sent over telephone wires to the ARM Experiment Center at Pacific Northwest Laboratories.

At the Experiment Center, the data are processed again and packaged into the NetCDF format. From here, the datasets can be accessed by members of the Science Team in near real time. Finally, after three months at the Experiment Center, the data are archived at the ARM Data Archive at Oak Ridge National Laboratory.

All data are archived in the NetCDF format, and compressed, so that all file-names are expressed in the same format. An example is

"sgp5mwravgC1.c1.941024-941114.tar.Z,"

where "sgp" stands for Southern Great Plains, "mwravg" is for the MWR averages, "C1" stands for the Central Facility, "941024-92114" are the dates of the IOP, and "tar.Z" stands for the type of compression.When uncompressed, the files will have a form similar to

"sgp5mwravgC1.c1.941026.000500.cdf,"

where "941026" is the date, "000500" is the time in hours-minutes-seconds, and ".cdf" is the NetCDF filename extension. For other datasets, any piece of the filename code may be changed. A more complete list of the dataset filenames may be found in the Site Scientific Mission Plan (Splitt, Lamb and Sisterson, 1995).

CHAPTER 4

The SGP-CART Central Facility Instruments and Datasets

Some of the instruments at the ARM-CART site are proven field instruments, and others have been developed specifically for use in ARM, by the Instrument Development Plan (IDP).

Table 4.1 lists the relevant atmospheric properties and the instruments used to mea-

TABLE 4.1: Instrumentation used by ARM to address parameters used in this report.

Property	ARM Instrument Type
Solar Beam Flux	Sun-tracking Pyrheliometer (SIROS and BSRN)
Solar Flux, Downwelling and Upwelling	Pyranometers: Shaded and unshaded, uplooking and downlooking from 10 and 25 meters (SIROS and BSRN)
IR Flux, Upwelling and Downwelling	Pyrgeometer, shaded uplooking and downlooking at 10 meters. (SIROS)
Surface Albedo	
Temperature and Humidity Profiles	balloon-borne temperature and humidity sensors (BBSS) Surface Meteorological Observations (SMOS)
Water Vapor Mixing Ratio Profiles and Column Integrated Liquid and Water Vapor	• balloon-borne Water Vapor sensor (BBSS) • Two-channel Microwave Radiometers (MWR)
Ozone Profiles	Climatology
Optical Depth/Clear Sky	Satellite borne (Minnis')

TABLE 4.1: Instrumentation used by ARM to address parameters used in this report.

Property	ARM Instrument Type
Cloud Geometry (Fraction, Base, Top)	• Micropulse Lidar (MPL) • Belfort Laser Ceilometer (BLC) • Satellite-borne (Minnis) • Manual Surface Observations • Balloon-borne soundings (for estimating high relative humidity regions
Cloud Optical Depth and Emissivity	Satellite-borne (Minnis)
Cloud Optical Properties: albedo, etc.	Satellite-borne (Minnis),
Ice/Liquid Discrimination	
Precipitation Rate	Surface Meteorological Observation (SMOS)

sure them. For example, three-dimensional cloud geometry (cloud-base, cloud-top, cloud fraction) profiles can be derived from a combination of data from the Micropulse Lidar, Minnis' Cloud Products, visual surface observations and the Balloon-borne water vapor sensor.

While ARM data were collected at the boundary, extended and auxiliary facilities, only data collected at the Central Facility have been used here. Inherent with each dataset are missing data, bad data, and questionable data. Thus interpolation and averaging was needed to fill in good data. For some datasets, statistics were calculated (see Table 4.2 for the mathematical equations), which produced hourly, daily or whole IOP means and with corresponding standard deviations and skewness.

TABLE 4.2: Mathematical Formulations of some Statistics.

Statistics	Mathematical Formulation
Mean = $\overline{X}$	$\frac{1}{n}\sum_{i=1}^{n} X_i$
Standard Deviation = σ_x	$\left(\frac{1}{n-1}\sum_{i}^{n}(X_i-\overline{X})^2\right)^{1/2}$

TABLE 4.2: Mathematical Formulations of some Statistics.

Statistics	Mathematical Formulation
Coefficient of Variation = CV	$\sigma_X/\bar{X}$
Skewness = sk_x	$\left(\frac{1}{n-2}\sum_{i}^{n}(X_i-\bar{X})^3\right)^{1/3}$
Normalized Skew	sk_X/σ_X
Covariance = Sxy	$(\frac{1}{n})\sum_{i=1}^{n}(X_i-\bar{X})(Y_i-\bar{Y})$
Correlation = Rxy	$\frac{S_{XY}}{\sigma_X\sigma_Y}$

One of the most annoying tasks was to compare datasets that had different temporal structures. For example, the MPL recorded at 30 second intervals, the SIROS at 1 minute intervals, the MWR at 5 minute intervals, Pat Minnis' Satellite algorithm at hour intervals and soundings were taken every three hours. For example, to obtain hourly data, the BLC, SIROS and MWR data were averaged, while the soundings were interpolated. Five to ten percent of all IOP data was missing, bad, or questionable. So, depending on the severity of the problems, the data were either scratched or modified.

Note that all time of day values in these datasets are in units of Universal Coordinated Time (UTC), or Greenwich Mean Time (GMT). To convert into local time (Central Standard Time), subtract 6 hours. Sunrise during the October/November occurs around 12 UTC (6 CST), and sunset is around 23:30 UTC (17:30 CST).

4.1 The Micropulse Lidar (MPL)

NASA Goddard designed the MPL to measure the cloud-base height on a continual basis, provide optical depths for thin clouds, and make relative aerosol concentration esti-

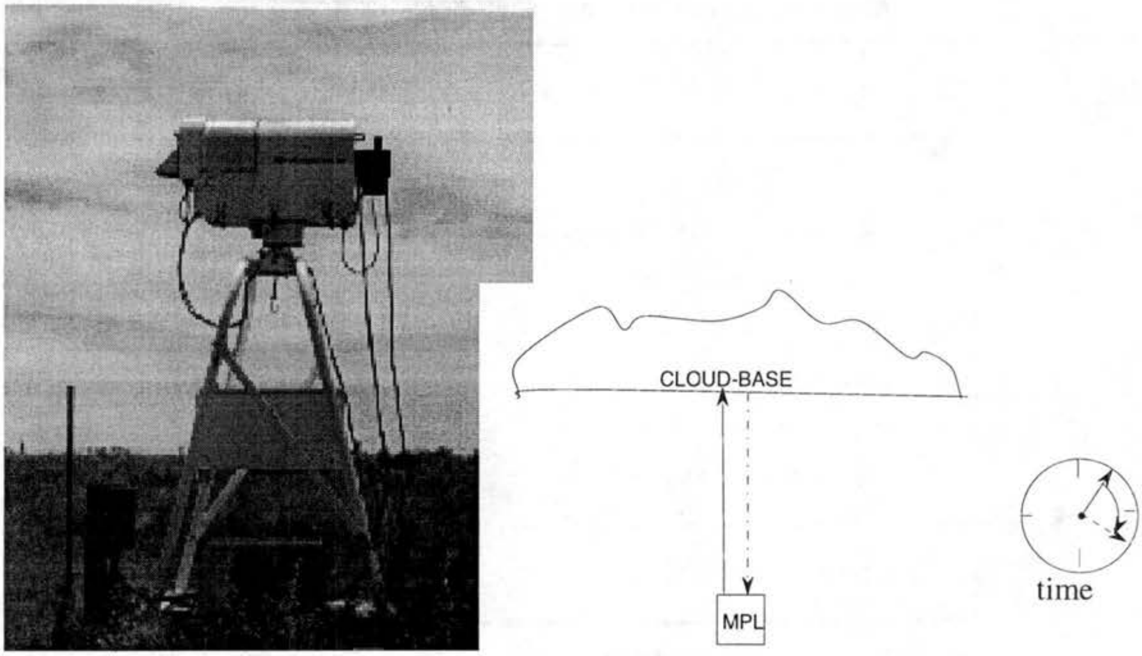

FIGURE 4.1: The Micropulse Lidar and schematic of its operation.

mates. The lidar (the acronym stands for **li**ght **d**etection **a**nd **r**anging) produces a pulse of light lasting 5 nanoseconds and about 1.5 meters long. As the pulse of light travels up to space, some of it is scattered back towards the instrument by the atmosphere, aerosols and clouds. The length of time required for the backscatter to reach the MPL is directly related to the distance of the scattering substance from the MPL, and the strength of the signal is related to the density of the scattering substance. Starting about 2 nanoseconds after the transmitted pulse, the MPL detector groups beam backscatter into 2 nanosecond time bins, which correspond to about 300 meter bins. Signal profiles are obtained by accumulating signals from 2500 pulses per second. With an accumulation time of 30 seconds, the signal to noise ratio is high enough to detect clouds up to 15 km above the surface.

4.1.1 The Data

The MPL NetCDF data files included only cloud-base measurements at 30 second intervals. A valid cloud-base could range between 270 and 15070 meters, with a 300 meter resolution. Values of -30 were inserted when no cloud was detected, and "60" was recorded when fog or condensation appeared on the sensor. Missing or bad data were assigned a value of "-999." A segment of the processed MPL data set from November 9, is shown in Table 4.3. Time is measured in hours (UTC) and cloud-base is measured in meters.

TABLE 4.3: MPL cloud-base data for November 9.

Time (UTC)	cloud-base (meters)	Time (UTC)	cloud-base (meters)
18.80	570	18.96	870
18.82	570	18.97	570
18.84	570	18.99	570
18.85	570	19.01	570
18.87	570	19.02	870
18.89	870	19.04	570
18.90	570	19.06	570
18.92	870	19.07	870
18.94	570	19.09	570

4.1.2 Statistics and Calculations

Because the MPL recorded cloud-base every 30 seconds, up to 120 observations were possible during a one-hour interval. Thus, hourly cloud amount (the percentage of time a cloud was overhead) could be easily calculated by dividing the number of "cloud" observations by the number of "total" observations. This hourly cloud amount is analogous to spatial cloud fraction (the percentage of the whole sky obscured by cloud at one instant). A "cloud" observation is considered to be any value not -30, 60, or -999. Also, note that the hour-interval had the corresponding hour value as its endpoint (i.e. 12:00 interval means observations between 11:01 and 12:00)

Was there a diurnal trend to cloud-base height or to cloud fraction? We can calculate means for particular hours on all days of the IOP. For example, at 19 UTC at any day of the IOP, one would expect a cloud fraction of.54 and a cloud-base of 2727 meters. Because the MPL registered -30 for clear sky and 60 for foggy conditions, it didn't make sense to include these numbers into the mean cloud-base statistics. Neither did it make a sense to average a 2000 meter and a 10,000 meter cloud-base, however this fact was ignored.

Even with the meaningless averages for mean cloud-base, there seems to be a strong diurnal variation to the cloud fraction (Figure 4.2) and the mean cloud-base height (Fig-

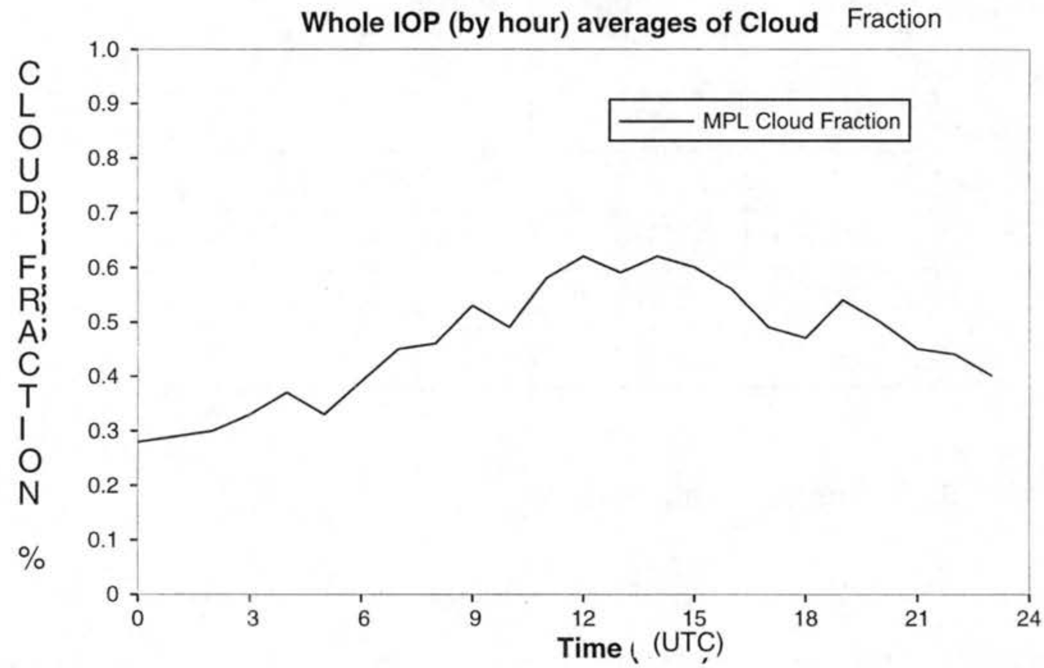

FIGURE 4.2: Whole IOP (by hour) averages of MPL Cloud Fraction.

ure 4.3). The MPL tends to show higher cloud-base, but lower cloud fraction during the nighttime hours.

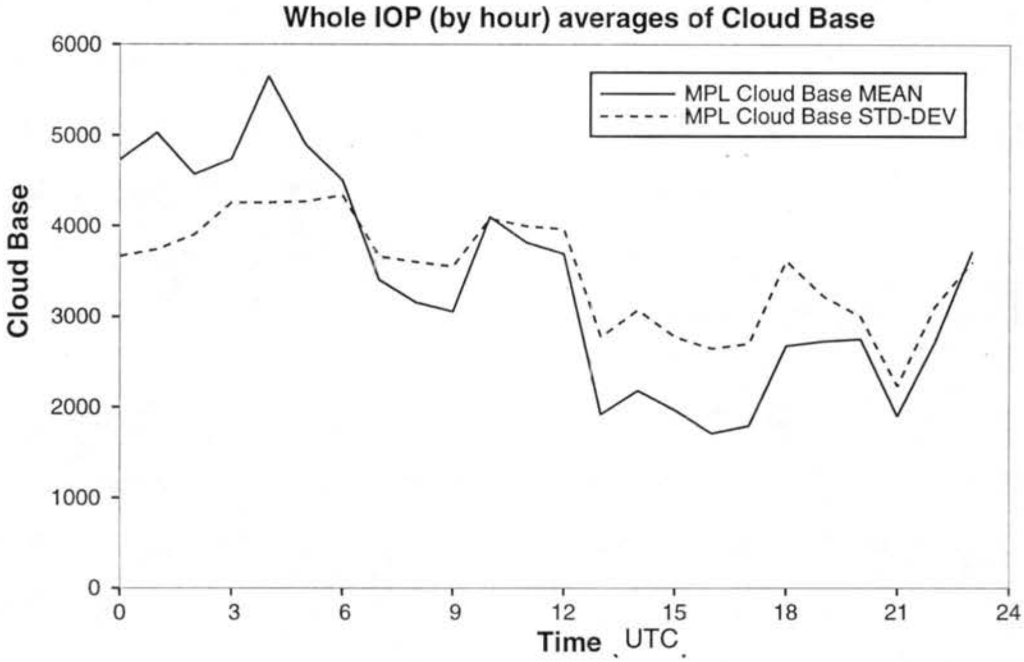

FIGURE 4.3: Whole IOP (by hour) Mean and Standard Deviation of MPL cloud-base.

4.2 Belfort Laser Ceilometer (BLC)

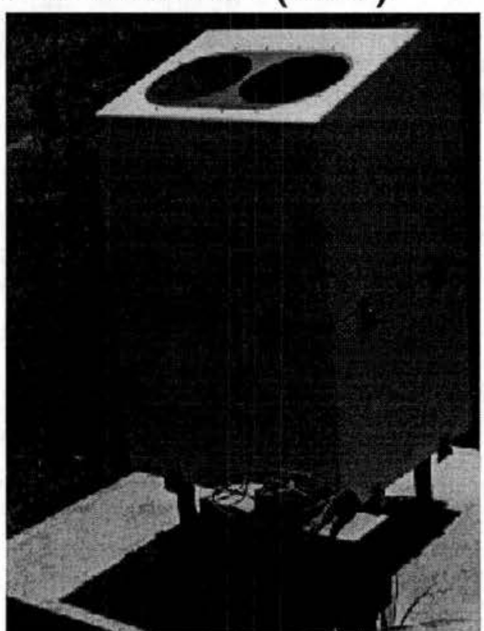

FIGURE 4.4: The Belfort Laser Ceilometer.

The Belfort Laser Ceilometer is, in principle, similar in operation to the Micropulse Lidar. A difference is that while the MPL transmits visible light (0.523 μm), the BLC uses near infrared light (0.910 μm). The ceilometer uses a fiber-optic cable to transfer the output of the laser to the focal point of a Newtonian telescope. The light energy is projected upward by the mirror in the transmitter telescope. The receiver telescope is aligned with the transmitter telescope for detecting light backscattered from any object in the transmitted beam (referenced from the ARM web page: http://info.arm.gov/cgi-bin/instrview.pl?inst=blc&from=view).

The BLC is able to identify more than one cloud-base (up to three) at each observation. Like the MPL, the BLC detects clouds through backscatter time intervals where the backscatter strength is dependent on the density of the substance. The BLC has a 30-second cycle in which it collects, analyzes and dumps out data. During the first 5 seconds it sends out about 5000 pulses and detects the backscatter. During the next 10 seconds the BLC number crunches, and for the last 15 seconds the instrument does nothing. Site operators have noticed that the BLC may fail to detect a thin cloud, cloud with the sun directly behind, or a cloud obscured by precipitation or fog.

4.2.1 The Data

Because the BLC has the capability to identify multi-layered clouds (if they are thin), the data set is a little more complicated than that of the MPL. Valid cloud-bases for the BLC ranged up to 7800 meters, with a resolution of 7.62 meters (and so would have a much larger temporal variability than the MPL). When no cloud was detected, the value was recorded as "0," and like the MPL, bad or missing data were recorded as "-999." Data, corresponding to the same time period as the MPL, is shown in Table 4.4.

TABLE 4.4: BLC cloud-base data (meters) for November 9.

Time (UTC)	cloud-base 1	cloud-base 2	cloud-base 3	Time (UTC)	cloud-base 1	cloud-base 2	cloud-base 3
18.81	770	0	0	18.97	747	0	0

TABLE 4.4: BLC cloud-base data (meters) for November 9.

Time (UTC)	cloud-base 1	cloud-base 2	cloud-base 3	Time (UTC)	cloud-base 1	cloud-base 2	cloud-base 3
18.82	747	0	0	18.98	747	0	0
18.83	800	0	0	18.98	739	0	0
18.83	792	0	0	18.99	739	0	0
18.85	770	0	0	19.00	785	0	0
18.86	785	0	0	19.01	739	0	0
18.87	808	0	0	19.02	747	0	0
18.87	800	0	0	19.02	777	0	0
18.88	747	0	0	19.03	785	0	0
18.89	732	0	0	19.04	762	0	0
18.90	754	0	0	19.05	747	0	0
18.91	747	0	0	19.06	770	0	0
18.92	747	0	0	19.07	762	0	0
18.92	739	0	0	19.08	792	0	0
18.93	800	0	0	19.08	777	0	0
18.94	739	0	0	19.09	754	0	0
18.95	739	0	0	19.10	754	0	0
18.96	747	0	0				

4.3 Microwave Radiometer (MWR)

4.3.1 The Data

The Microwave Radiometer is essentially a vertical pointing microwave receiver and measures vertical (column) water vapor path, liquid water path, and infrared equivalent temperature, averaging over five minute intervals. It is tuned to measure the microwave emissions of the vapor and liquid water molecules in the atmosphere at specific frequencies. (from web page: http://info.arm.gov/cgi-bin/instrview.pl?inst=mwr&from=view).

FIGURE 4.5: The Microwave Radiometer.

A segment of the data set for November 9 is given in Table 4.5. Note that the liquid water path has been multiplied by 100 (so that both the vapor and the liquid could be graphed on the same scale). Plots for the whole IOP can be found in Chapter 5.

TABLE 4.5: MWR vapor, liquid water path and IR-equivelent temperature for November 9.

Time (UTC)	Vapor (mm)	Liquid (mm*100)	IR-equivalent Temp (K)
18.83	10.01	2.30	271.72
18.92	10.03	1.44	270.11
19.00	10.06	2.60	273.49
19.08	10.07	3.99	274.81

For some dates (November 13 for instance), the liquid water seems to have an upper limit of 1 mm (100 units on this table). If the instrument tried to record a higher value, then -999 (error) would be reported for all parameters of the MWR.The reason was that the MWR was calibrated so that liquid water paths over 1 mm deep were considered impossible. Jim Lilijgren, of the Lawrence Livermore Lab, re-calibrated this dataset (for one hour averages instead of five minute averages) so that 1 mm was a legitimate value. According to Jim Lilijgren (referenced from the web page at http://info.arm.gov/cgi-bin/

MICROWAVE RADIOMETER AVERAGES FROM THE OCT/NOV 1994 IOP

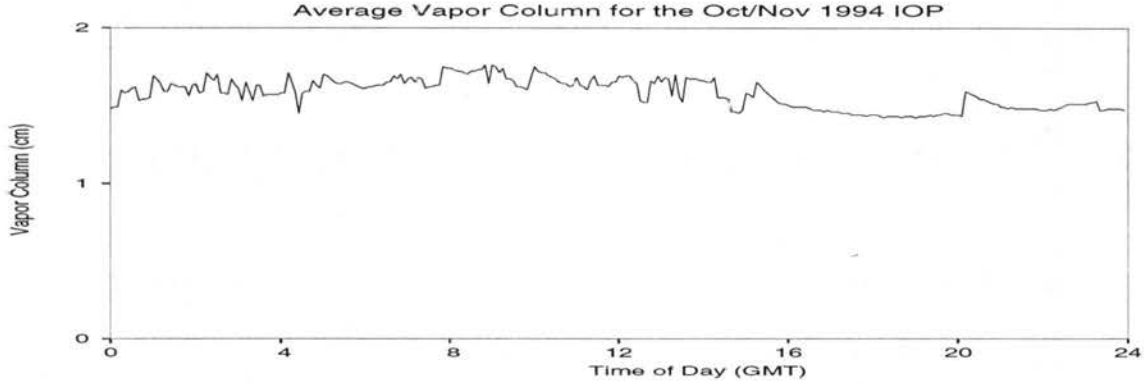

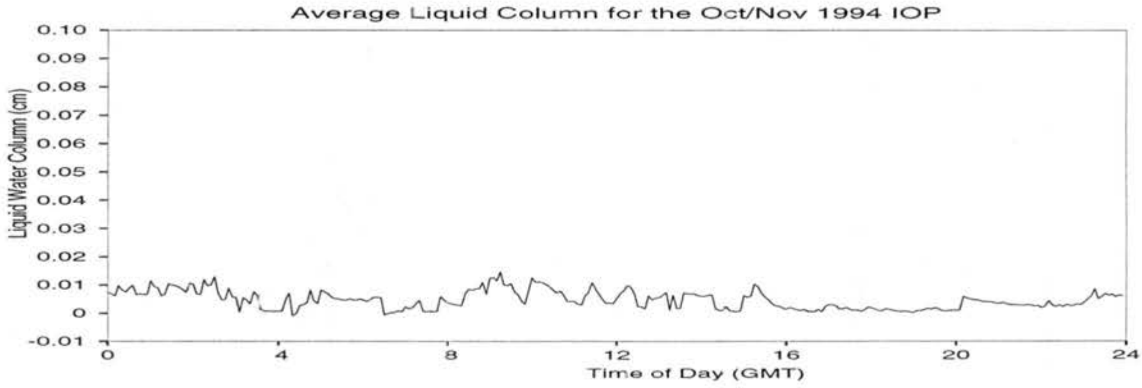

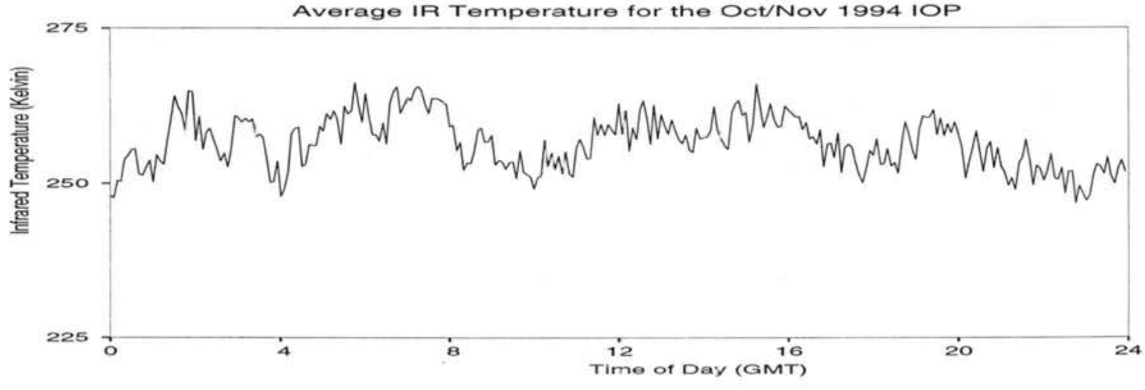

FIGURE 4.6: Whole IOP averages (all from the MWR) of Precipitable Water Path, Liquid Water Path, and IR Brightness Temperature.

instrview.pl?inst=mwr&from=view), the MWR has a "noise" threshold of ±0.03mm, so that a value of +0.03 mm could be considered a clear sky value.

Whole-IOP averages for the liquid, vapor and IR-temperature values are shown as Fig. 4.6. Unlike the cloud-base and fraction from the MPL, there does not seem to be a strong diurnal trend.

4.4 The Baseline Surface Radiation Network (BSRN)

The BSRN data instrument array includes four radiometers, located 3 meters from each other and a meter above the ground (Table 4.7):

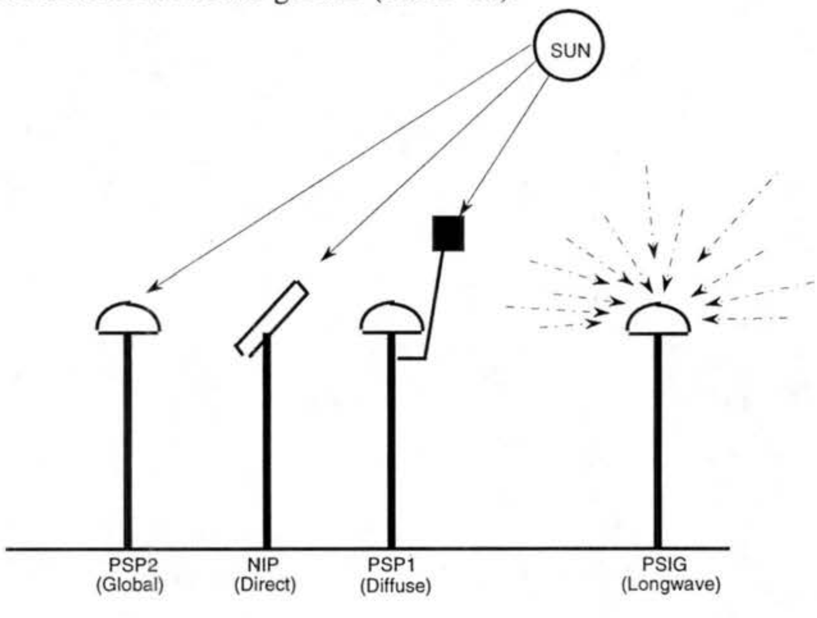

FIGURE 4.7: Components of the BSRN.

1) one Eppley Normal Incidence Pyrheliometer (nip) with a solar tracker to measure direct normal solar radiation

2) two Eppley Precision Spectral Pyranometers (psp1 and psp2); one for measuring hemispherical global (diffuse + direct) radiation, the other with a tracking shade disc to measure only hemispherical diffuse radiation.

3) one Eppley Precision Infrared Radiometer or Pyrgeometer(pir - also called a psig) with a solar "filter" to measure hemispherical broadband downwelling infrared radiation.

The solar pyranometers have detectors that are covered by a special glass which is transparent throughout most of the solar spectrum (0.285 μm to 2.8 μm). The detector consists of a black disk in thermal contact with the "hot" side of a thermopile, and in thermal contact with a "cold" side of the instrument case (which theoretically should have the temperature of the surrounding air). The difference in temperatures can be used to derive flux values (in Watts per square meter). The response of the detector varies with the cosine of the solar zenith angle. The solar pyrheliometer uses the same solar detector as the pyranometers, but its viewing angle is restricted to 5.7 degrees and aimed directly at the sun by an automatic solar tracker. The pyrgeometer uses a detector sensitive to radiation between 3.5 and 50 μm. Because this band has some overlap with the solar spectrum, the pyrgeometer uses a special sunlight-blocking disk plus a special solar interference filter, to keep the solar flux from warming the instrument and contaminating the terrestrial flux measurements.

4.4.1 The Data

Measurements of the downwelling Global Hemispheric, Diffuse Hemispheric, and Direct Normal Solar fluxes, and the Hemispheric Total Infrared flux were recorded every minute. Values of the Direct Normal Solar Fluxes were obtained by multiplying the values in the data set by the cosine of the zenith angle. Unlike cloud-base measurements, it was reasonable to calculate five-minute or even hourly averages of the flux values from the BSRN. Table 4.6 includes some BSRN values from November 9. SWINC is the ShortWave Incident at the top of the atmosphere, which is the solar constant multiplied by cos(Z), and Percent Solar is Global Solar divided by the SWINC. Because the Direct Solar is small, the Diffuse is large and the Percent Solar is small, it is obvious that clouds

TABLE 4.6: BSRN surface flux data for November 9.

Time (UTC)	cosZ	zenith angle (°)	Direct Solar (W m^{-2})	Diffuse Solar (W m^{-2})	Global Solar (W m^{-2})	SWINC (W m^{-2})	% Solar	Down LW (W m^{-2})
18.83	0.59	54.03	10.23	298.65	295.81	802.96	36.84	331.67
18.92	0.59	54.13	0.15	259.74	249.29	800.91	31.13	332.85
19.00	0.58	54.27	-0.62	228.20	218.19	798.36	27.33	334.53
19.08	0.58	54.42	-1.24	215.05	204.15	795.32	25.67	335.05

were present during this time period.

4.5 Solar and InfraRed Observation System (SIROS)

FIGURE 4.8: Some of the SIROS and BSRN instrumentation.

The SIROS system measures similar radiation quantities as the BSRN but with down-looking instruments as well as the uplooking ones of the BSRN. The instruments and their functions are:

1) pyrheliometer to measure normal incidence solar direct beam;

2) pyranometer to measure downwelling hemispherical global solar;

3) pyranometer to measure downwelling hemispherical diffuse solar;

4) pyranometer to measure upwelling hemispherical global solar (10 m above ground);

5) pyrgeometer to measure downwelling broadband hemispherical IR;

6) pyrgeometer to measure upwelling broadband hemispherical IR (10 m above ground).

The SIROS system also includes a Multi-filter Shadowband Radiometer (MFRSR), a thermopile detector located 25 meters above the surface, which basically acts like all three solar BSRN instruments in one. That is, the MFRSR can alternately cover the sun (measuring diffuse), shadow all but the sun (measuring direct), or shadow nothing (measuring the total).

4.5.1 The Data

The SIROS datasets contained much of the same information as the BSRN (the downward components of the Total Hemispheric, Diffuse Hemispheric, and Direct Normal Solar fluxes, and the Hemispheric Total Infrared flux. They also included narrowband (spectral) breakdowns of the infrared fluxes, and directional (upwelling/downwelling) breakdowns of both the IR and the Solar fluxes (Table 4.7). It should be noted that the SIROS dataset is considered as being in "beta" mode, meaning that it has not yet been completely quality controlled.

There are two things to note in this table. One is the obvious ridiculousness of the MFRSR data (Total, Direct and Diffuse Solar fluxes). It turned out the calibration of the MFRSR data was never completed and the data are still in "counts." Also notable are comparisons with the pyranometer, and pyrheliometer data recorded by the BSRN. A

TABLE 4.7: SIROS flux data for November 9: pyrh = pyrheliometer, pyr = surface pyranometer, 10m = 10meter pyranometer, MFRSR = multifilter shadow band radiometer.

Time (UTC)	Total Solar MFRSR (Wm^{-2})	Dir Solar MFRSR (Wm^{-2})	Diff Solar MFRSR (Wm^{-2})	Dir Solar pyrh (Wm^{-2})	Up LW 10m (Wm^{-2})	Down LW pyr (Wm^{-2})	Up SW 10m (Wm^{-2})	Down SW pyr (Wm^{-2})	IR-Surf Temp (K)
18.83	848.1	48.74	820.3	14.75	368.8	337.6	56.56	288.8	284.0
18.92	726.9	5.96	724.5	.95	367.6	337.9	48.93	248.5	283.7
19.00	642.8	.55	643.2	.43	367.7	339.8	43.31	218.6	283.7
19.08	610.9	1.17	610.5	.00	365.6	341.1	40.85	205.5	283.3

more detailed comparison between the SIROS and the BSRN is found in Chapter 5.

4.6 Balloon Borne Sounding System (BBSS)

FIGURE 4.9: The author launching a BBSS at the Central Facility.

Balloon-Borne Sounding Systems (BBSS) were launched every three hours from the Central Facility, to measure the pressure, temperature, dewpoint, relative humidity and winds within an atmospheric column. Most of these balloons succeeded in reaching tropopause, but a few burst or malfunctioned at much lower levels. The sensors report temperature, humidity, and pressure data at 2 second intervals. Table 4.8 is an example of the data from the 18 UTC, November 9 sounding, where heights were calculated with the hypsometric equation,

$$\Delta Z = \frac{R_d \bar{T}}{g_0} ln\left(\frac{p_{lower}}{p_{upper}}\right),$$

where $R_d = 287$ J K^{-1} kg^{-1} is the dry air gas constant, $g_0 = 9.8$ m s^{-1} is the gravitational acceleration, T is the average temperature in the layer, and p_{lower} and p_{upper} are the pressure layer boundaries. Further manipulation of the soundings involved interpolation to

TABLE 4.8: Segment of the 18Z November 9 sounding

Height (m)	Pres (mb)	Temp (°C)	Dewpt (°C)	RH (%)
1237.	858.2	1.1	-0.7	88.0
1249.	857.0	1.1	-0.8	87.0
1259.	855.9	1.1	-0.8	87.0
1268.	854.9	1.1	-0.8	87.0
1278.	853.9	1.0	-0.9	87.0
1290.	852.6	0.9	-1.2	86.0
1299.	851.6	0.9	-1.2	86.0

uniform grids as well as interpolation to fill missing data.

Although clouds are regions of saturated (100% Relative Humidity) air, the balloon might go through a clear spot in a cloud layer, or the humidity sensor might give inaccurate readings at low pressures and low temperatures. Therefore, regions of "high" relative humidity in the vertical path of the balloon could be interpreted as cloudy layers. As "high" relative humidity is relative, cloud threshold RH values lowered with height.

So that relative humidity could be easily plotted and compared with cloud-base and cloud-top measurements (i.e. humidity as a 2-Dimensional plot - time and level: "Composite Plots" in chapter 5), the balloon soundings were interpolated to a uniform vertical grid (height) and to a uniform horizontal time (one hour). An appendix shows the steps used to interpolate these soundings. Similar interpolations were performed to put sounding profiles to a 25 mb grid to run the radiation parameterization.

4.7 Satellite Derived Cloud Measurements - Minnis

4.7.1 Description of Methodology

For these cloud measurements, the Central Facility was centered in a 0.3° by 0.3° box drawn on the earth's surface. Then this box was further broken into 4 km by 4 km "pixels." The Visible Infrared Spin Scan Radiometer (VISSR), on board the GOES-7 (Geostationary Operational Environmental Satellite) was calibrated with the sun-synchronous NOAA-11's Advanced Very High Resolution Radiometer (AVHRR) to continuously look down upon the box and the Central Facility. Minnis (1995) assumed that clouds are plane-parallel entities (no curvature of clouds even though the earth is round) and have horizontally constant particle sizes and particle optical properties. Also, he assumed that if a cloud was detected within a pixel, then the pixel was completely represented by the cloud. Each cloudy pixel was assumed to have a cloud at only one altitude and its physical thickness was calculated via empirical formulae using its optical properties. Minnis then characterized the cloudiness over the Central Facility, using a superposition of all the pixels in the 0.3° gridbox.

The methodology to retrieve cloud properties is called the "layer bispectral threshold method." Cloud-fraction, cloud-center temperature and altitude, cloud-top temperature and altitude, and cloud optical depth were computed for three height intervals ($z \leq 2$ km, $2 \leq z \leq 6$ km, and $z > 6$ km - designated as levels "low", "middle" and "high" respectively). The total (designated as level "total") cloud amount is the simple sum of all three layers with no overlap, and the total cloud-center and cloud-top temperature and altitudes are weighted averages of the other levels with the cloud-fractions serving as the weights. IR Brightness temperature estimates for each cloud layer are performed at the 11.5 μm wavelength. The cloud-center temperature is defined as the equivalent radiating temperature of the cloud and the cloud-center altitude is the altitude corresponding to this temperature (as determined from a sounding). This means, for optically thin clouds, that the cloud-center temperature is somewhere within the cloud, but for optically thick clouds, the cloud-center temperature (and altitude) are the same as for the cloud-top (because the satellite can't "see" below the cloud-top).

For the satellite to "know" if a cloud is present, observations are compared with known "clear-sky" measurements of temperature and reflectance. Empirical formulae, based on climatology of clear sky measurements, are used to calculate the clear sky values, and then the cloud-detecting algorithm uses statistical methods to decide whether the actual satellite measurements are different enough from clear-sky values to indicate a cloud is present. The algorithm uses the assumption that a cloud is almost always more reflective and colder than the surface. For example, the cloud algorithm indicates a cloud is present if the difference between brightness temperature of the observations and the clear sky values are more than 5° or the reflectance is greater than some clear-sky value (Minnis et al, 1987). Clear sky temperature-reflectance relationships can be constructed at 2 km, 6 km and tropopause height, so that the presence of a cloud at these levels can be inferred from the measured temperature and reflectance.

Once the satellite "detects" a cloud, the cloud's albedo and transmission can then be computed by parameterizing both scattering and absorption - by the cloud, the surface and the free atmosphere. These calculations involve knowing if the cloud is water or ice. If the cloud radiating temperature is greater than 253 K it is assumed to be a water cloud with an effective cloud-particle radius of 10 μm. Ice clouds (colder than 253 K) are assumed to consist of hexagonal ice crystals with a range of sizes. If the cloud radiating temperature (cloud-center temperature) is a function of cloud emissivity, cloud-top and clear sky temperatures, then the optical depth can be computed by an iterative, best fit process. If cloud-top altitude is matched with a sounding to the cloud-top temperature then the physical thickness of the cloud can be found using the already computed optical depth of the cloud. For more details, see Minnis, et al. (1987).

4.7.2 The Data

The satellite-derived cloud measurements data-set includes many more variables than were useful for this work, and includes data from latitudes and longitudes other than those of the Central Facility. Table 4.9 lists the "units" and "dimensions" for variables which important for this project. The first five variables have only one dimension each, the values of the dimensions are listed. The number of hourly observations in a day (≤ 24) is characterized by the dimension "time." The satellite looked at nine regions (3 latitudes X 3 longitudes) over the CART site, with the Central Facility at the center (36.6° N and -97.5°W). The dimension "level" corresponds to the height of the cloud-top, grouped into low, middle, high, and total: (level 1 corresponds to low clouds below 2 km, level 2 corresponds to middle clouds between 2 km and 6 km, level 3 corresponds to high clouds above 6 km and level 4 corresponds to a satellite derived "union" of all the clouds visible). The dimension "view" can also have two values: 1 for the clear scene (the value with no clouds) and 2 for the total scene (the value with clouds included).

TABLE 4.9: Minnis' Variables and Dimensions important to this report. Notes: 1) listed for the first five entries are the values of the dimensions, 2) The Central Facility is at latitude=36.6, longitude=-97.5.

Variables	Units	Dimensions
Time_Offset	seconds	time (= unlimited <= 24)
Latitude,	degrees	latitude (= 3: 36.9, 36.6, 36.3)
Longitude	degrees	longitude (= 3: -97.8, -97.5, -97.2)
Level	unitless	level (= 4: Low, Middle, High, All)
View	unitless	view (= 2: ClearScene, Total-Scene)
Cloud_Amount	percent	time, level, latitude, longitude
Visible_Optical_Depth, IR_Optical_Depth, Emissivity, Albedo	unitless	time, level, latitude, longitude
Cloud_Center_Height, Cloud_Top_Height, Cloud_Thickness	kilometers	time, level, latitude, longitude
Cloud_Center_Temp, Cloud_Top_Temp	Kelvin	time, level, latitude, longitude
Broadband_LW_Flux	Wm-2	time, view, latitude, longitude
Broadband_SW_Albedo, Narrowband_VIS_Albedo	unitless	time, view, latitude, longitude
Clear_Temperature	Kelvin	time, latitude, longitude
Solar_Zenith_Angle	degrees	time, latitude, longitude

An example of a piece of the data set for November 9 is in Table 4.10, where cloud_base = cloud_top - thickness.

TABLE 4.10: Satellite Cloud Retrievals for November 9.

Time UTC	level	cloud_ amount (%)	vis_ opt depth	IR_ opt depth	cloud_ top (meters)	cloud_ center (meters)	albedo	thick ness (meter)	cloud-base (meter)
18.5	1	0.00	0.00	0.00	0	0	0.00	0	0
18.5	2	100.00	0.00	0.00	3370	3370	0.00	0	3370

TABLE 4.10: Satellite Cloud Retrievals for November 9.

Time UTC	level	cloud_ amount (%)	vis_ opt depth	IR_ opt depth	cloud_ top (meters)	cloud_ center (meters)	albedo	thick ness (meter)	cloud- base (meter)
18.5	3	0.00	0.00	0.00	0	0	0.00	0	0
18.5	4	100.00	0.00	0.00	3370	3370	0.00	0	3370
19.5	1	0.00	0.00	0.00	0	0	0.00	0.	0
19.5	2	100.00	11.08	5.54	3360	3360	0.55	470	2890
19.5	3	0.00	0.00	0.00	0	0	0.00	0	0
19.5	4	100.00	11.08	5.54	3360	3360	0.55	470	2890

Like the other data sets, statistics can be made on some of these variables. For example, cloud_amount can be averaged, just like as with the MPL.

4.8 Surface Meteorological Observing System (SMOS)

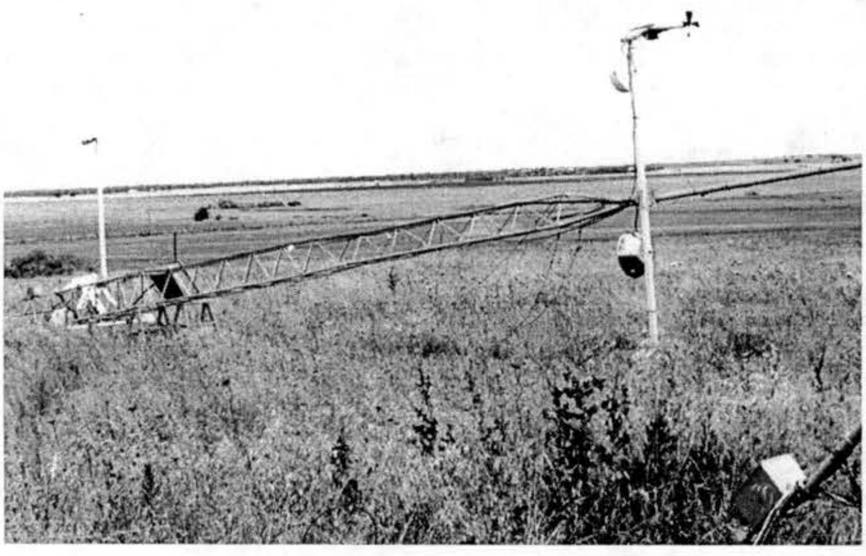

FIGURE 4.10: The SMOS tower lying on the ground waiting to be fixed (after a lightning storm).

The SMOS is a collection of standard meteorological instruments to measure surface conditions including wind speed and direction, temperature, relative humidity, vapor pressure, barometric pressure, snowfall, and rainfall. For each parameter, the SMOS measures a mean and a standard deviation for half hour intervals.

TABLE 4.11: Some Surface Data for November 9. 18 UTC is the observation for 17:30 UTC for consistency with other data.

Time (UTC)	Temp (°C)	RelHum (%)	Vapor Pressure (mb)	Barometric Pressure (mb)	Rainfall past half hour(mm)
18	6.69	81.70	8.01	982.93	.00
19	7.35	81.50	8.36	983.19	.00
20	7.77	79.80	8.43	982.78	.00

CHAPTER 5

Data Comparison

In some cases, two different datasets offer the same type of information. One example is the BLC and MPL both recording cloud-base. Another is the BSRN and SIROS both recording solar fluxes. We can also theoretically calculate an atmospheric parameter with one or more datasets and compare with a measured value from another dataset (Bretherton et al., 1994 and Levy et al., 1993).

5.1 Cloud-base Measurements from the BLC and MPL

While the MPL and the BLC measured the same quantity, their operation and resulting data streams were quite different. These differences included the valid cloud-base range, the resolution of the cloud-base, the sampling and averaging time intervals, and abilities for multiple cloud layer detection.

For the MPL, a valid cloud-base could range between 270 and 15070 meters with a 100 meter resolution. Valid cloud-bases for the BLC ranged up to 7800 meters, with a resolution of 7.62 meters. A MPL clear sky was recorded as -30, while the BLC would record 0. The MPL also had a flag for fog/condensation, recorded as 60. Invalid or missing values from both instruments were recorded as -999. The MPL sampled and averaged cloud-base data over a 1 minute interval, while the BLC sampled and averaged over a 30 second interval.

The capabilities of the two instruments differed as well. The BLC had some capabilities of identifying multi-layered cloud-bases (hence cloudbase1, cloudbase2, cloudbase3), but only when the lower clouds were relatively thin. The MPL had the ability to detect a higher cloud-base (up to 12 km) and hence could detect cirrus clouds.

Because the instruments measured essentially the same quantity, only one of the datasets was needed for future work. The MPL had a larger range, but coarser resolution than the BLC. The BLC had the extra capability of detecting multiple cloud-bases. For a "fair" comparison, we can compare the lowest cloud-bases detected by each instrument during all five-minute time intervals of the IOP. Statistics are in Table 5.1 with the data graphed in Figure 5.1. .

TABLE 5.1: Statistics for the BLC and MPL when both instruments measured a lowest cloud-base in a five-minute interval.

Instrument	Number of Observations.	Mean cloud-base	Standard Deviation	Skewness
BLC	1823	1029	1063	1385
MPL	1823	1113	1061	1347

The instruments essentially recorded the same cloud-base when there were clouds present (correlation was 0.95395, and means about 100 meters apart.). However, the MPL recorded simpler data (just time and cloud-base) and could detect cirrus clouds. Also, while the BLC could detect multiple cloud-base levels, there were too few instances recorded to be of any use. Thus the MPL cloud-base was used for the rest of this work.

5.2 Solar Fluxes from the SIROS and the BSRN

As discussed in the previous chapter, the SIROS (Solar and Infrared Observing System) is basically a newer and more detailed BSRN (Baseline Surface Radiation Net-

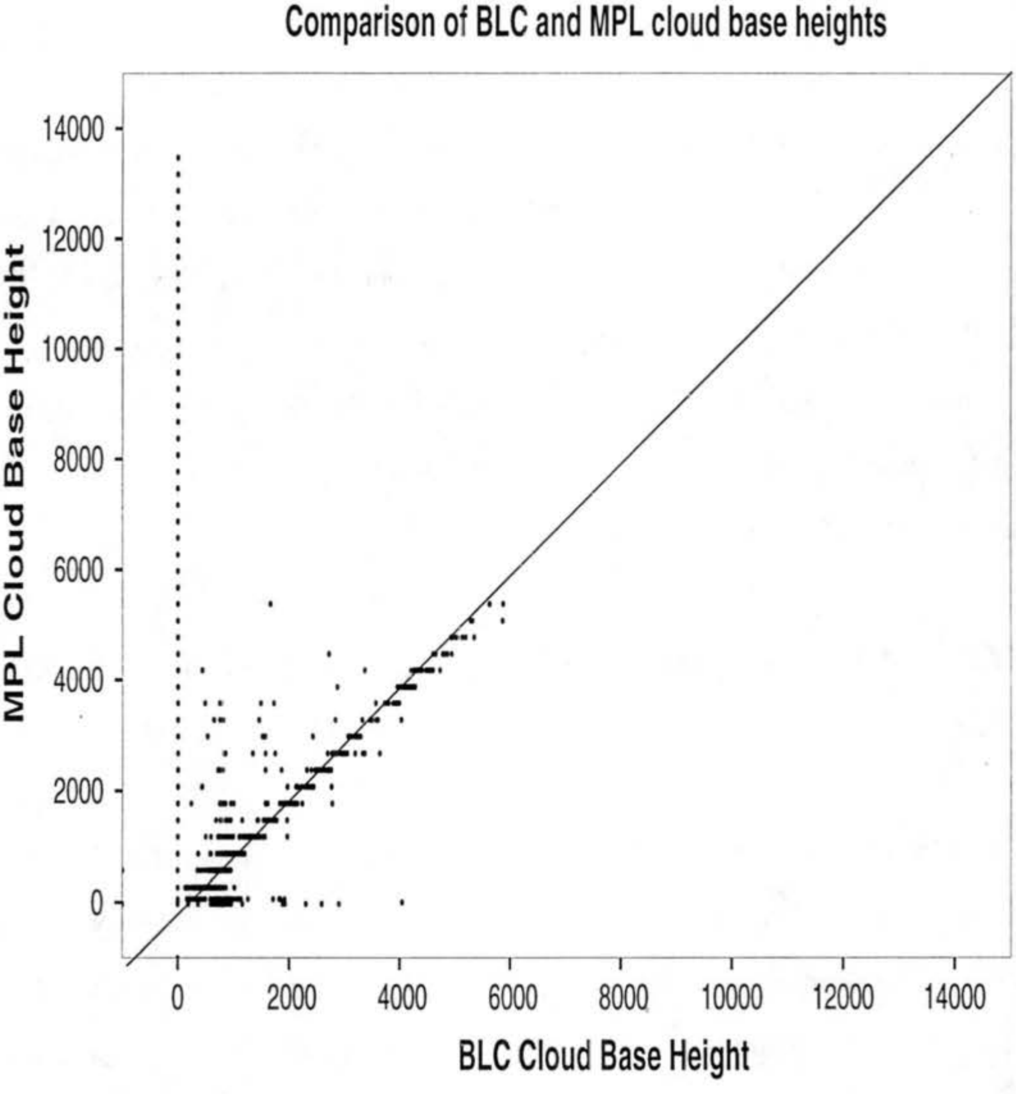

FIGURE 5.1: Comparison of the lowest BLC and MPL cloud-base heights, for all five minute intervals during the IOP.

work). Both systems measure solar and infrared fluxes with the use of radiometers, but the SIROS includes a MFRSR (MultiFilteR Shadowband Radiometer) to measure solar fluxes and includes radiometers to spectrally analyze and directionalize the solar and infrared components. Also, the BSRN gives results in one-minute intervals, while the SIROS measures at 15-second intervals. For these analyses, only the broadband fluxes were examined, so that the BSRN and SIROS produced similar observations. Specifically, the direct, diffuse, and total downward solar flux, and the downward IR values were computed for five-minute intervals and for one--hour long intervals.

The solar values from the SIROS pyranometers and the BSRN pyranometers agree closely, as do the downwelling longwave values. Because the systems are located a few meters apart at the ARM-SGP site, the numbers need not be identical. However, The solar values from the MFRSR (SIROS) are ridiculous. Even though the NetCDF files listed MFRSR data as Watts per square meter, these values are are much too high, meaning the calibration was not done correctly. Because some of the SIROS dataset is certainly in error, and the rest of the dataset is also questionable (beta mode), it really does not make good sense to use SIROS data.

5.3 Cloud-bases from the MPL and Cloud Tops from Minnis

Do the cloud-bases detected by the MPL lie below the cloud-tops retrieved by the satellite? As seen by the pictures in the chapter of Composite Plots, most cloud-base/cloud-top estimates make sense, except when very low clouds (< 1 km) or very high clouds (>8 km) are involved. The satellite may not see high thin clouds and, often may not distinguish low clouds from the ground. Thus, the retrievals would mistake a low cloud for a thin high cloud.

5.4 Cloud Fractions derived from the MPL and Minnis

In the last chapter, the percentage of time during hour intervals that the MPL detected a cloud was called "hourly cloud amount." Minnis' calculated the average percentage of sky obscured by clouds each hour, which would be "sky cover fraction." Even though they are different quantities, we can compare them as "cloud-fraction."

Figure 5.2 is a direct comparison between MPL and Minnis cloud fraction for each

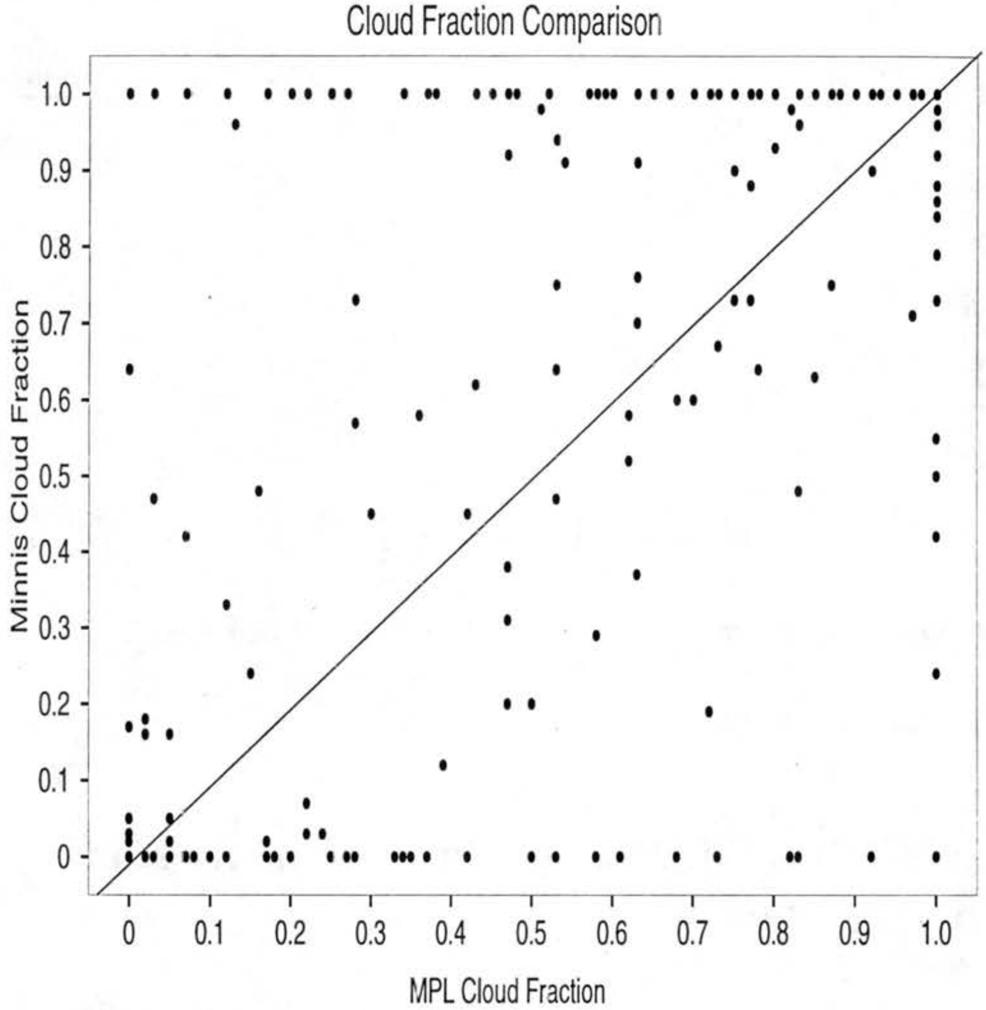

FIGURE 5.2: A Comparison of the MPL and Minnis' Cloud Fraction (%) for each hour of the IOP.

individual hour during the IOP. The fit does not look good, although the large number of (0.0,0.0) and (1.0,1.0) points make the correlation fairly high at 0.8. Some of the large number of points along the bottom axis represent periods when the clouds were not detectable by the satellite, but would have been seen by a ground-based lidar. When the whole IOP averages, by hour of the day, of the cloud fractions are computed (Figure 5.3), amazingly, they agree quite well, especially during the late night between 6 UTC and 12 UTC (midnight and 6 AM local time). At other times, Minnis' cloud fraction is

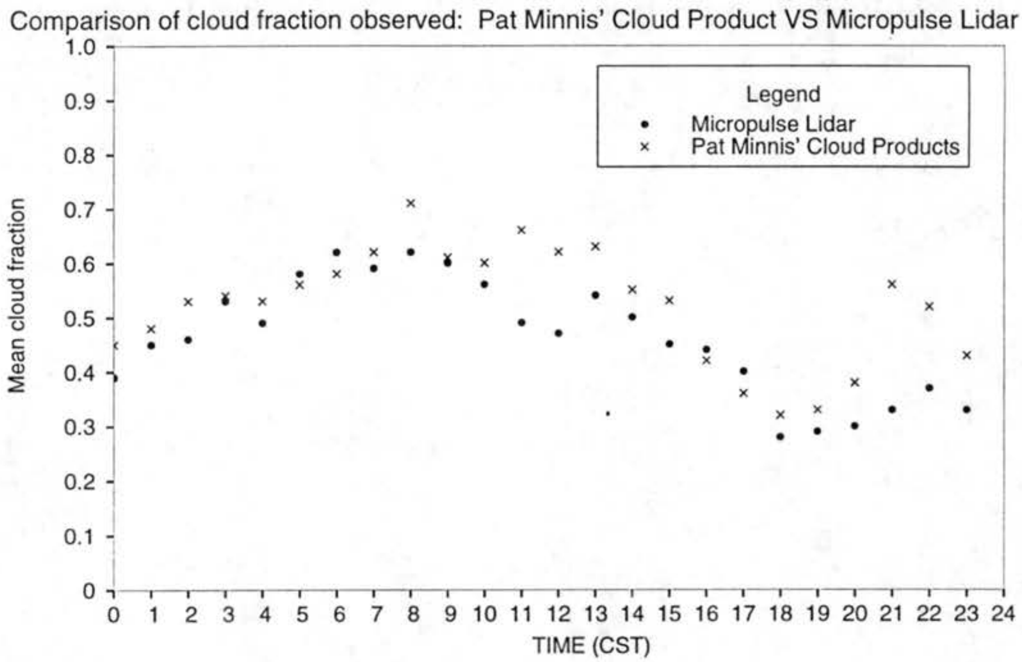

FIGURE 5.3: A Comparison of MPL and Minnis' Cloud Fraction (%) averaged by the hour of the day, during the IOP.

10-20% higher than the MPL.

5.5 SMOS vs. SIROS estimates of surface "skin" temperature

The surface "skin" temperature is the effective radiating temperature of the earth's surface, and it is needed as input for a longwave radiation model. The SIROS system measures the upwelling radiation from the earth's surface, and using the Stefan-Boltzmann constant, one can back out the radiating skin temperature. However, because the SIROS system has a large amount of missing data, we might assume it worthwhile to use only the surface temperature from the SMOS, and no information from the SIROS. Are the quantities similar enough? Looking at Figure 5.4, there is quite a substantial difference between the two quantities, especially between day and night. Physically, the surface "skin" is more heat conductive than the atmosphere near it. In the daytime, the surface temperature is lower (by up to 6 K) than the skin temperature, while the reverse

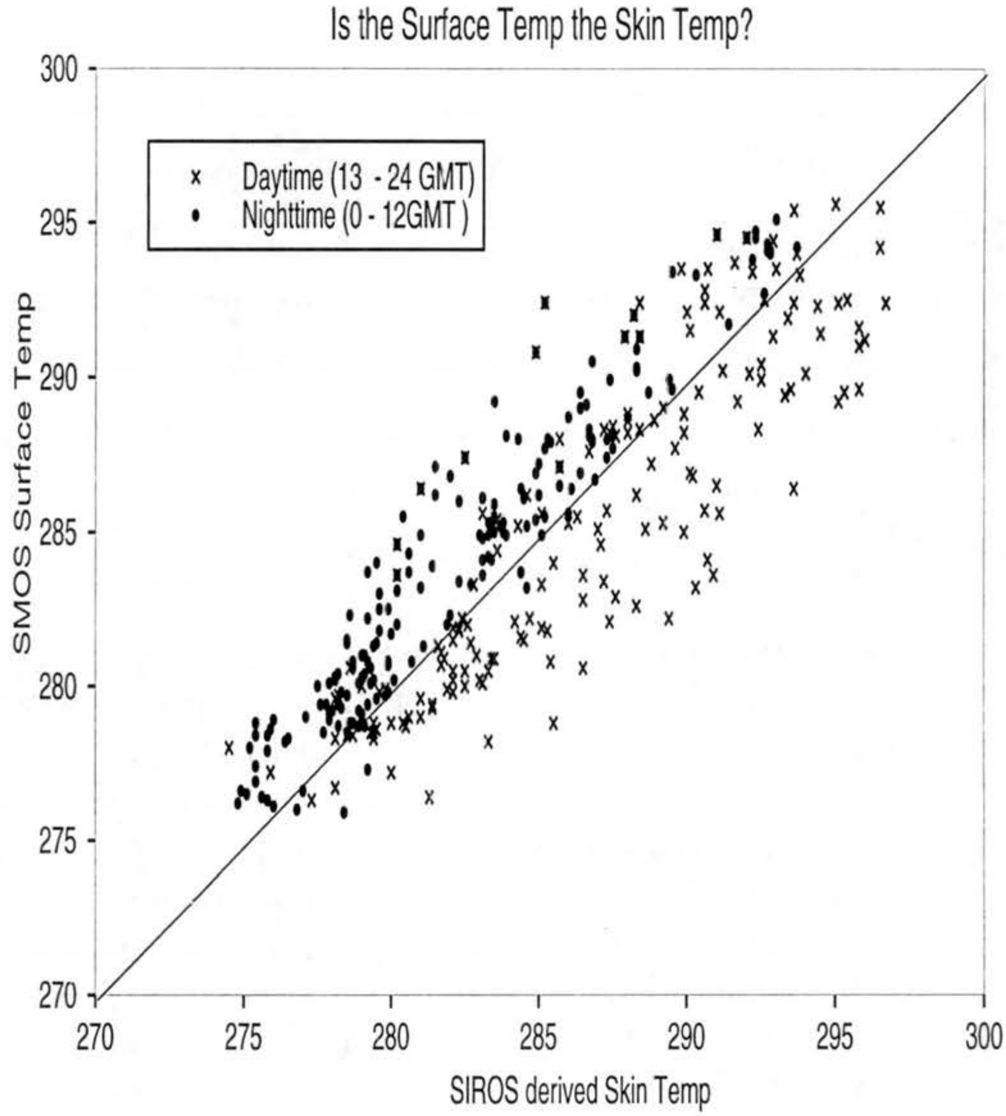

FIGURE 5.4: Comparison of SMOS surface temperature and SIROS skin temperature for day (x's) and night (dots)

is true during the night. This translates into about a 30 W m^{-2} difference in surface long-wave flux, which is a substantial 10%. Yet, with the balance between day and night, and the lack of useful SIROS data on other counts, it is still beneficial to ignore all SIROS data.

5.6 Composite Plots

This section presents a time series of all the relevant cloud and radiation data from the IOP (October 24 - November 14, 1994), including: MPL cloud-base, Minnis' cloud-top, BBSS estimates of cloud position from relative humidity, precipitable and liquid water columns from the MWR, and the downwelling radiation observations from the BSRN, both solar and infrared. These "composite" plots, the whole series which is found in an appendix, are plotted for each of the 22 days of the IOP, and are intended to give a picture of the changes of surface radiation due to variable clouds and liquid water paths. There are a few things to keep in mind when looking at these plots.

1) **Clouds:** The sounding-measured relative humidities have been interpolated, and values greater than 50% have been plotted (shaded) to look like clouds. Because of the low threshold of relative humidity, it is likely that there are times and positions shaded when and where no clouds were present. cloud-bases from the MPL are plotted every minute (dots), while all four levels of cloud-top from Minnis are plotted so that they (bars) cover the whole hour. Note that Minnis cloud-top bars at zero meters mean no cloud detected, but bars located below zero are error flags. Usually the three cloud positions are consistent with each other (such as November 5), but sometimes (such as November 1), they are not.

2) **MWR:** The MWR plot includes measurements of vapor and liquid water path (LWP). MWR liquid water column measurements have been multiplied by 100 to fit on the same plot as the vapor column measurements. When the MWR liquid water column goes above 1 mm (100 units on the plot), it was assumed to be raining, so the complete set of MWR measurements was assumed to be in error. In these cases, neither the liquid and vapor values were plotted. Note that these data are from the original MWR measurements and not Jim Lilijgren's re-processed data. Also note that there is something really weird going on during November 14, where according to instrument logs, condensation occurred on the instrument itself. Most of the variability of the LWP can also be explained by rain (such as on October 30).

3) **BSRN:** The black line on the BSRN radiation plots is the calculated SWINC (ShortWave INCident at the top of the atmosphere, which is 0 during the nighttime). Even for very clear periods (such as November 6), the observed total solar is 25% lower than the SWINC due to absorption and scattering by gases and aerosols in the atmosphere. The BSRN plot is consistent (which is good) with the other two plots (clouds and MWR). When clouds appear (especially at low levels) the liquid water goes up, the direct and total hemispheric shortwave fluxes go down, and the diffuse shortwave and the downward longwave go up. For example, look at November 9. Another good example of this phenomena is about 11 UTC on October 29, when the downward longwave suddenly increased coupled with the onset of a cloud and a higher LWP.

4) **General:** There are spikes and jumps in the data. Some of these can be explained physically, while others are the result of bad data. For examples, the BSRN downward longwave plot of October 27 (11 UTC) has a little spike in the longwave, due to a short-lived cloud over the MPL, but the BSRN longwave spike on October 28 (around 15 UTC) is bad data. Spikes for BSRN shortwave data (like on November 10) are usually due to non-uniform clouds or partly cloudy skies.

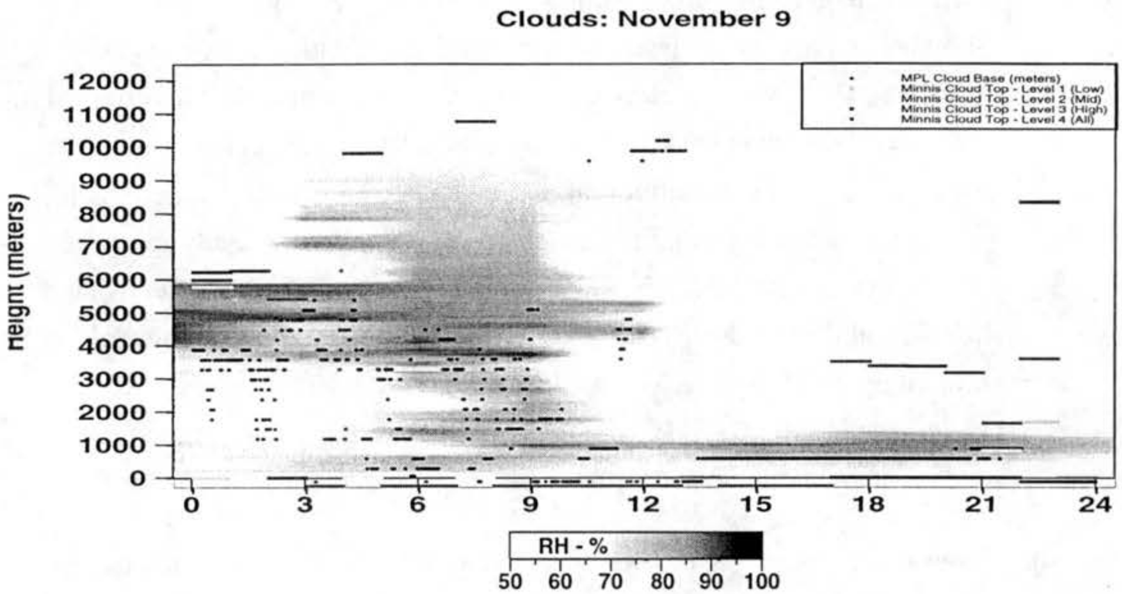
Clouds: November 9
MPL Cloud Base (meters)
Minnis Cloud Top - Level 1 (Low)
Minnis Cloud Top - Level 2 (Mid)
Minnis Cloud Top - Level 3 (High)
Minnis Cloud Top - Level 4 (All)
Height (meters)
RH - %
50 60 70 80 90 100

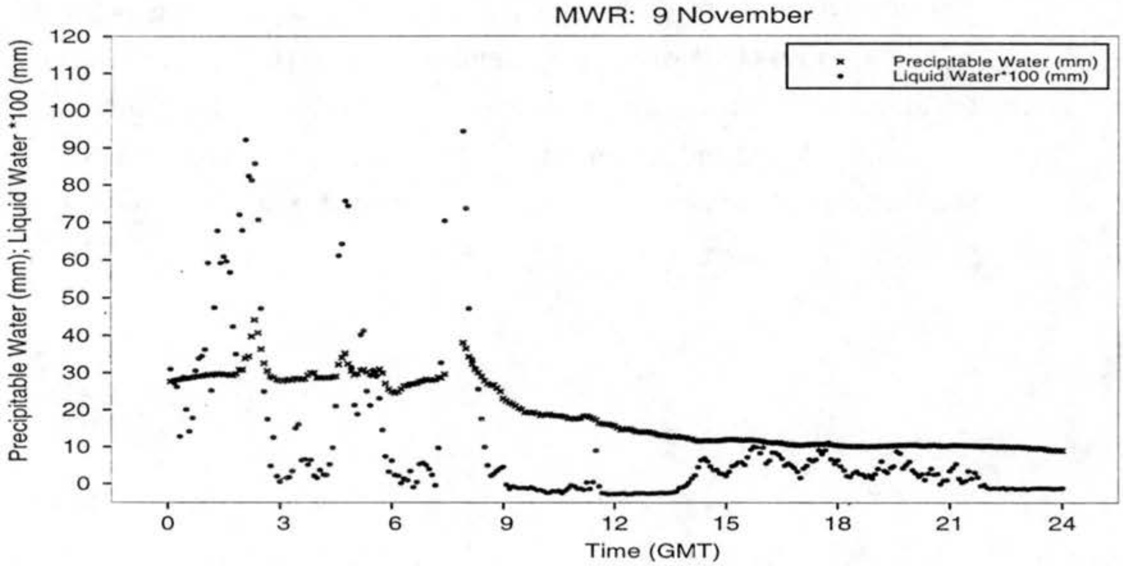
MWR: 9 November
Precipitable Water (mm)
Liquid Water*100 (mm)
Precipitable Water (mm); Liquid Water *100 (mm)
Time (GMT)

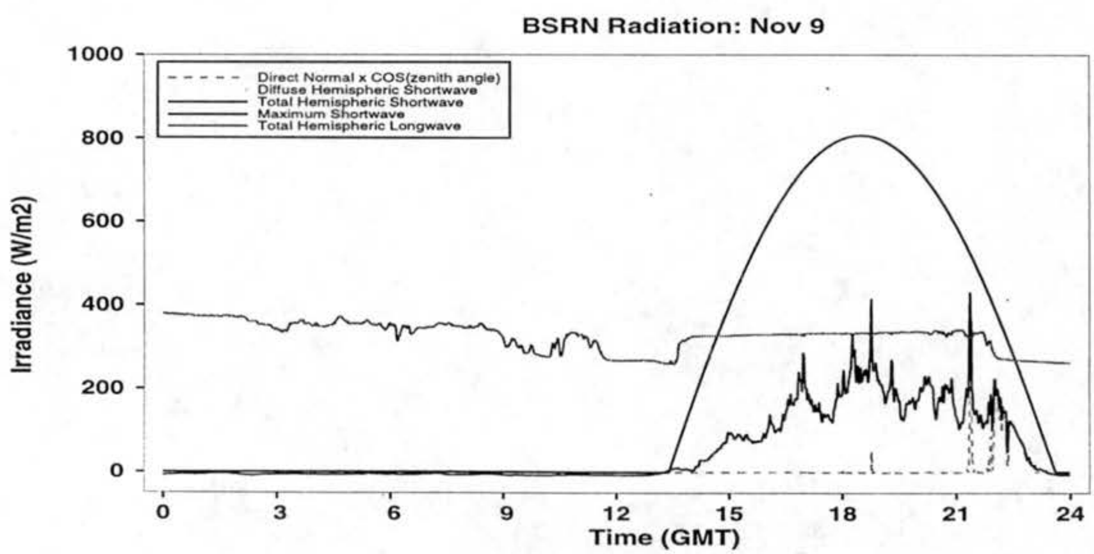
BSRN Radiation: Nov 9
Direct Normal x COS(zenith angle)
Diffuse Hemispheric Shortwave
Total Hemispheric Shortwave
Maximum Shortwave
Total Hemispheric Longwave
Irradiance (W/m2)
Time (GMT)

CHAPTER 6

The CSU GCM Radiation Parameterization

6.1 Background - GCMs, SCMs and Parameterizations

General Circulation Models (or Global Circulation Models - GCMs) are prognostic global models, designed to realistically and accurately model the circulation of the atmosphere and/or ocean. They either explicitly simulate or parameterize the individual processes (dynamic, thermodynamic, radiative transfer, etc.) and their interactions through use of differential equations and numerical integration. The domain of the model is often the whole globe and all time, but use of a computer means that the domain must be discretized into points in space and moments in time. The discrete horizontal intervals in space are known as *grid-boxes*, which are on the order of 200 km by 200 km for present atmospheric GCMs used for climate studies.

To realistically model atmospheric processes, GCMs must use a tremendous amount of computer time and power. Therefore, modelers need to decide what resolution and degree of detail are needed to meet climate modeling needs. *Parameterization* is a useful technique to calculate variables that are sub-grid scale (i.e. smaller than the discrete space and time grid of the computer model). Processes that are often parameterized in GCMs include cloud properties (cloud amount, base, optical depth, composition), precipitation, radiative fluxes and turbulent fluxes (Randall, 1994).

How do we test these parameterizations in a GCM? The obvious approach is to run the parameterization in the model and compare the results with observations. Unfortunately, because the model is so large and complex, there may be no way to attribute particular results to particular aspects of the model's formulation. Second, the simulation may be too computationally expensive or time consuming to make many model runs. Finally, because climate models represent averages in the atmosphere or ocean, and not individual systems, comparisons with observations can be difficult (Randall, 1994).

Therefore, this part of the report is about testing a radiation parameterization with the analyzed ARM data. In particular, the current CSU GCM radiation parameterization (Harshvardhan et al. 1987) was used. ARM data were fed into it at hourly intervals, and modeled results, such as fluxes and albedos were compared with observations from the Central Facility.

6.2 The Longwave Parameterization

For a clear atmosphere, the upward and downward fluxes at a pressure level p, integrated over a spectral range $\Delta\nu$ can be written as:

$$\begin{aligned} F_{clr}^{up}(p) &= B[T(p)] + G[p, p_s, T_s] - G[p, p_s, T(p_s)] \\ &+ \int_{T(p)}^{T(p_s)} \frac{\partial}{\partial T}(G[p, p', T(p')])\, dT(p') \end{aligned}, \tag{6.1}$$

and

$$F_{clr}^{down}(p) = B[T(p)] - G[p, p_t, T(p_t)] + \int_{T(p)}^{T(p_t)} \frac{\partial}{\partial T}(G[p, p', T(p')])\, dT(p'), \tag{6.2}$$

where

$$G[p,p',T] = \int_{\Delta\nu} \tau_\nu(p,p') B_\nu(T)\, d\nu, \tag{6.3}$$

$$B(T) = \int_{\Delta\nu} B_\nu(T)\, d\nu, \tag{6.4}$$

and

$$\frac{\partial}{\partial T}(G[p,p',T]) = \int_{\Delta\nu} \tau_\nu(p,p') \frac{\partial}{\partial T}(B_\nu(T))\, d\nu. \tag{6.5}$$

In these equations, $B_\nu(T)$ is the Planck function at temperature T and wavenumber ν, $\tau_\nu(p,p')$ is the diffuse transmittance between levels p and p', and subscripts s and t denote the surface and the top of the model. The radiative heating rate or divergence of the net flux is (see Equation 2.9):

$$\frac{dT}{dt} = \frac{g}{C_p}\frac{d}{dp}(F^{up} - F^{down}) \ , \tag{6.6}$$

where C_p is the specific heat of air at constant pressure and g is the graviational acceleration.

Because τ_ν varies greatly with wavenumber, the flux equations are too computationally expensive to integrate completely (via line-by-line integration). Therefore, the radiation parameterization uses approximate transmission calculations, known as *band models*. In other words, rather than add up each individual spectral line intensity for a broadband calculation, the model calculates a characteristic intensity for a spectral band of width $\Delta\nu$, thus saving computational resources. Observational evidence shows that the bulk of atmospheric transmission/absorption of longwave radiation is caused by only a few atmospheric constituents, H_2O, CO_2 and O_3. Also this transmission/absorption mostly occurs at a few key bands (Table 6.1). Atmospheric interactions with other longwave wavenumbers are considered small and thus neglected.

TABLE 6.1: Spectral "bands" used in the radiation parameterization. Regular angle numbers are wavenumber intervals (cm^{-1}), numbers in italics are wavelength intervals (μm).

H_2O	H_2O	CO_2	CO_2	O_3
Centers	**Wings**	**Center**	**Wings**	**Center**
0-340 / *inf-29.4*	340-540 / *29.4-19.5*	620-720 / *16.1-13.9*	540-620 / *18.5-16.1*	980-1100 / *10.2-9.1*
1380-1900 / *7.2-5.3*	800-980 / *12.5-10.2*		720-800 / *13.9-12.5*	
	1100-1380 / *9.1-7.2*			
	1900-3000 / *5.3-3.3*			

Cloudy sky calculations are more complicated than those for clear sky. If we assume that clouds are radiatively black at some wavelength and that the clouds completely cover the grid box, then we can use the same flux equations as before, but change the limits of integration (from cloud surface to cloud bottom, cloud-top to model top). Unfortunately, clouds are not black bodies, may only cover part of the grid box, and may span multiple atmospheric levels. Therefore, the parameterization's computational scheme considers cloud fraction as a measure of the probability of a clear line of sight, and adds certain multiplicative factors (to the flux equations 6.1 - 6.5 above) depending on the probability of a clear line of sight between model levels. Finally, the model includes a parameter specifying whether the clouds are "randomly" or "maximally" overlapped (Figs. 6.1 and 6.2). Under the assumption that clouds do not reflect longwave, and emit as gray bodies (characteristic emissivity over a large spectral interval), the model assigns a random overlap cloud fraction equal to their emissivity (e.g. the model treats a cloud with an emissivity of 0.5 the same as it would a black body cloud filling half the sky).

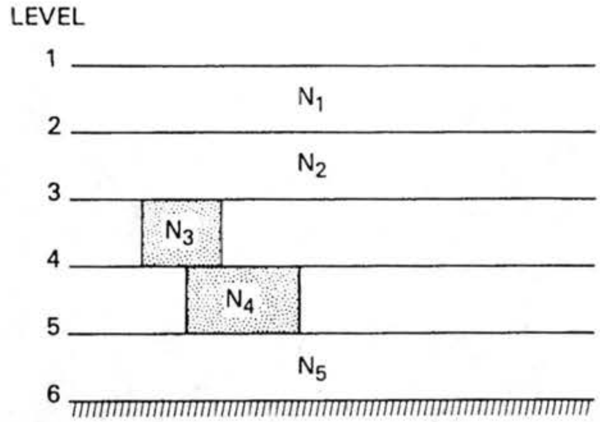

FIGURE 6.1: Schematic of Randomly Overlapped Cloud Layers (from Harshvardhan et al, 1987).

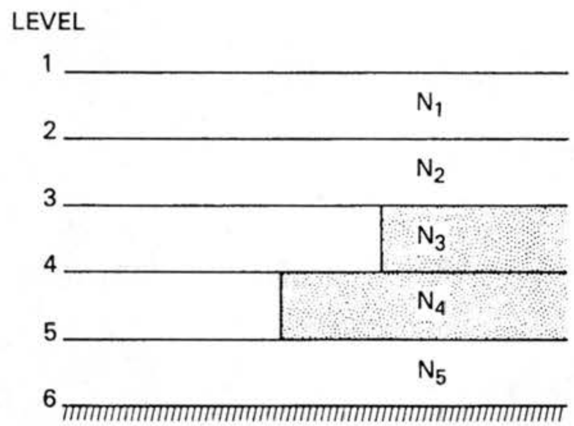

FIGURE 6.2: Schematic of Maximally Overlapped Cloud Layers (from Harshvardhan et al, 1987).

6.3 The Shortwave Parameterization

For the clear-sky shortwave parameterization the important atmospheric processes are water vapor absorption, ozone absorption, and clear-sky Rayleigh scattering (Lacis and Hansen, 1974). For the cloudy sky, cloud optical properties such as the solar zenith angle, cloud optical depth, albedo, and asymmetry factor (outlined in Chapter 2), are needed. To run the model we also need the incoming solar flux (insolation = solar constant * cosZ) and the four components of the surface albedo (diffuse/direct for visible/near infrared). With these parameters, the delta-Eddington model or two stream models (Harshvardhan, 1987) may be used to calculate reflection and transmission at each layer.

Without presenting details, the direct radiation reflected and transmitted by the *i*th layer may be considered sources of diffuse (non-directional) radiation for the next layer

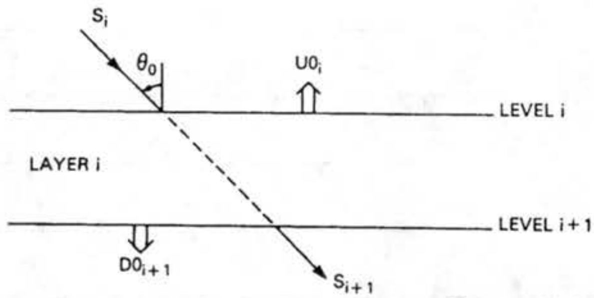

FIGURE 6.3: Schematic of solar radiation affecting ith layer in isolation. S is direct flux, U is reflected flux and D is diffuse flux.

(Fig 6.3). The sum of all subsequent transmission and reflection from all other layers, is the radiation in this *i*th layer.

6.4 General Use of the radiation parameterization

Parameterization inputs and how they are obtained are listed in Table 6.2.

TABLE 6.2: A list of needed inputs to the parameterization and how obtained.

Variable	Obtained by:
Vertical temperature and humidity profile	Soundings
surface (skin) temperature	SIROS or SMOS
cloud positions	MPL + Minnis + Soundings
Water mixing ratio in an atmospheric layer, C_w	1) obtain cloud positions 2) obtain LWP from MWR 3) Assume characteristic (linear) liquid distribution within the cloud
Solar insolation (solar zenith angle - μ_0)	Assume a solar constant and calculate zenith angle from date, time and latitude
Vertical ozone and CO_2 profiles	Climatology

TABLE 6.2: A list of needed inputs to the parameterization and how obtained.

Variable	Obtained by:
Surface Albedos	use Briegleb et al. (1986) formula with appropriate constants for surface type
Ice mixing ratio, C_i	1) obtain cloud positions 2) assume climatological ice-content value 3) Assume characteristic ice distribution
Cloud Optical Properties	calculate ε and τ by using cloud water and ice mixing ratios and assuming values of C_w, C_i, r_e, ω_0, and g

Specifically, we can calculate the surface albedos using

$$R(\mu) = R_0 \frac{(1+d)}{1+2d\mu}, \tag{6.7}$$

where μ is the cosine of the solar zenith angle (cosZ), R_0 is the diffuse surface albedo, and d is a parameter related to the surface type (Briegleb et al., 1986). For the generally "grassland" surface type of the ARM site, R_0 is taken to be 0.30 for visible and 0.10 for near-infrared, and d is set to 0.8.

The cloud optical properties are computed by a subroutine known as "elqclop.f" (Fowler and Randall, 1996), where we can manually change the cloud-particle effective radius, single scatter albedo and asymmetry constants (r_e, ω_0, g). Cloud optical depth for each layer is computed with the formula

$$\tau \sim \frac{3C}{2r_e}, \tag{6.8}$$

where C and r_e can stand for either ice or liquid values. Thus, the total cloud optical depth is the sum of the optical depths for all layers.

All nine items can then be inputted into the longwave and shortwave parameterizations described above, where

1) the surface radiative fluxes (Direct/Diffuse/Total Shortwave, Total Longwave for both Up/Down),

2) the radiative fluxes throughout the atmospheric column,

3) the vertical atmospheric heating profile, and

4) the whole sky solar albedos

are computed and we can compare with ARM observations such as the BSRN and Minnis' satellite retrievals.

Note that the parameterization was meant to be used as a "fast radiation parameterization" (Harshvardhan, 1987) and therefore it uses some major assumptions. Because it was specifically designed to study the earth's atmosphere near its present state, the parameterization is limited to the range of atmospheric parameters encountered in or near the atmosphere's present state. Trace atmospheric gases, including methane, freons, and nitrogen oxides are neglected, as are solar absorption by oxygen and carbon dioxide. For absorptive gases in the atmosphere, the model uses imprecise broadband approximations. Though known to be important to shortwave scattering, the parameterization neglects aerosols. Inputted clouds are assumed to have characteristic properties (asymmetry, effective radius) throughout the whole depth of the cloud and are considered maximally overlapped. Finally, the model omits longwave cloud reflection. The combination of all these assumptions could potentially produce large errors.

CHAPTER 7

Testing the Radiation Parameterization with ARM data

Incorporating ARM data into the parameterization theoretically should be a trivial job, because the data have been manipulated to one-hour intervals and a uniform vertical structure. However, because cloud properties are extremely difficult to measure, we should first examine "clear" sky cases and then the "cloudy" sky cases.

Inputted ARM data were from hourly intervals centered at half past the hour, so that for example, the 12:30 UTC observation is an "average" or "characteristic value" between 12:01 and 1:00 UTC. The parameterization was run with a uniform vertical 25 mb (39 levels total) grid, and a 10 mb (94 levels total) grid. (Figure 7.1). The carbon dioxide concentration was set to 355 ppmv and the climatological ozone profile shown in Fig. 7.2 was used. The surface albedos were estimated using the Briegleb et al. (1986) formula and the "grassland" surface type discussed in the previous chapter.

Because the SIROS data set was not available at all for a third of the IOP, and also because it included a substantial amount of questionable data, the SIROS data was scratched completely. The BSRN provided measurements of all downward broadband fluxes, but obtaining upward fluxes was a problem. The parameterization needed a surface "skin" temperature, which could be easily calculated from the downward (25 meter) pointing pyrgeometer data. But so not to use the SIROS data, the SMOS observations of

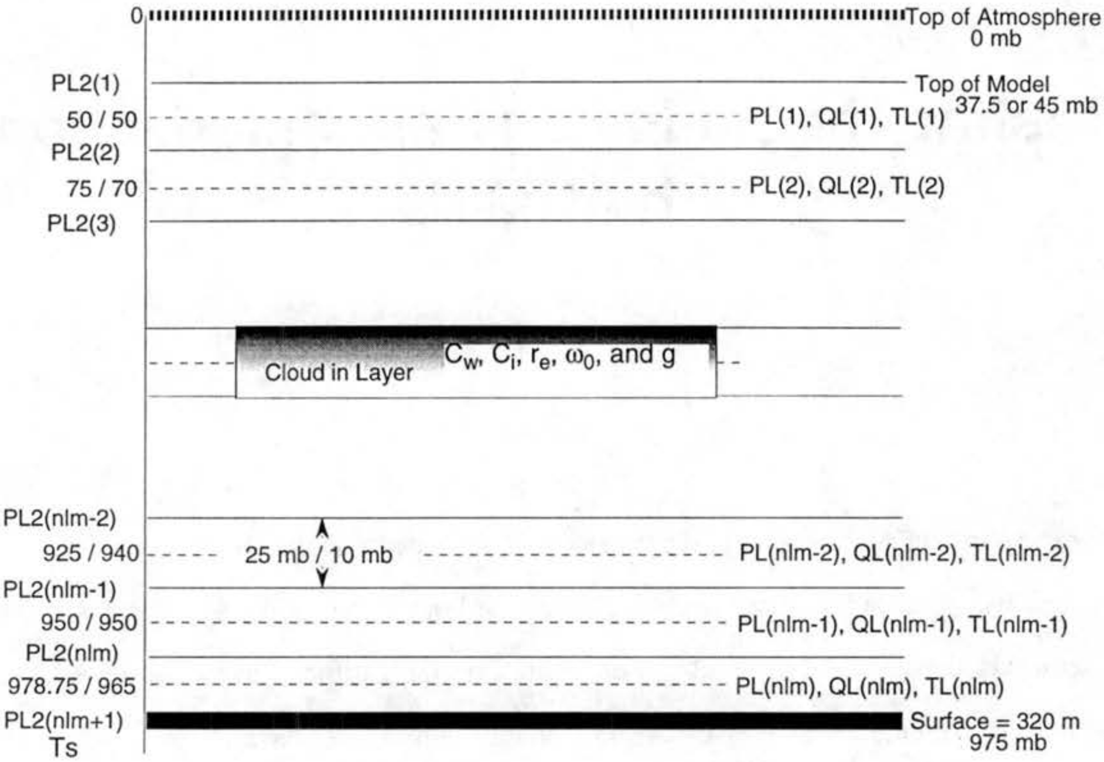

FIGURE 7.1: A schematic of the vertical grids (25 mb and 10 mb) used for the parameterization. There are nlm=39 levels (38 layers) for the 25 mb grid and nlm=94 levels (93 layers) for the 10 mb grid. PL2 (l) are the pressure at the boundaries of the layers, with PL(l), QL(l), and TL(l) the pressure, water vapor mixing ratio and temperature at the middle of the layers. The top (PL2(1)) of the model is at 37.5 mb for the 25 mb grid and 45 mb for the 10 mb grid. The surface pressure (example) is 975 mb, meaning that the lowest layer is a different thickness than the others. Along the left side of the figure are the pressures at the middle (PL(l)) of the layers (25 mb grid / 10 mb grid).

surface air temperature were assumed to be the skin temperature (see Chapter 5 for this discussion). Even though the air temperature is not the skin temperature, the high SMOS data quality permitted its use.

7.1 Clear Sky

We can define a "clear sky" case when the MPL detects no clouds during the hour interval (cloud fraction = 0). A total of 141 "clear sky" hours were observed during the IOP, of which 119 included no liquid water as well (meaning that both the MPL and the

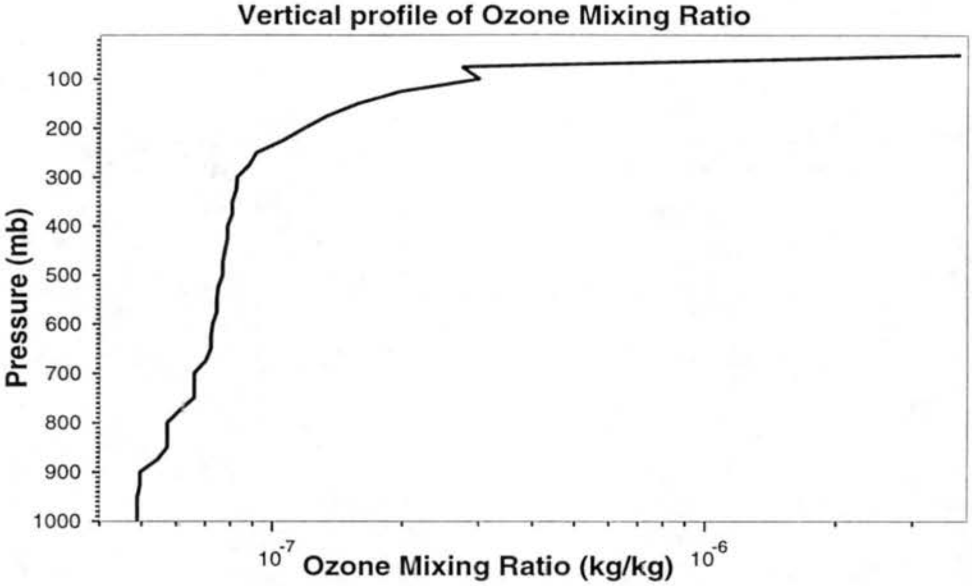

FIGURE 7.2: Climatological Ozone Profile used in the parameterization.

MWR agreed there was no cloud), and 18 of the remaining 22 hours observed liquid water paths of 0.02 mm (the MWR error average) or less. For each case, the parameterization was run using the sounding data, both for the 25 mb and the 10 mb grids. Fig. 7.3 compares both the shortwave and longwave fluxes computed by the model and observed by the BSRN for the 25 mb grid; Figure 7.4 is similar, but is calculated for the 10 mb grid. Changing from the 25 mb grid to the 10 mb grid caused a small, (but not-noticeable in the graphs) difference in all the fluxes. In all cases, the shortwave fluxes decreased, by up to 1.3 W-m^{-2} for the direct, 0.3 for the diffuse and up to 1.6 W-m^{-2} for the global. The outgoing (TOA) longwave was always decreased between 0.5 and 1.2 W-m^{-2}, while the downward surface longwave (net surface longwave) changed between -0.8 and +0.8 (+0.8 and -0.8) W m^{-2}.

Both shortwave plots have many points located close to (0,0), corresponding to night-time (no solar radiation), and many diffuse solar flux points far from the perfect fit line, probably corresponding to hours when a cloud was present in the sky that did not pass overhead of the MPL. The more interesting points are the direct and total solar flux points, where the calculated fluxes are 25-100 W-m^{-2} too high. Some of the difference is

(a)

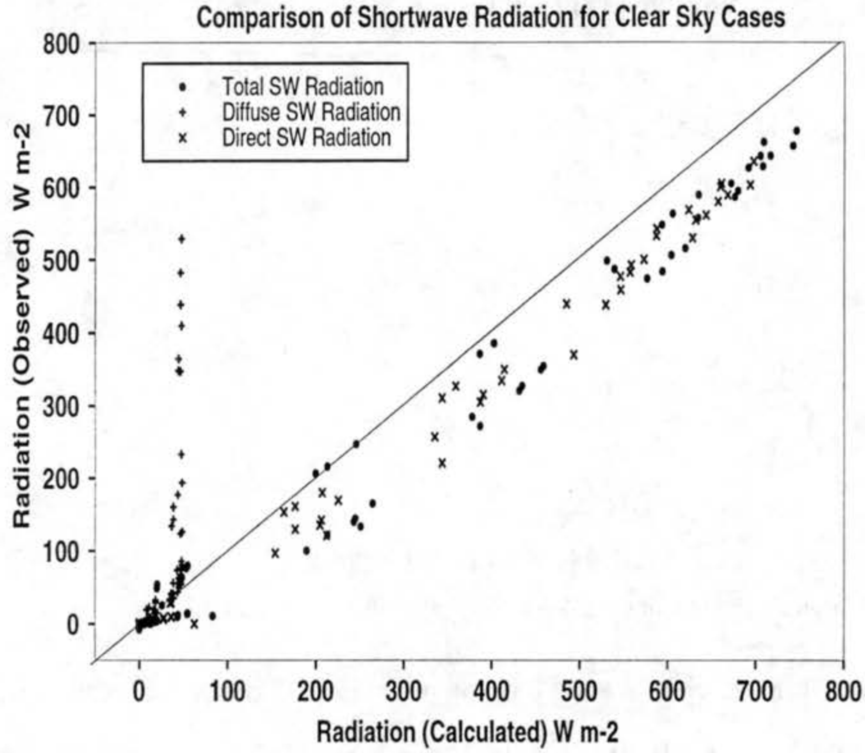

(b)

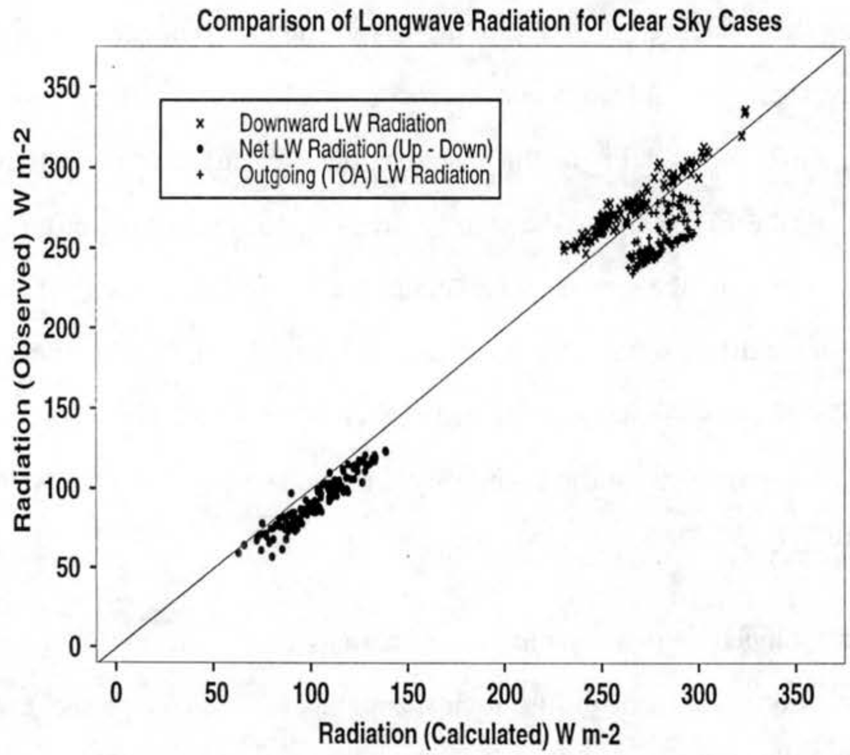

FIGURE 7.3: Comparison of modeled and observed Shortwave (a) and Longwave (b) Fluxes, for Clear Sky cases (MPL detects no clouds during the hour) for the 25 mb grid.

(a)

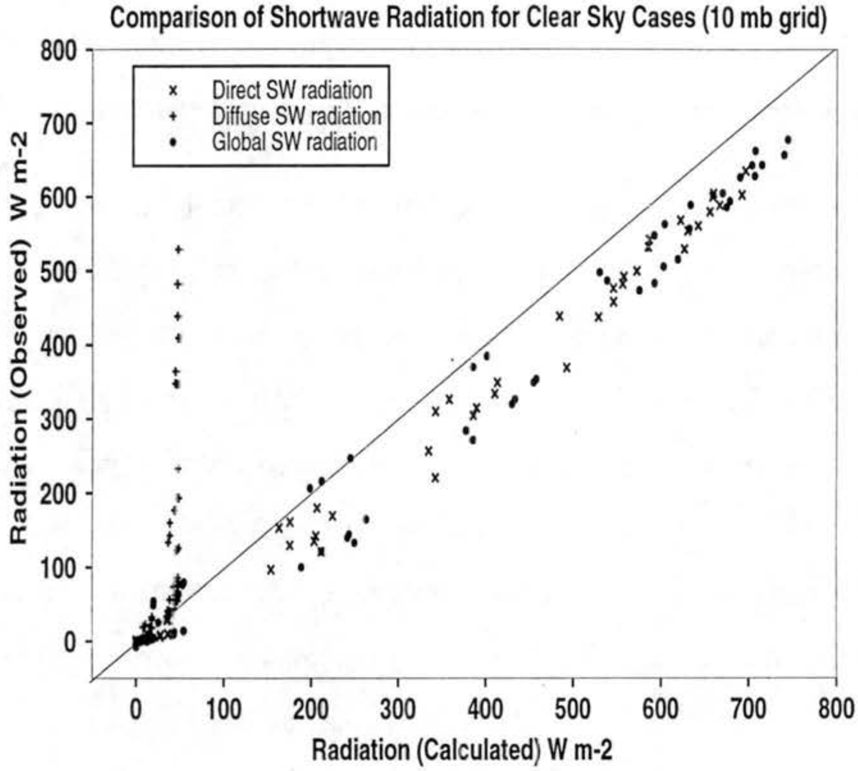

(b)

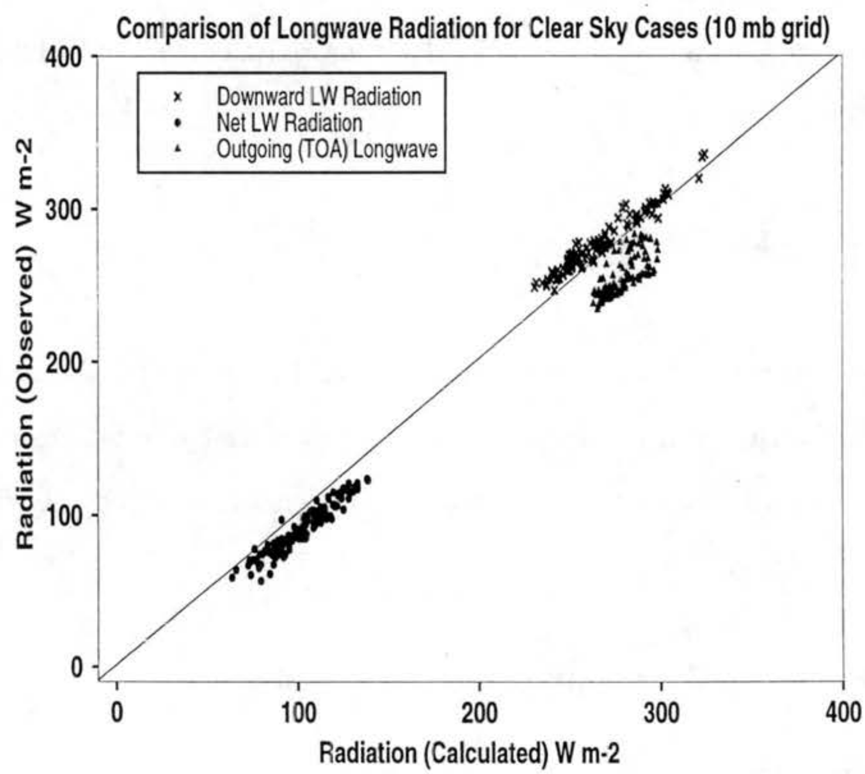

FIGURE 7.4: Comparison of modeled and observed Solar (a) and Longwave (b) Fluxes, for Clear Sky cases (MPL detects no clouds during the hour) for the 10 mb grid.

due to the parameterization not having any aerosols or trace atmospheric gases to absorb and scatter solar radiation. However, most of the error is probably due to mathematical simplifications and broadband approximations used in the parameterization.

Most points on the longwave plots are very close to the perfect fit line. However, most of the downward longwave points are observed lower than calculated, and because the upward longwave was plugged into the model, the net longwave (up - down) was observed higher than calculated. We might attribute some of the errors to a pyrgeometer (observation) bias, but more likely the errors are caused by broadband approximations and the simplified physics. Also from the graph, the outgoing (top of the atmosphere) longwave is consistently calculated lower than observed by Minnis' satellite retrievals. This means that the satellite is registering radiation from lower (warmer) down in the atmosphere than the parameterization would suggest. Some possible reasons are: the soundings' and climatology's estimates of water vapor high in the atmosphere are too low, that the atmospheric water vapor is modeled not absorptive enough, or that the satellite is calibrated incorrectly.

7.2 Cloudy Sky

Cloudy sky cases are far more complicated than clear sky and necessitated starting with simple cases. First, periods of liquid clouds having a constant base and top were attempted. Later, the model was run with ice clouds, with mixed phase clouds, and finally with multiple-level clouds.

7.2.1 Computing Cloud and Optical Parameters

7.2.1.1 Computing cloud-base and cloud-top

How should we obtain "characteristic" cloud-bases and tops for each hour? Either the

MPL or the satellite could be observing more than one cloud during the hour. If the MPL observed cloud-bases nearly the same throughout the hour, then we can assume one cloud-base. One way of deciding is using statistics. If the coefficient of variation of cloud base (CV equals the standard deviation divided by the mean) is less than 0.25, we can assume one cloud-base. If it is higher than we assume multiple cloud-bases. Table 7.1 lists MPL statistics from November 9. Comparing this table with the composite plot of No-

TABLE 7.1: cloud-base statistics from November 9.

Time (UTC)	mean (meters)	standard deviation (meters)	Coefficient of Variation	cloudfrac (%)
0	3850	93	0.02	1.00
1	3475	517	0.15	1.00
2	3215	734	0.23	1.00
3	3995	970	0.24	1.00
4	3580	1494	0.42	0.98
5	2500	1680	0.67	1.00
6	1606	0	0.00	0.92
7	2142	1823	0.85	0.98
8	1833	1229	0.67	0.95
9	2475	1118	0.45	1.00
10	2183	1111	0.51	0.53
11	968	1351	1.40	0.72
12	5124	3694	0.72	0.93
13	9935	125	0.01	0.92
14	1151	2287	1.99	0.53
15	570	0	0.00	1.00
16	570	0	0.00	1.00
17	570	0	0.00	1.00
18	570	0	0.00	1.00
19	570	0	0.00	1.00
20	570	0	0.00	1.00
21	665	141	0.21	1.00
22	839	91	0.11	1.00

TABLE 7.1: cloud-base statistics from November 9.

Time (UTC)	mean (meters)	standard deviation (meters)	Coefficient of Variation	cloudfrac (%)
23	870	0	0.00	0.02
24	-30	0	0.00	0.00

vember 9, shows that the CV = 0.25 is a reasonable cutoff for cloud-base uniformity.

We can put forward the same type of argument for Minnis' cloud-top. If all cloud-tops (that is level 1, 2, and 3) are fairly similar to each other, (for example look at 1 UTC at Table 7.2 below) then there is only one cloud-top for the hour and we can use the height given under top4). Together with estimates of cloud-base from the MPL, and the

TABLE 7.2: November 9: Cloud Fraction and cloud-top from Minnis.

hr UTC	amount1 (%)	amount2 (%)	amount3 (%)	amount4 (%)	top1 (m)	top2 (m)	top3 (m)	top4 (m)
0	0.00	0.00	0.00	0.00	-999	-999	-999	-999
1	0.00	53.45	46.55	100.00	0	5770	6230	5990
2	0.00	0.00	100.00	100.00	0	0	6270	6270
3	0.00	100.00	0.00	100.00	0	5400	0	5400
4	0.00	0.00	0.00	0.00	-999	-999	-999	-999
5	0.00	0.00	100.00	100.00	0	0	9810	9810
6	0.00	0.00	0.00	0.00	-999	-999	-999	-999
7	0.00	0.00	0.00	0.00	-999	-999	-999	-999
8	0.00	0.00	100.00	100.00	0	0	10760	10760
9	0.00	0.00	0.00	0.00	-999	-999	-999	-999
10	0.00	0.00	0.00	0.00	-999	-999	-999	-999
11	0.00	0.00	0.00	0.00	-999	-999	-999	-999
12	0.00	0.00	0.00	0.00	-999	-999	-999	-999
13	0.00	0.00	0.00	0.00	-999	-999	-999	-999
14	0.00	0.00	0.00	0.00	0	0	0	0
15	0.00	0.00	0.00	0.00	-999	-999	-999	-999
16	0.00	0.00	0.00	0.00	-999	-999	-999	-999

TABLE 7.2: November 9: Cloud Fraction and cloud-top from Minnis.

hr UTC	amount1 (%)	amount2 (%)	amount3 (%)	amount4 (%)	top1 (m)	top2 (m)	top3 (m)	top4 (m)
17	0.00	0.00	0.00	0.00	-999	-999	-999	-999
18	0.00	100.00	0.00	100.00	0	3500	0	3500
19	0.00	100.00	0.00	100.00	0	3370	0	3370
20	0.00	100.00	0.00	100.00	0	3360	0	3360
21	0.00	100.00	0.00	100.00	0	3160	0	3160
22	48.28	31.03	0.00	79.31	810	2960	0	1650
23	8.00	6.00	4.00	18.00	1690	2950	8330	3590

cloud fraction (either from the MPL or Minnis) we have a reasonable vertical profile of the cloud during the hour. For example, for November 9, at 19 UTC, both Minnis and the MPL observed a cloud fraction of 100%, the cloud-base was put at 570 meters and the cloud-top at 3370 meters.

If we assume that whenever the relative humidity is "high" there is a cloud, then we can also calculate cloud-bases and tops from the soundings. What is a "high" relative humidity? Unfortunately, as the sonde rises into colder temperatures and lower pressures, its measurements of relative humidity are less accurate. Following trial and error and attempting to be as simple as possible, here are some reasonable thresholds of relative humidity to indicate a cloud in a layer with a particular pressure (Table 7.3).

TABLE 7.3: Sufficient Pressure/Humidity combinations in an atmospheric layer to assume a cloud is present.

If Pressure is less than... (mb)	Then humidity must be greater than (%)
1000	95
900	90
800	85
700	80
600	75
500	70

TABLE 7.3: Sufficient Pressure/Humidity combinations in an atmospheric layer to assume a cloud is present.

If Pressure is less than... (mb)	Then humidity must be greater than (%)
400	65
300	60
150	55

7.2.1.2 Ice and Water Distribution in the Cloud

Once we do have the cloud-top and base, how do we distribute the water (or ice) in the cloud? How do we know whether a cloud is water or ice? One study (Slingo et al., 1980) showed that distributions in liquid water clouds are linear, with largest values of liquid water content at the top of the cloud. Ice profiles can be profiled also as linear (Figure 7.5), but with largest values of ice water content at the bottom of the cloud (Stackhouse and Stephens, 1989). Whether a cloud is water or ice or both, depends on many

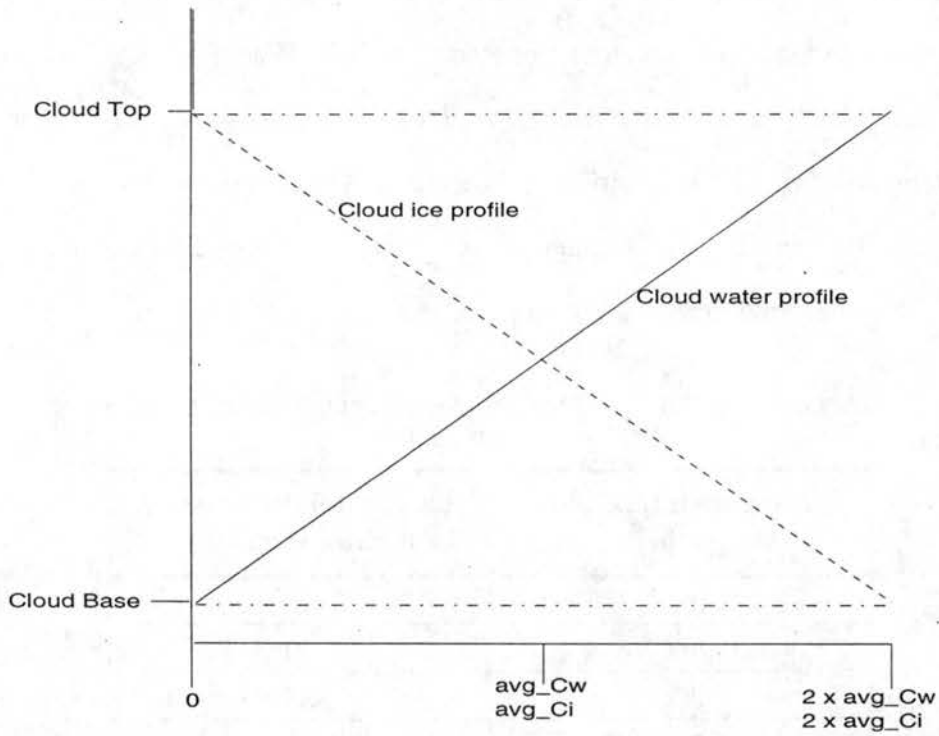

FIGURE 7.5: Liquid water profile, C_w, (solid line) for water clouds and Ice profile, C_i (dotted line), for ice clouds.

factors (temperature, pressure, horizontal wind, vertical wind, liquid or ice content, aerosol concentrations, etc.) but for simplicity, we can let temperature be the deciding factor. If a cloud is completely confined to levels warmer than 253 K (-20°C) then it is all water, while if it was located in levels all colder than 253 K (-30°C) then we can assume it is ice. If the cloud straddles 253 K, then it is *mixed-phase*, composed of both water and ice.

For water clouds, we distribute the Liquid Water Path (LWP) using the following procedure:

1) Convert cloud levels from meters to millibars by obtaining the temperatures and humidities from the soundings and applying the hypsometric equation;
2) Calculate cloud thickness in millibars (cloud-base - cloud-top);
3) Calculate an "average" cloud water (in kg/kg) for the cloud:

$$\overline{C_w} = \frac{LWP}{1000} g\rho_{liq} \left(\frac{1}{100dP_{cloud}}\right), \tag{7.1}$$

where g is 9.8 m s^{-1}, ρ_{liq} is 1000 kg m^{-3} and dp_{cloud} is the cloud thickness.

4) Assume a linear distribution for cloud water content, so that $C_w = 0$ at the bottom and $C_w = 2\,\overline{C}_w$ at the top of the cloud:

$$C_w = \overline{C}_w \left(\frac{P_b - P}{P_m - P_t}\right), \tag{7.2}$$

where p_b is the pressure at the bottom of the cloud, p_t is the pressure at the top, p_m is the pressure at the middle of the cloud, and p is the pressure of the layer in question. For layers with no cloud, there is no cloud water.

For ice clouds, there were no observations of ice path or ice content in the ARM datasets, so we need "reasonable" values of ice water content. Reasonable values of ice content in the middle of the cloud are between 10^{-6} and 10^{-4} kg m^{-3} (Stackhouse and Stephens, 1989; Dowling and Radke, 1990). Heymsfield and Platt (1984) and Platt and Harshvardhan (1989) showed that ice content is dependent on temperature (see Fig. 7.6).

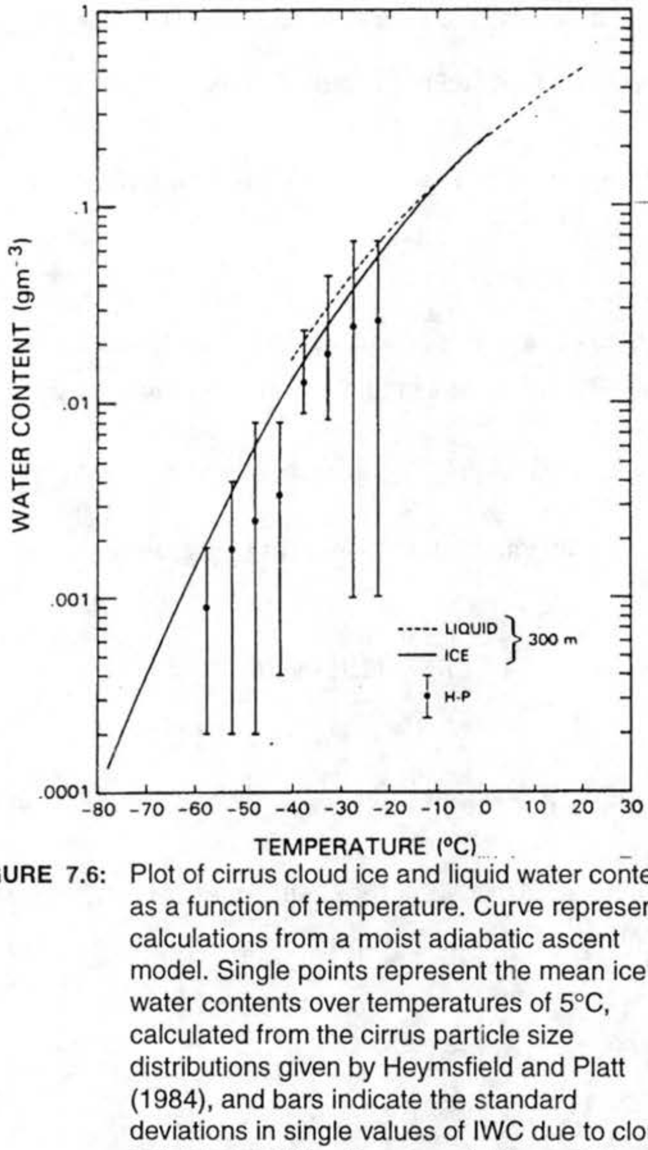

FIGURE 7.6: Plot of cirrus cloud ice and liquid water contents as a function of temperature. Curve represents calculations from a moist adiabatic ascent model. Single points represent the mean ice water contents over temperatures of 5°C, calculated from the cirrus particle size distributions given by Heymsfield and Platt (1984), and bars indicate the standard deviations in single values of IWC due to cloud natural variability. (figure copied from Platt and Harshvardhan, 1989).

In the spirit of these two papers, we can relate cloud center ice water contents to temperature (see Table 7.4). The average ice mixing ratio can then be found by:

TABLE 7.4: Relation between cloud center temperature and ice content of a cloud.

If the cloud center temperature is within 2.5° of	...then this is the default Ice Content ($g\ m^{-3}$)
223	0.001
228	0.002
233	0.004
238	0.008
243	0.016
248	0.032
253	0.064

$$\overline{C}_i = IWC\left(\frac{100\,(p_{sfc} - p_m)}{g\,(Z_m)}\right), \tag{7.3}$$

where p_{sfc} is the surface pressure, and p_m and Z_m are the pressure and height of the middle of the cloud, respectively. Again we can assume a linear water distribution, except the ice distribution is reversed from the liquid; $C_i = 0$ at the top and $C_i = 2\,\overline{C}_i$ at the bottom of the cloud:

$$C_i = \overline{C}_i\left(\frac{p - p_t}{p_b - p_m}\right). \tag{7.4}$$

For mixed clouds, there is no way to know anything about the distribution of ice or water from the ARM data, so we might assume that the liquid water path is distributed through the cloud like as in the water cloud case, and that the ice path is distributed like as in the ice cloud case.

How good are all of these assumptions for cloud water or ice distribution? To see if we are the right track, we can compute the all sky shortwave albedos using the radiation parameterization and compare them with top of the atmosphere observations from Pat

Minnis Satellite cloud retrievals. Without changing the default optical parameters (this is done in the next section) and calculating only daytime values, Fig. 7.7 shows SW albedos as a function of cloud type, when the clouds were of a single layer. Table 7.5 shows

TABLE 7.5: Correlation and regression line fits for calculated versus observed whole sky shortwave albedo as a function of cloud layer type, for MPL - Minnis and Sonde-derived cloud positions.

		MPL - Minnis			Sonde	
TYPE	**# Cases**	**correlate**	**Regression Equation**	**# Cases**	**correlate**	**Regression Equation**
Clear	42	.72	Obs = .56 Calc + .10	38	.77	Obs = .58 Calc + .10
Liquid	42	.81	Obs = 1.15 Calc - .03	24	.88	Obs = 1.12 Calc - .02
Ice	15	.41	Obs = .40 Calc + .13	14	.15	Obs = .10 Calc + .22
Mix	23	.80	Obs = 1.72 Calc - .30	35	.79	Obs = 1.06 Calc + .04

the correlation and regression equations for each color dot on the albedo figures. Obviously, the model handles "clear" and liquid water-only clouds pretty well. What is interesting about the "clear" cases is that while the correlation between observed and calculated is high (for both the sonde and the MPL - Minnis), the regression line is sloped so that the model under-calculates albedo when the albedo is low (small zenith angle) and over-calculates when the albedo is high (large zenith angle). This could mean that the Briegleb et al. (1986) model's zenith-angle dependence is too strong or that used poor values for R_0 and d were used. For the liquid-only cases, the correlations are very good, and the regression line falls almost on the one-to-one line.

Ice clouds, however, are another matter. Even with using the modified Heymsfield and Platt (1984) relation for ice content versus temperature, the calculations do not model the observations very well. The correlation is low, and the regression line is not close to the one-to-one line. Possibly this is due to the small number of ice-only observations, but more likely, the bad fits are due to erroneous ice contents and simplified assumptions of cloud optical parameters.

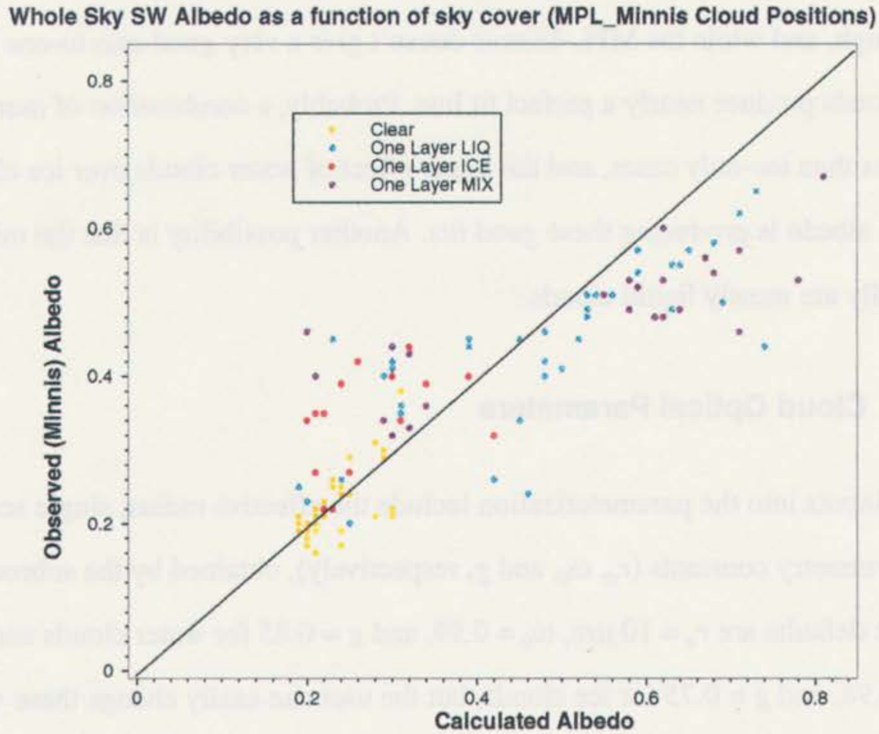

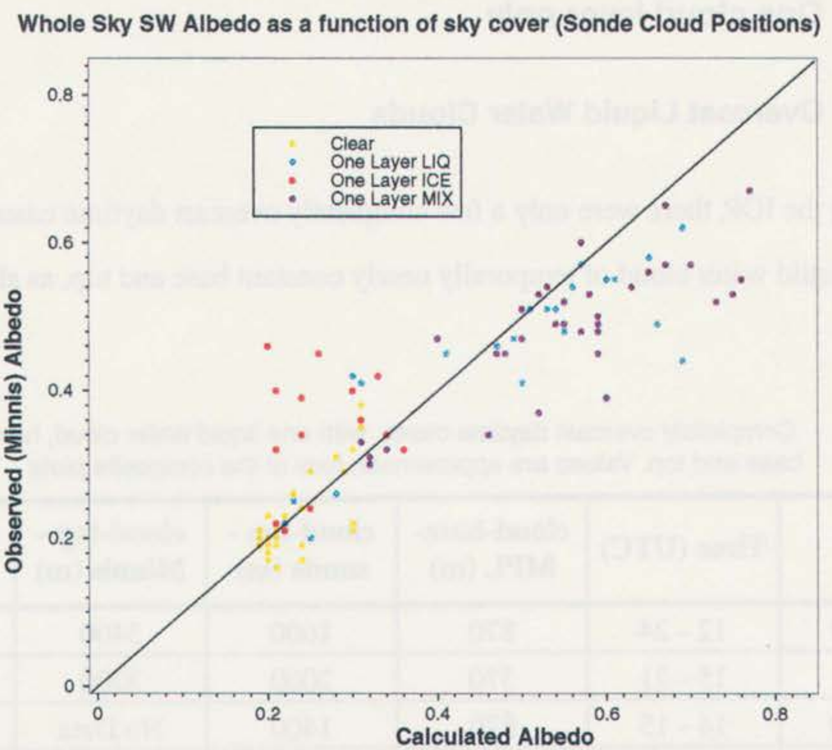

FIGURE 7.7: A comparison of Top of the Atmosphere albedos as a function of type of single cloud layer with cloud positions derived from MPL-Minnis (top) and Sonde (bottom).

Interestingly, albedo data fits for the mixed-phase clouds are pretty good. The correlations are high, and while the MPL-Minnis doesn't give a very good one-to-one fit, sonde derived clouds produce nearly a perfect fit line. Probably, a combination of more mixed-phase cases than ice-only cases, and the larger effect of water clouds over ice clouds on shortwave albedo is producing these good fits. Another possibility is that the mixed clouds really are mostly liquid clouds.

7.2.1.3 Cloud Optical Parameters

Other inputs into the parameterization include the effective radius, single scatter albedo and asymmetry constants (r_e, ω_0, and g, respectively), obtained by the subroutine elqclop.f. The defaults are $r_e = 10$ µm, $\omega_0 = 0.99$, and $g = 0.85$ for water clouds and $r_e = 30$ µm, $\omega_0 = 0.98$, and $g = 0.75$ for ice clouds, but the user can easily change these values.

7.2.2 One cloud layer only

7.2.2.1 Overcast Liquid Water Clouds

During the IOP, there were only a few completely overcast daytime cases having only one liquid water cloud of temporally nearly constant base and top, as shown in Table 7.6.

TABLE 7.6: Completely overcast daytime cases, with one liquid water cloud, having constant base and top. Values are approximate, look at the composite plots

Date	Time (UTC)	cloud-base-MPL (m)	cloud-top - sonde (m)	cloud-top - Minnis (m)	LWP (mm)
Oct 29	12 - 24	870	1600	3400	.3
Nov 9	15 - 21	570	2000	3200	.07
Nov 10	14 - 15	870	1400	No Data	.02
Nov 11	14 - 17	570	1000	4000	.05

We can easily change the effective radius, single scatter albedo and asymmetry parameter (defaults are $r_e = 10\ \mu m$, $\omega_0 = 0.99$, and $g = 0.85$). Figs. 7.9 through 7.9 (for November 9, 19 UTC) show how changing the cloud dimensions and the particle optical properties affects different radiative fluxes. Raising the cloud-base acts to lower the diffuse and total solar fluxes, while raising the cloud-top, the single scatter albedo, the asymmetry constant, or the effective radius tends to increase the diffuse and total solar fluxes (Figs. 7.9 and 7.9). The downwelling longwave flux is dependent on cloud-base, and surprisingly, extremely dependent on cloud-top level. The parameterization assumes no scattering or reflection in the longwave, so both the downwelling and the outgoing longwave are not dependent on either the single-scatter albedo or the asymmetry parameter. However, the longwave plots show opposite effects of increasing the effective radii of the cloud particles; the downwelling flux is decreased with increasing radii and the outgoing flux is increased. For all four flux plots, the most confusing aspect is the "step" characteristic when raising cloud-top, which occurs when we raise the cloud-top by 200 meter increments, sometimes straddling the 25 mb pressure layer. This "step" characteristic does not happen when we raise cloud-bases by 50 meter increments, because the magnitude of the cloud-base change is much smaller than the 25 mb increments of the model. Note that the dotted line represents "calculated" values, with the solid line "observed" values in the first figure, but the opposite for the other three figures.

7.2.2.2 Overcast Ice Clouds

Like the liquid only cloud cases in the section above, there were very few daytime periods of completely overcast, uniform ice only clouds during the IOP (Table 7.7).

Similarly to the liquid cloud case, we can change the effective radius, single scatter albedo and asymmetry constants (r_e, ω_0, and g, respectively), with the ice defaults being $r_e = 30\ \mu m$, $\omega_0 = 0.98$, and $g = 0.75$

9 Nov, 19 GMT: Diffuse Solar Flux as a Function of Individual Cloud Optical Parameters:

Defaults: Cloud Base: 570 m; Cloud Top: 2000 m; SingleScatterAlbedo: .99; Asymmetry: .85; Effective Radius: 10 microns

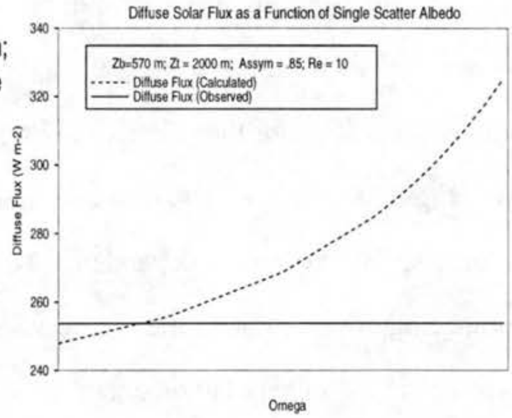

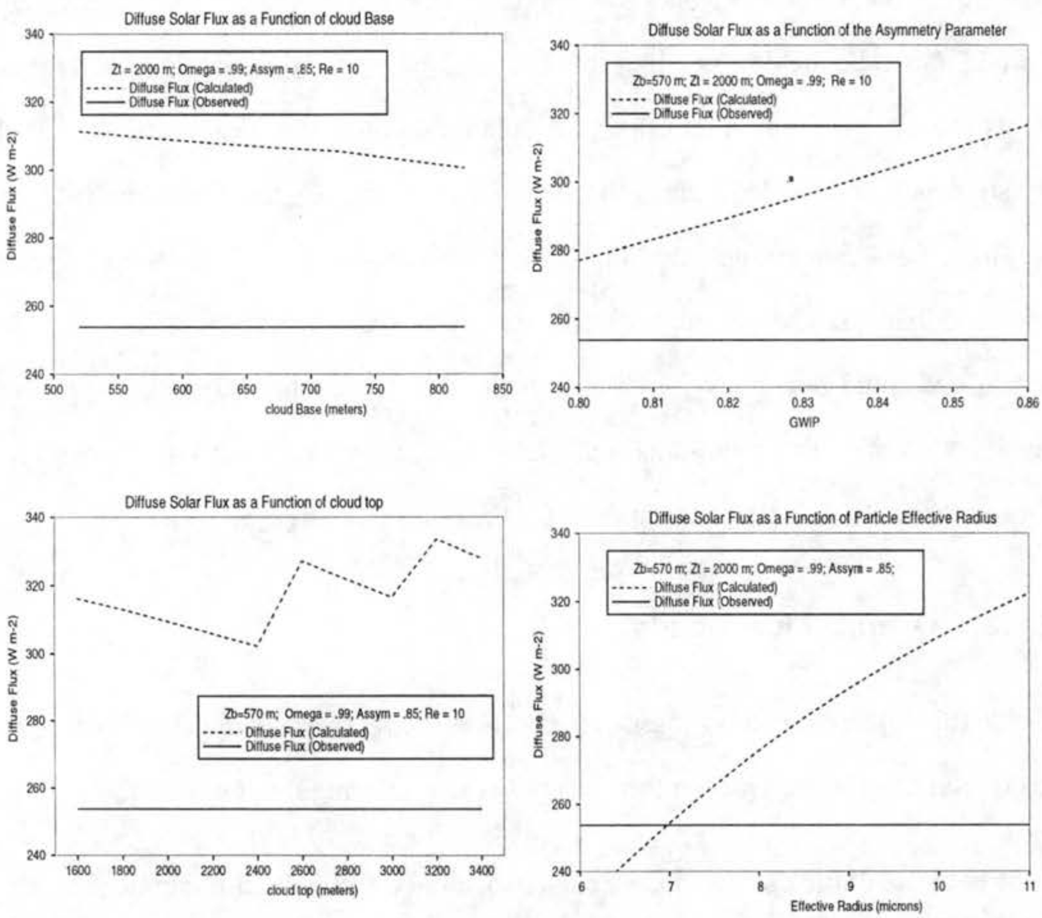

FIGURE 7.8: Diffuse Solar Flux as a function of Cloud Optical Parameters. For each graph, four parameters are held constant, while one is varied. For November 9 @ 19 UTC.

9 Nov, 19 GMT: Total SW Flux as a Function of Individual Cloud Optical Parameters:

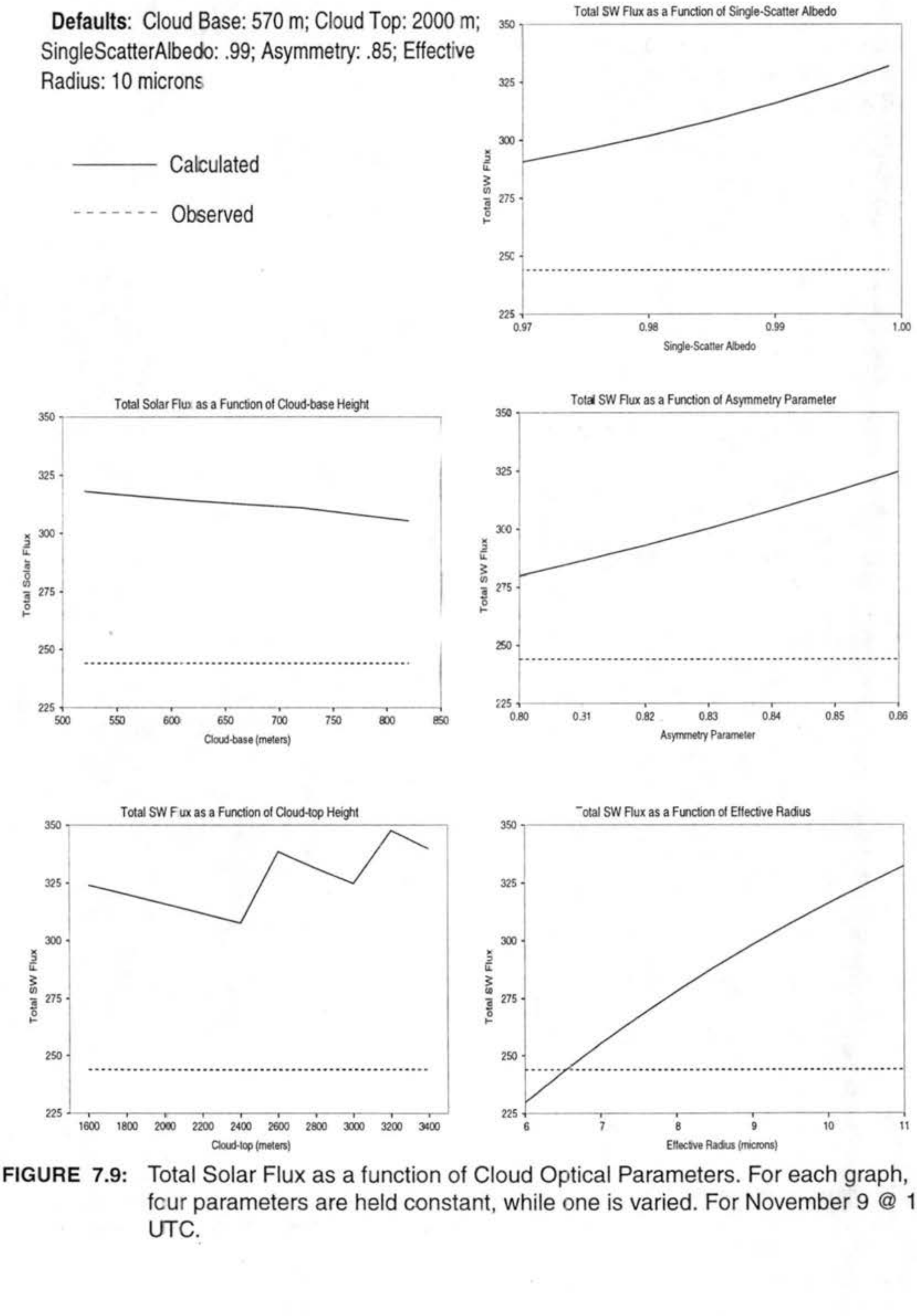

FIGURE 7.9: Total Solar Flux as a function of Cloud Optical Parameters. For each graph, fcur parameters are held constant, while one is varied. For November 9 @ 19 UTC.

9 Nov, 19 GMT: Downward LW Flux as a Function of Individual Cloud Optical Parameters:

Defaults: Cloud Base: 570 m; Cloud Top: 2000 m; SingleScatterAlbedo: .99; Asymmetry: .85; Effective Radius: 10 microns

——— Calculated

- - - - - - Observed

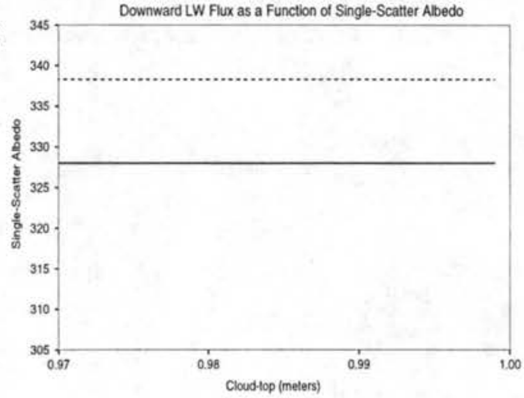

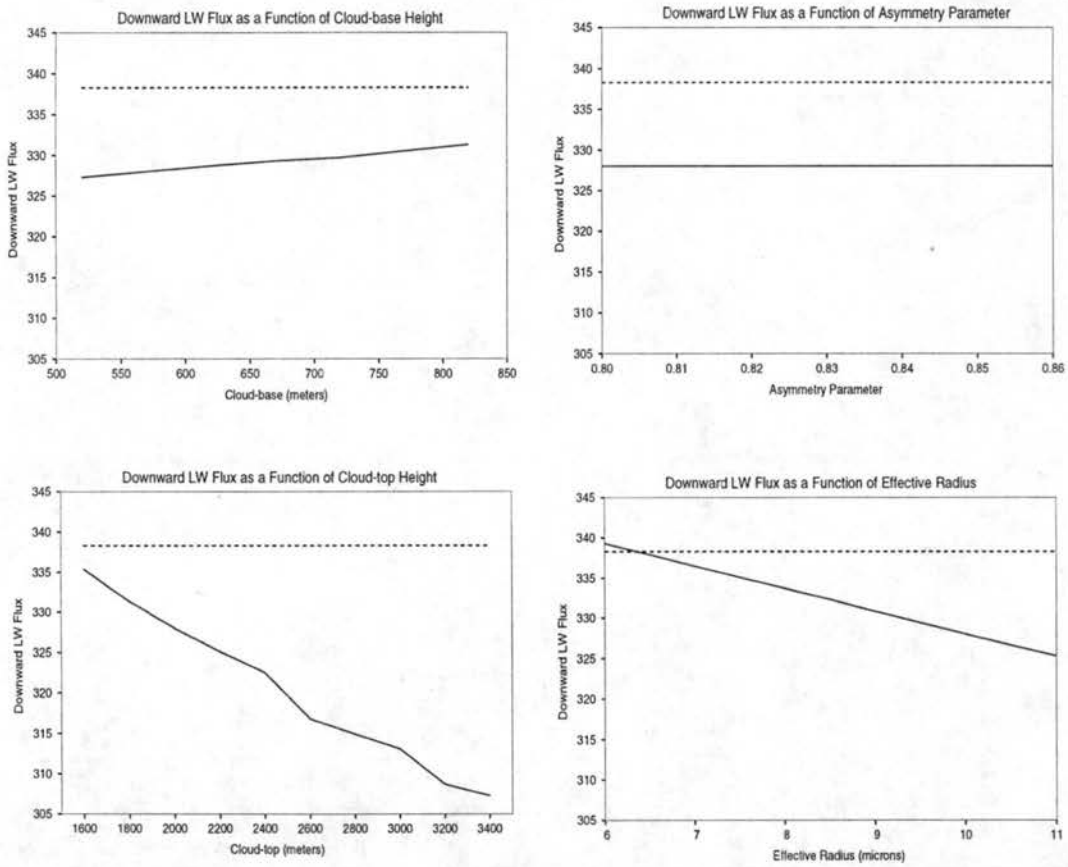

FIGURE 7.10: Downwelling LW Flux as a function of Cloud Optical Parameters. For each graph, four parameters are held constant, while one is varied. For November 9 @ 19 UTC.

9 Nov, 19 GMT: Outgoing (TOA) LW Flux as a Function of Individual Cloud Optical Parameters:

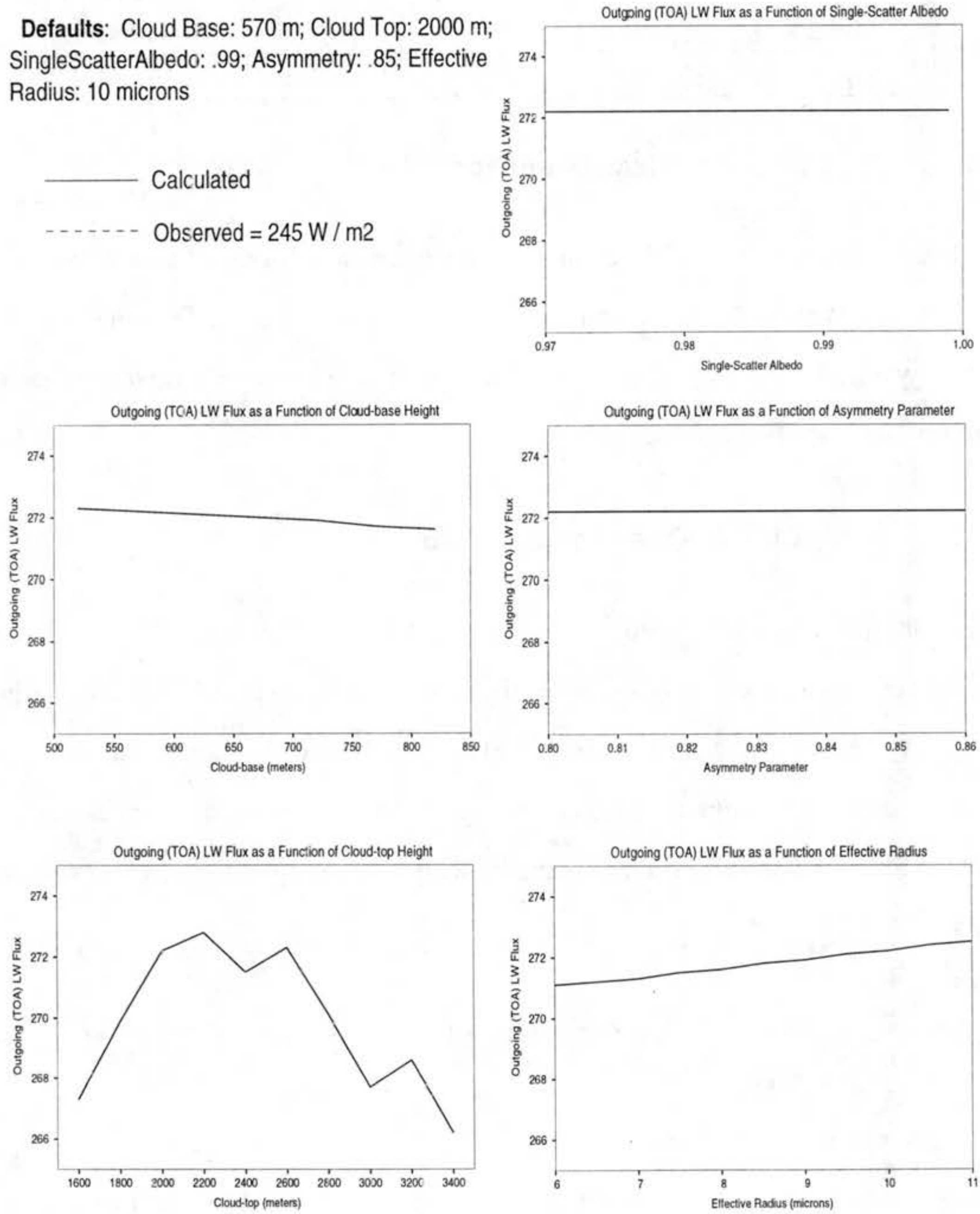

FIGURE 7.11: Outgoing (TOA) LW Flux as a function of Cloud Optical Parameters. For each graph, four parameters are held constant, while one is varied. For November 9 @ 19 UTC.

TABLE 7.7: Completely overcast daytime cases, with one ice cloud, having constant base and top. Values are approximate, look at the composite plots.

Date	Time (UTC)	cloud-base-MPL (m)	cloud-top - sonde (m)	cloud-top - Minnis (m)
Nov 1	14	8500	---	6000
Nov 1	15-19	9200	---	11200
Nov 2	17 - 18	7000	9000	11000
Nov 2	19 - 20	5000	10000	11000

7.2.2.3 Overcast, One Mixed Liquid/Ice Cloud

Clouds at middle levels of the atmosphere are often *mixed phase*, that is, having both liquid and ice. We can define a mixed-phase cloud as a cloud that straddles the 253° K line. Fairly uniform (both cloud-base and cloud-top) mixed-phase clouds were detected on November 3 and November 5.

7.2.2.4 Partly Cloudy, One - Level: Whole IOP

The difference between "overcast" and "partly cloudy" is the value of the cloud fraction. For completely overcast cases above, the cloud fraction is set to 1.00. For a partly cloudy sky, the cloud fraction is between 0.00 and 1.00. Basically, the parameterization "weights" the absorption/transmission of the cloud by the cloud fraction. For example, if the cloud fraction is *cloudfrac*, then the model scales the absorption/transmission by computing

$$Effect = cloudfrac \times OvercastEffect + (1 - cloudfrac) \times ClearEffect \qquad \textbf{(7.5)}$$

where *Effect* is the result of having a certain fraction and type of cloud in the atmosphere, and *OvercastEffect* is the effect a type of cloud would have if it covered the whole sky. The Overcast Effects are different for the MPL/Minnis-derived cloud positions than for the sonde-derived cloud positions. The following graphs (Figs 7.13

and 7.13) show cases when both the cloud-base and cloud-top can be computed, there is one measurement for each, and the base is below the top for the MPL-Minnis measurements. The fluxes on Fig. 7.13 are computed with cloud positions derived by the MPL and Minnis, while on Fig. 7.13 are computed by the sounding. The graphs marked (a) compare the shortwave fluxes, while graphs marked (b) show the longwave fluxes. Red symbols are daytime and blue are nighttime comparisons. Note that these graphs use the default values for single scatter albedo, asymmetry factor, and effective radius (0.99, 0.85, and 10 μm for water and 0.98, 0.75, and 30 μm for ice clouds)

The first thing to notice on these plots is that the day/night bias has disappeared. In other words, using the surface air temperature instead of the surface skin temperature was not a completely bad assumption. Note that fluxes computed on the 10 mb grid are very similar to those on the 25 mb grid. As with the clear sky cases above, the downward LW fluxes are calculated too low and the outgoing (Top of Atmosphere) LW fluxes are calculated too high. However, looking at the longwave plots closely, the calculations made using the sonde tend to straddle the perfect fit line more than the calculations made with the MPL and Minnis cloud positions. For the shortwave plots, the results are more mixed; the MPL/Minnis cloud positions tend to produce fluxes that average to the best-fit line, yet deviate farther from the line.

Another way to look at the same data is to split them into sky cover type. Figures 7.14 and 7.15 show longwave and shortwave plots on the 25 mb grid for both MPL-Minnis and sonde-derived cloud positions, split into categories: "clear," "one cloud-liquid only," "one cloud- ice only," and "one cloud-mixed." At first glance, the plots using the sounding clouds and the MPL - Minnis clouds are very similar (just as Figures 7.13 and 7.13 showed before), and the sounding clouds give results that are more clustered together. However, it is more interesting to note the quality of fit within the different cloud categories. As would be expected, the clear sky gives the best fit to the one-to-one line. The

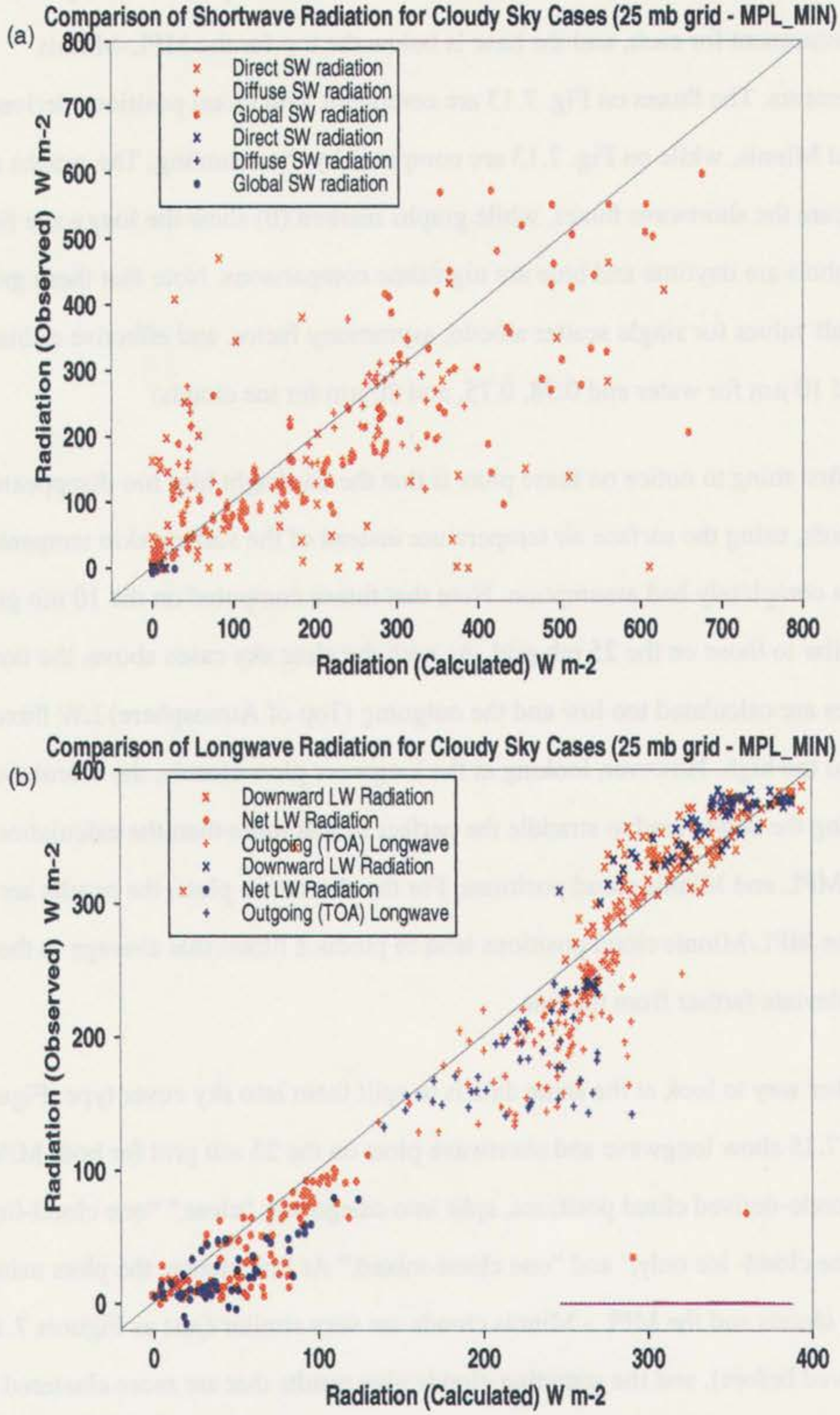

FIGURE 7.12: Cloudy Sky Cases with the 25 mb grid, where cloud-base and cloud-top are computed by the MPL and Minnis. a) Shortwave. b) Longwave.

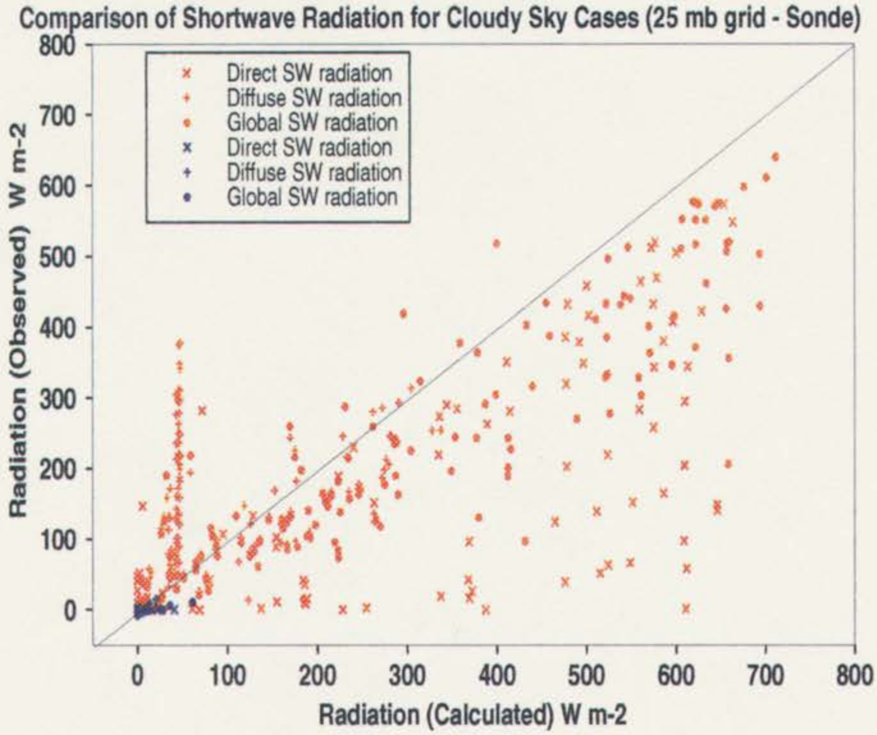

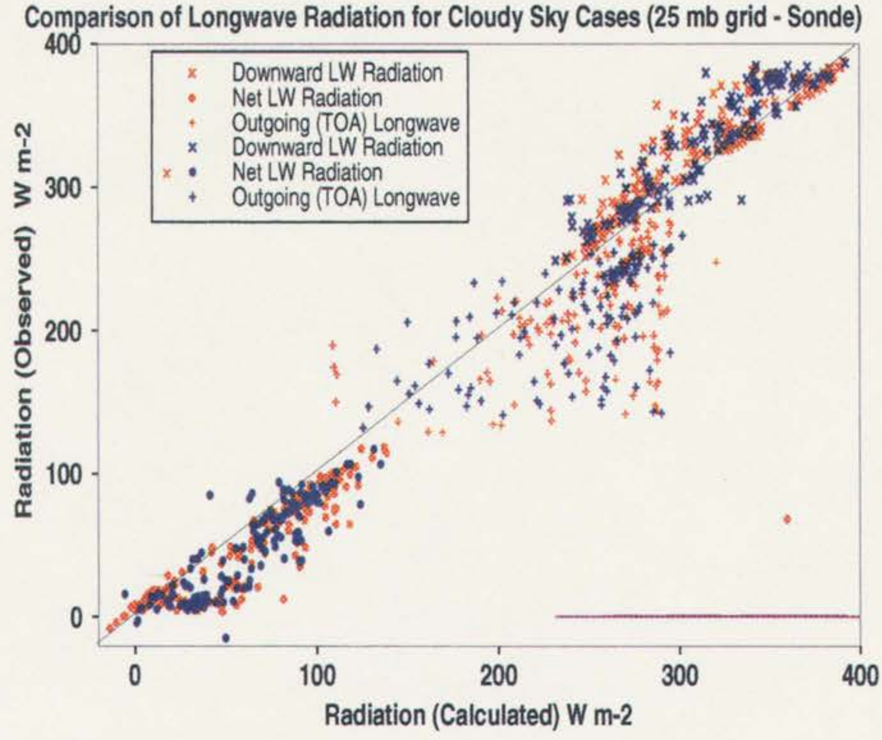

FIGURE 7.13: Cloudy Sky Cases with the 25 mb grid, where cloud-base and cloud-top are computed from the Sonde. a) Shortwave. b) Longwave.

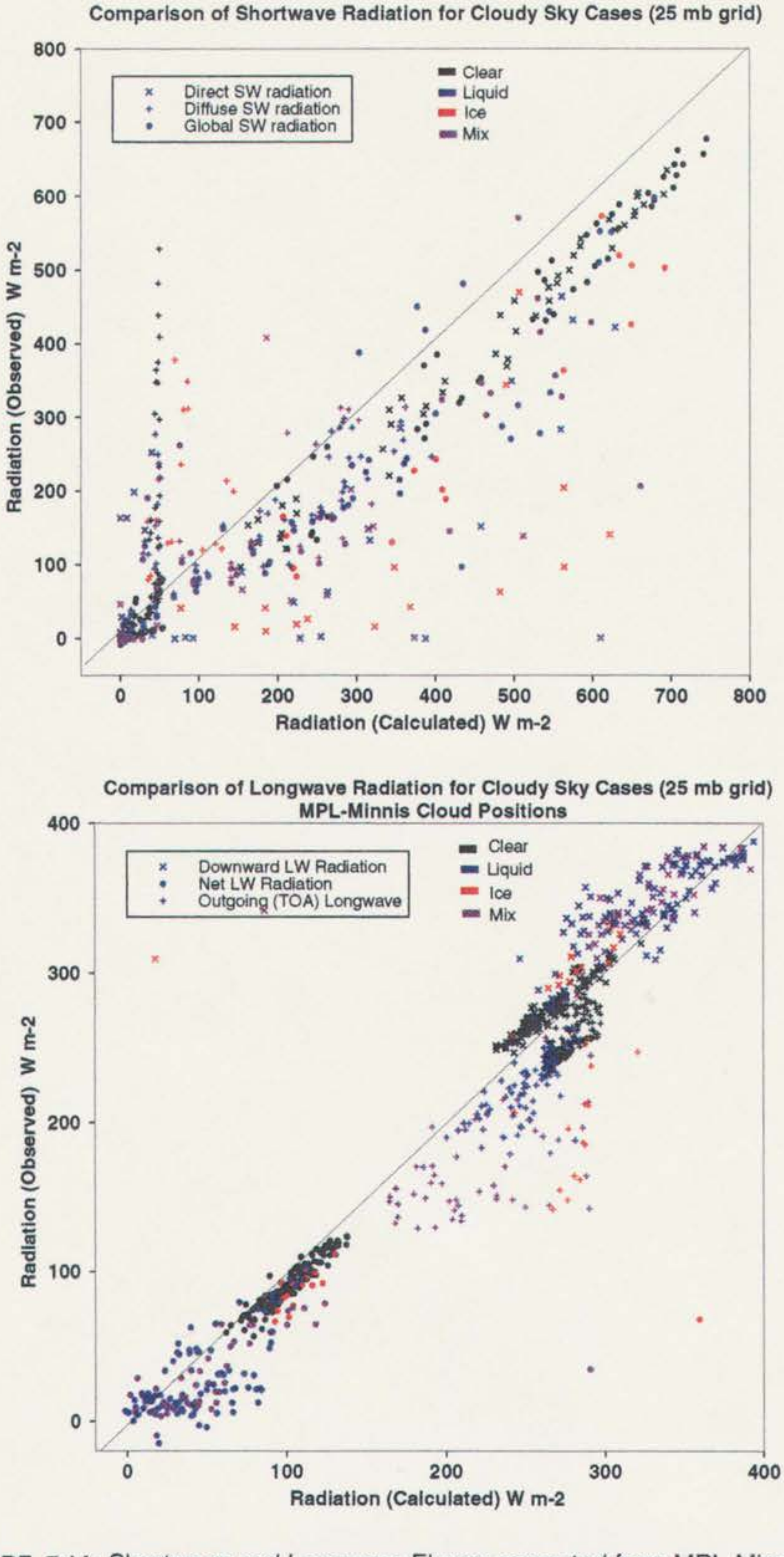

FIGURE 7.14: Shortwave and Longwave Fluxes computed from MPL-Minnis derived cloud positions.

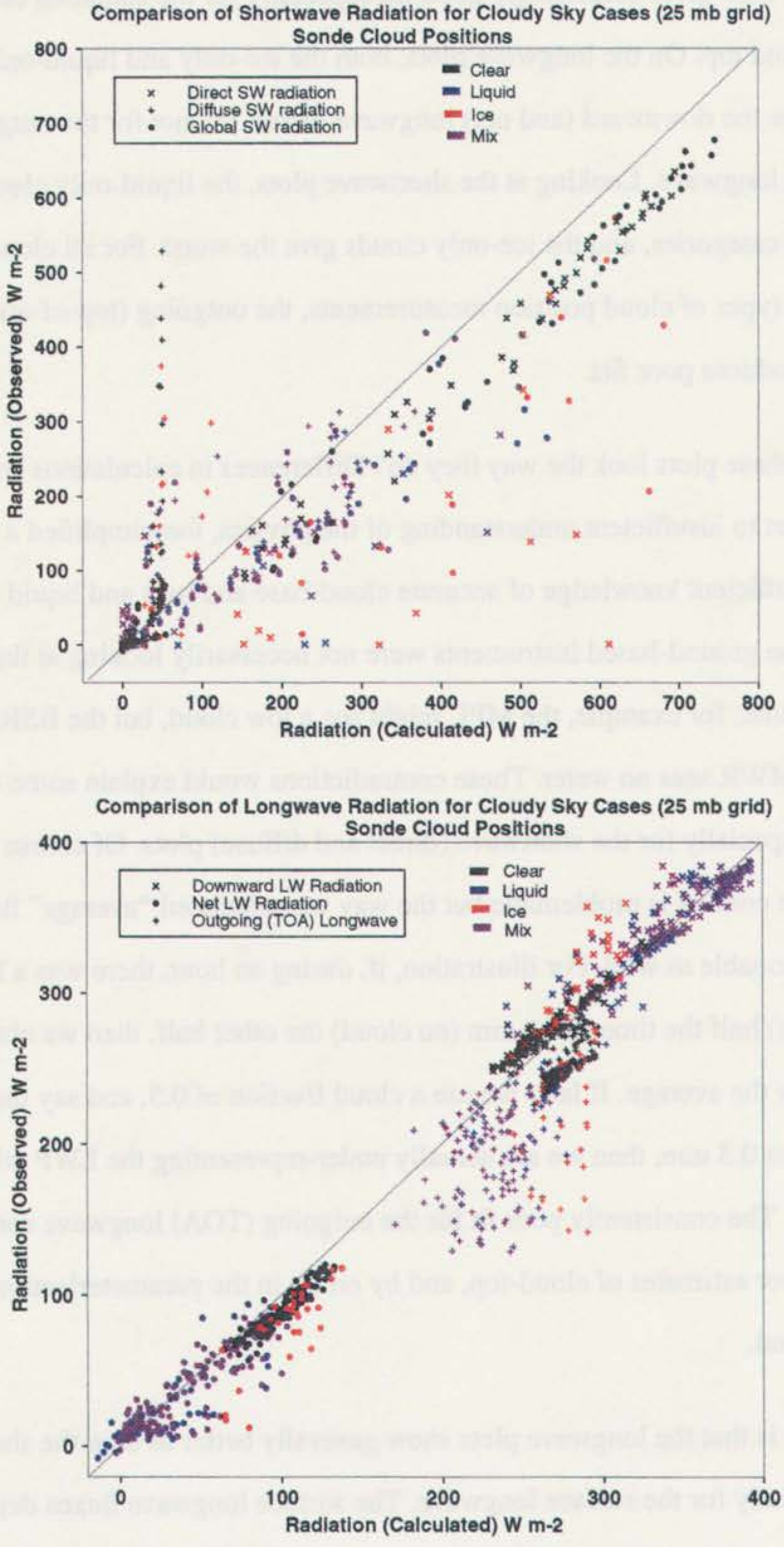

FIGURE 7.15: Shortwave and Longwave Fluxes computed from Sonde derived cloud positions.

mixed cloud case gives surprisingly good fit, especially for the sounding estimates of cloud-base and top. On the longwave plots, both the ice-only and liquid-only clouds give decent fits for the downward (and net) longwave fluxes, but not for the outgoing (top-of-atmosphere) longwave. Looking at the shortwave plots, the liquid-only clouds give the best fit in all categories, and the ice-only clouds give the worst. For all cloud categories and for both types of cloud position measurements, the outgoing (top-of-atmosphere) longwave produces poor fits.

Why do these plots look the way they do? Differences in calculations from observed are due in part to insufficient understanding of the physics, too-simplified a parameterization, and insufficient knowledge of accurate cloud-base and tops and liquid and ice contents. Also the ground-based instruments were not necessarily looking at the same place at the same time; for example, the MPL might see a low cloud, but the BSRN sees direct sun and the MWR sees no water. These contradictions would explain some of the outlying points, especially for the shortwave (direct and diffuse) plots. Of course the way we calculated ice content is problematic but the way we calculated "average" liquid water path is questionable as well. For illustration, if, during an hour, there was a LWP equal to 1 mm (clouds) half the time and 0 mm (no cloud) the other half, then we obtain a value of 0.5 mm for the average. If later we use a cloud fraction of 0.5, and say that the characteristic LWP is 0.5 mm, then we are actually under-representing the LWP when clouds were present. The consistently poor fit for the outgoing (TOA) longwave can be explained by poor estimates of cloud-top, and by errors in the parameterization, especially above the cloud.

Also note is that the longwave plots show generally better fit than the shortwave plots, specifically for the surface longwave. The surface longwave fluxes depend heavily on the location of cloud base, and lightly on the location of the cloud top. Because the surface downwelling longwave is only slightly biased toward too-low calculations, it would appear that the cloud-bases detected by the MPL are pretty accurate.

7.2.3 Multi-Level Clouds

Because Minnis reported, once per hour, cloud-tops at three vertical levels (low, middle and high) and at a fourth level corresponding to a composite of the other three, it would be useful to do an analogous computation with the MPL cloud-bases. However, the MPL reported a cloud-base every minute and inferring multiple cloud-bases during the hour is not straightforward. The gist of the algorithm to determine separate cloud-bases is as follows:

1) At the beginning of each hour, set "lobase", "midbase" and "hibase" to -30 (clear sky);

2) Read valid cloudbase from the MPL data set (cloudbase > 270 meters);

3) If "lobase" equals clear then set "lobase" equal to the new cloudbase;

4) Or else, if "lobase" already has a value, then compare new cloudbase to "lobase."

4a) If cloudbase differs from "lobase" by greater than 1000 meters, then either make "midbase" equal to cloudbase or set "midbase" to "lobase" and set "lobase" to cloudbase.

4b) If cloud differs from "lobase" by less than 1000 meters, then average this new cloudbase into "lobase" to get a new average "lobase."

5) Continue with step 2), and substitute "mid" or "hi" for "lo" as needed. For example, first compare the current cloud-base with "lobase." If step 4a) is true then compare the current cloud-base with "midbase," and read "if cloud-base differs from "midbase" by greater than 1000 meters..." Finally, if there are already three cloud-bases listed, then any cloud-base higher than "midbase" gets averaged into "hibase."

As an example, Table 7.8 shows the MPL multiple cloud-base calculations for No-

TABLE 7.8: Table of cloud-bases for November 9. Skycov is the whole hour cloud fraction

Time (UTC)	lobase (m)	lofrac (%)	mibase (m)	mifrac (%)	hibase (m)	hifrac (%)	skycov (%)
0	3850	1.00	-30	0.00	-30	0.00	1.00
1	3087	0.38	3716	0.62	-30	0.00	1.00
2	1620	0.13	3460	0.87	-30	0.00	1.00
3	1820	0.10	3760	0.50	4832	0.40	1.00
4	1170	0.23	3757	0.40	4984	0.35	0.98
5	792	0.45	3249	0.23	4375	0.32	1.00
6	911	0.67	1770	0.02	3111	0.31	1.00
7	302	0.47	3860	0.51	-30	0.00	0.98
8	456	0.35	1929	0.28	3270	0.32	0.95
9	1557	0.52	3113	0.38	4770	0.10	1.00
10	1770	0.47	5070	0.07	-30	0.00	0.53
11	763	0.70	9570	0.02	-30	0.00	0.72
12	870	0.28	4245	0.33	9854	0.32	0.93
13	9935	0.92	-30	0.00	-30	0.00	0.92
14	570	0.50	9870	0.03	-30	0.00	0.53
15	570	1.00	-30	0.00	-30	0.00	1.00
16	570	1.00	-30	0.00	-30	0.00	1.00
17	570	1.00	-30	0.00	-30	0.00	1.00
18	570	1.00	-30	0.00	-30	0.00	1.00
19	570	1.00	-30	0.00	-30	0.00	1.00
20	570	1.00	-30	0.00	-30	0.00	1.00
21	665	1.00	-30	0.00	-30	0.00	1.00
22	839	1.00	-30	0.00	-30	0.00	1.00
23	870	0.02	-30	0.00	-30	0.00	0.02
24	-30	0.00	-30	0.00	-30	0.00	0.00

vember 9. The titles, "lofrac," "mifrac," and "hifrac," correspond to the cloud fraction at each of the levels, while "skycov" represents the sum of the three. Remember that all cloudbases more than 1000 meters higher than "mibase" are averaged into "hibase."

Even though 1000 meters is probably too large a number, especially for low clouds (where 1000 meter difference is twice as high as the cloud itself), this multiple cloud level identifier is reasonable for most cases. Once we calculate multiple cloud-base levels, we should be able to compare with cloud-top levels.

Unfortunately, comparing cloud-bases and tops is not easy. Table 7.9 shows MPL cloud-base and fraction, and Minnis cloud-top and fraction for three occasions . The

TABLE 7.9: Three cases of multiple-level clouds, with different levels of spatial comprehension.

Date/Time		MPL Base (m)	MPL Frac (%)	Min Top (m)	Min Frac (%)
11 Nov - 17 UTC	1	570	0.92		
	2	7245	0.07	4540	0.94
	3			8810	0.06
	T		0.99		1.00
11 Nov - 19 UTC	1	570	0.10	550	0.07
	2	6965	0.32	5950	0.39
	3	8470	0.05	12360	0.02
	T		0.47		0.48
12 Nov - 20 UTC	1	1214	0.45		
	2	6707	0.40	4810	0.20
	3	8446	0.07	11540	0.70
	T		0.92		0.90

most comprehensible case is for 11 November at 17 UTC. At this time, two cloud layers were detected by each instrument, and the cloud fraction estimates imply that there are only two cloud levels. About 93% of the clouds during this hour stretched from 570 meters to 4540 meters, with 7% stretching from 7245 meters to 8810 meters. It turns out that the sounding supports these two cloud levels as well. Table 7.10 shows longwave flux values obtained from a one-level cloud (first row) and from the two-level cloud (second row). The one-level cloud illustrates how the parameterization would have treated multi-level clouds before we developed the algorithm to break the cloud into two layers.

For this date, the downward surface fluxes were improved, relative to observations, by a two-level cloud, while the top-of-atmosphere fluxes were made worse.

TABLE 7.10: Multi-level cloud from 11 November 17 UTC. The first row is one cloud spanning from 570 meters to 8810 meters, and the second row has the cloud split into two separate entities. The solar optical depths are the same for each case. "Rad" stands for the modeled value, "obs" stands for the observed value.

base 1 (m)	top 1 (m)	frac 1 (%)	base 2 (m)	top 2 (m)	frac 2 (%)	Opt Depth	down LW rad ($W m^{-2}$)	down LW obs ($W m^{-2}$)	TOA LW rad ($W m^{-2}$)	TOA LW obs ($W m^{-2}$)
570	8810	0.99	-30	0	0.00	4.11	297.8	280.4	225.0	233.3
570	4540	0.92	7245	8810	0.07	4.11	279.1	280.4	258.0	233.3

This November 11, 17 UTC case is one of a very few that can be considered for inputting into the parameterization. The hour including 12 November 20 UTC has cloud-bases and cloud-tops that support each other, and total cloud fraction that is consistent, but the individual cloud layers are confusing. The 1214 meter base is probably obscuring higher cloud-bases, and the 11540 meter cloud-top is obscuring some cloud-tops. We might interpret this as is that the 1214 cloud-base extends to 4810 meters, and both the 6707 meter and the 8446 meter bases extend to near 11540 meters. The hour of 11 November, 19 UTC is useless for cloud-base / cloud-top comparisons. Probably the 570 meter base and 550 meter top belong together (due to the similar cloud fraction) but because the base is higher than the top, there is no way of knowing which of these is wrong. The same problem is true in the middle layer, again where the base is higher than the top, but the fractions seem to agree.

7.3 Heating Profiles of the Atmosphere

Because clouds affect the radiative balance of the atmosphere, it is logical to ask how clouds heat or cool the atmosphere. The radiation parameterization can be used to calculate heating profiles, with separate components for longwave and shortwave. Figures 7.16 through 7.22 show heating profiles for a variety of different conditions during the IOP. For each plot, the red lines represent shortwave heating, the blue lines are longwave heating, and the black lines represent the total (LW + SW) heating. For each color, dotted lines represent clear sky while solid lines represent the cloudy-sky calculations. Obviously, for clear sky cases, the dotted lines and solid lines are the same (Fig. 7.16), and there

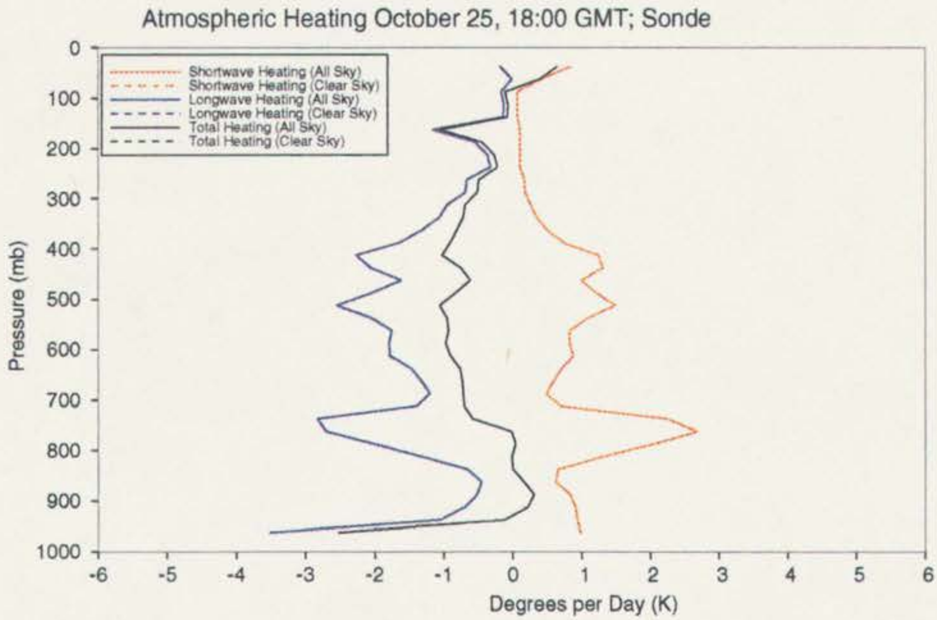

FIGURE 7.16: Heating Profile for a Clear Sky late morning case. Black lines are the net heating (LW + SW), Solid lines are all-sky cases.

is no shortwave flux at night (Fig. 7.17).

Kinks are seen in the clear-sky profile (Fig. 7.16) and can be related to temperature and humidity. The enhanced LW cooling and enhanced SW warming at 750 mb are due to being in a relatively high RH region. In essence, there is a "cloud" near 750 mb, even though it is not visible to the MPL or Minnis. The region around 675 mb has less LW cooling and less SW warming because it is a relatively dry region. The kink around 175 mb is again due to a relatively wet region.

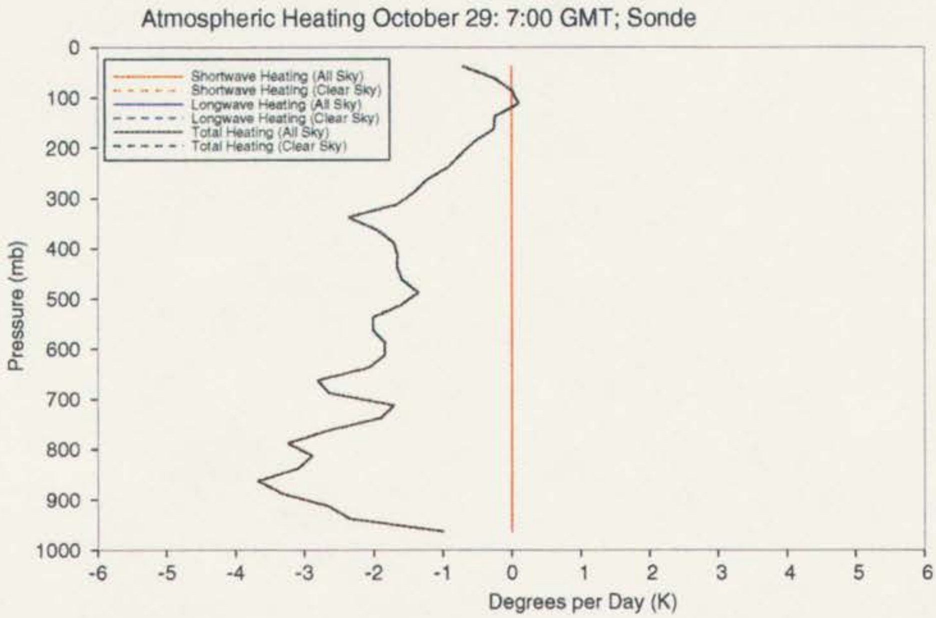

FIGURE 7.17: Heating Profile for a Clear Sky night-time case. Black lines are the net heating (LW + SW), Solid lines are all-sky cases.

Three examples of cloud heating profiles are shown in Figures 7.18 through 7.20: a high cloud, a low cloud, and a thick cloud. Without clouds, the atmosphere generally cools by about one degree per day in longwave, and warms by up to one degree per day by shortwave in midafternoon. This combination creates a near zero net heating. For cloudy skies, the results are more complicated. The low cloud drastically reduces the shortwave warming and the longwave cooling below the cloud, increases the shortwave warming and longwave cooling within and just above the cloud, and causes little or no effect far above the cloud. High clouds cause much less of a total change (about 0.1 degree/day below created by offsetting longwave and shortwave tendencies), but drastically change the heating profile near the cloud. A thick cloud acts to drastically change the heating structure below it, producing much less atmospheric cooling (by over 1 degree/day) than would occur in the clear-sky case.

An interesting exercise is to calculate the heating profile change when the clouds are

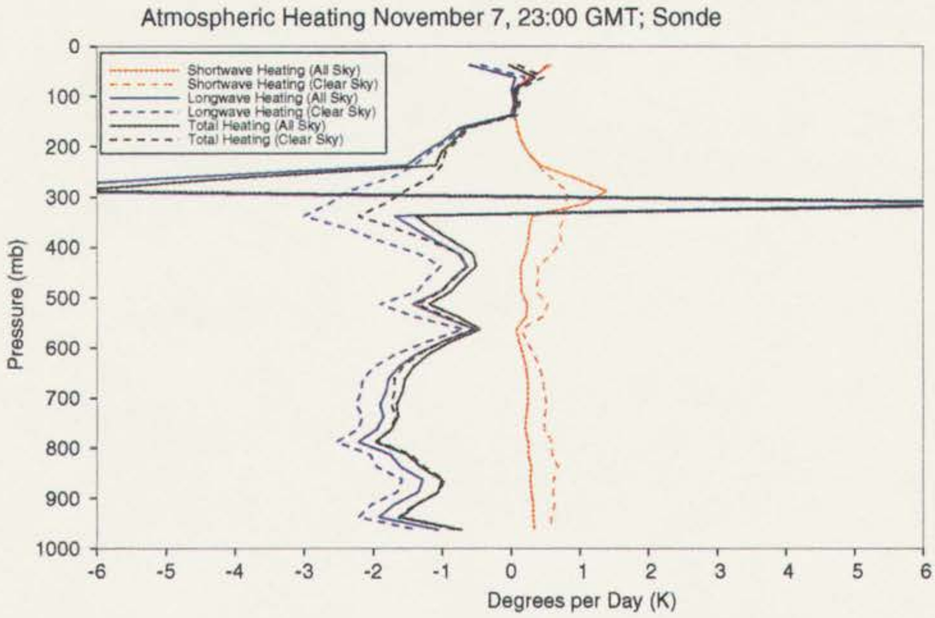

FIGURE 7.18: Heating Profile for a single high level cloud in afternoon. Black lines are the net heating (LW + SW), Solid lines are all-sky cases. Note profiles for cloudy sky in relation to clear sky.

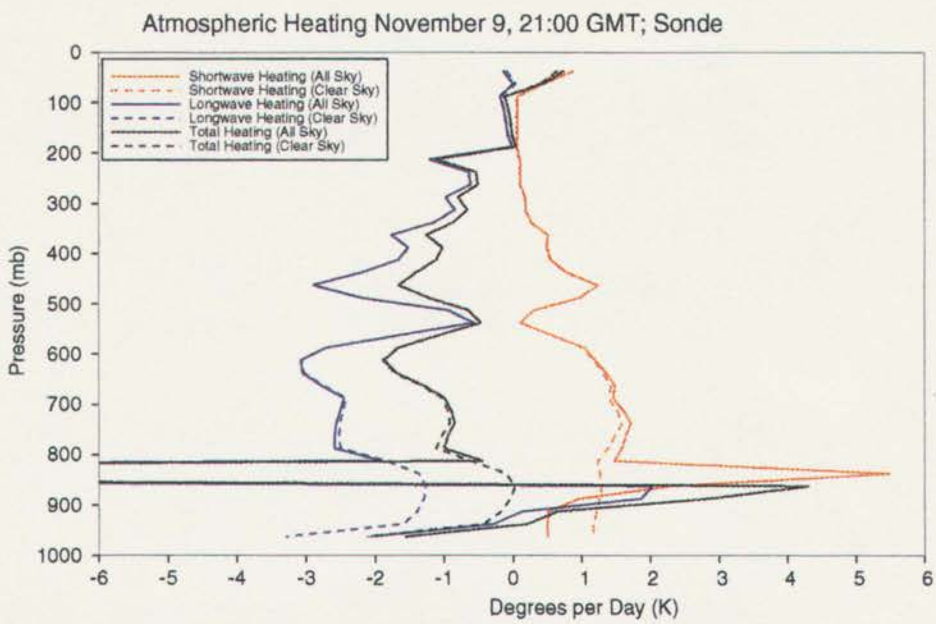

FIGURE 7.19: Heating Profile for a single low-level cloud in afternoon. Black lines are the net heating (LW + SW), Solid lines are all-sky cases. Note profiles for cloudy sky in relation to clear sky.

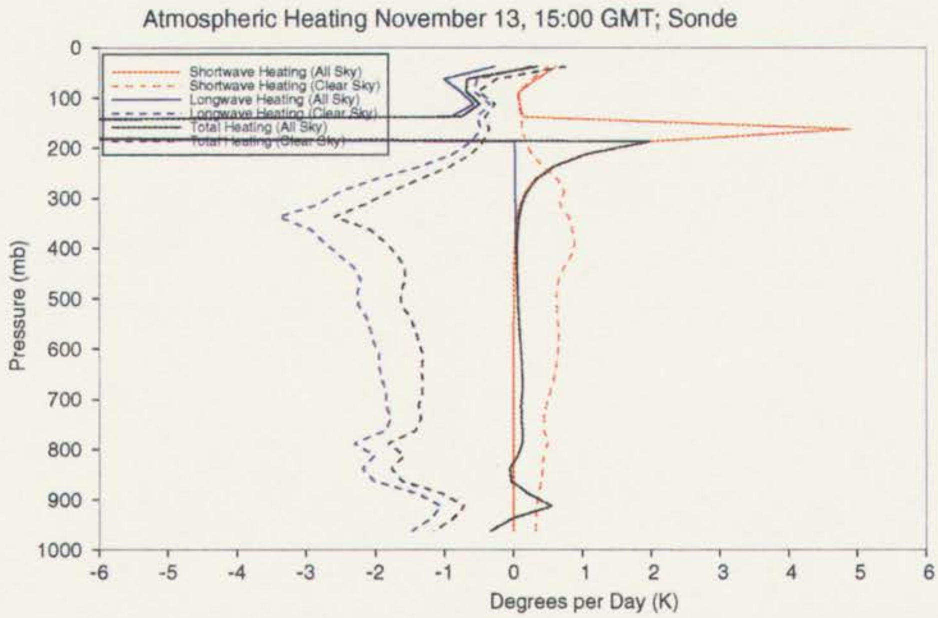

FIGURE 7.20: Heating Profile for a thick vertically extensive cloud in morning. Black lines are the net heating (LW + SW), Solid lines are all-sky cases. Note profiles for cloudy sky in relation to clear sky.

changed from single-level to multi-level (as in the case of November 11, 17 UTC discussed above). Figures 7.21 and 7.22 show these heating profiles. Note that for the single layer cloud, water is assumed for levels up to about 437 mb (greater than 253 K), while ice is assumed for levels above that. For the two-layer cloud, water is assumed in the lower cloud, while ice is assumed for the upper cloud.

The clear-sky kinks can be explained by layers of higher or lower relative humidity relative to other layers, and are the same for both plots. However, the interesting differences are due to changing from one cloud to two clouds. For the single cloud calculation (Fig. 7.21) the cloud fraction was set at 92% for the whole cloud, and the liquid/ice interface was located at 253 K. There are large heating/cooling discontinuities, especially right above the interface. Apparently, the drastic warming right above the 253 K interface, arises because of the assumptions made to identify liquid and ice.

For the double-layer clouds (Fig. 7.22), the lower liquid cloud has a cloud fraction of

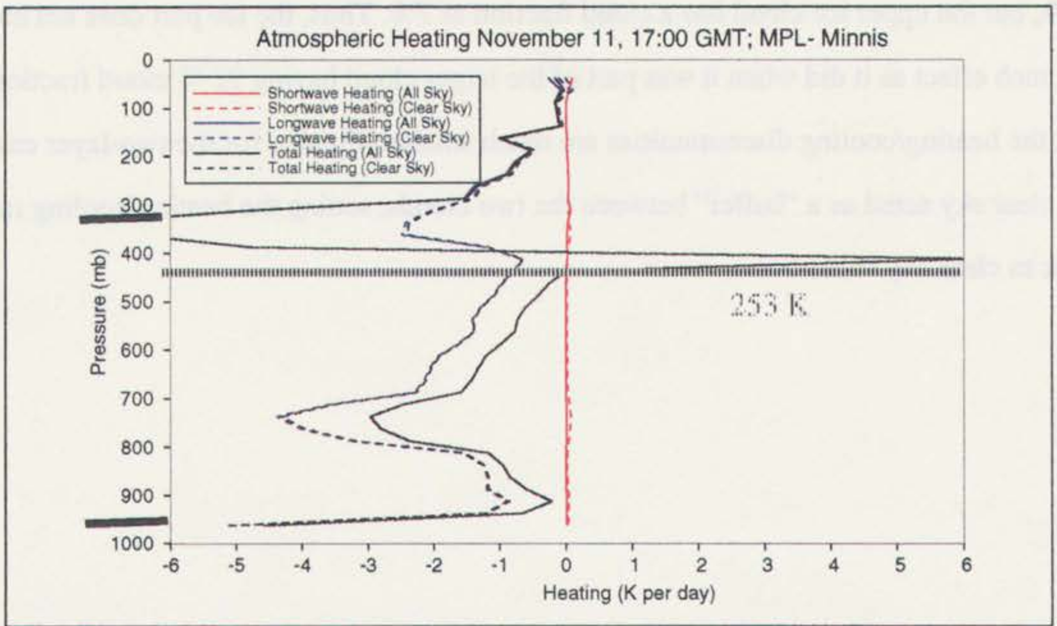

FIGURE 7.21: Heating Profile for a vertically extensive cloud in morning. Black lines are the net heating (LW + SW), Solid lines are all-sky cases. Note profiles for cloudy sky in relation to clear sky. Liquid - Ice interface is about 437.5 mb. The cloud has a base of 962.5 mb, is liquid-only to 437.5 mb, then is ice-only from there to 312.5 mb.

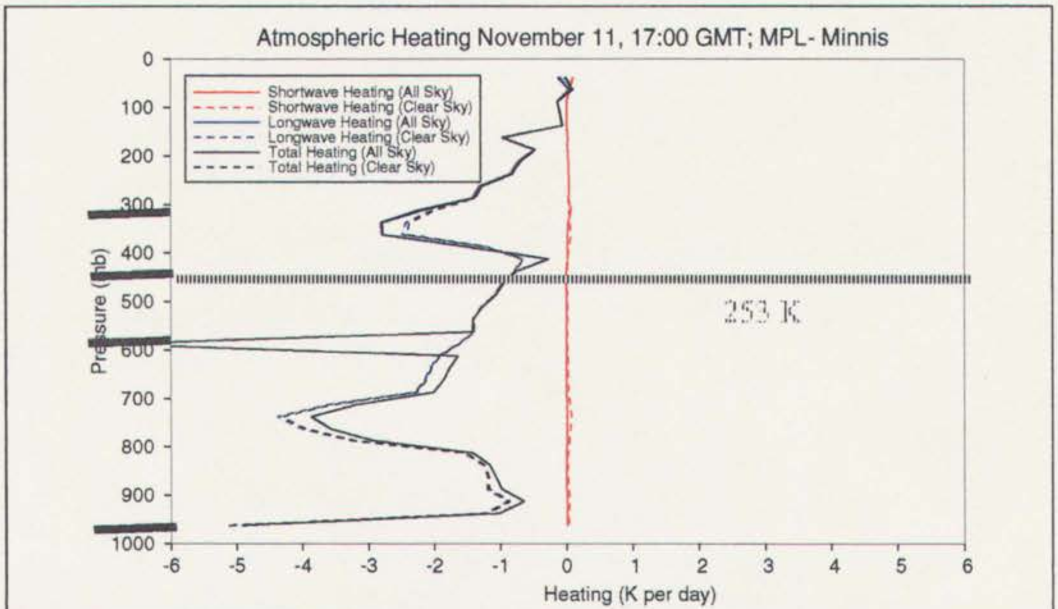

FIGURE 7.22: Heating Profile for a two-layer cloud in morning. This is the same time period as for the previous figure. Black lines are the net heating (LW + SW), Solid lines are all-sky cases. The lower cloud is liquid-only with a base at 962.5 mb and a top at 587.5 mb. The upper cloud is ice-only with a base at 437.5 mb and a top at 312.5 mb. Note profiles for cloudy sky in relation to clear sky.

92%, but the upper ice cloud has a cloud fraction of 7%. Thus, the ice part does not have as much effect as it did when it was part of the larger cloud having 92 % cloud fraction, and the heating/cooling discontinuities are much smaller. Finally, for the two-layer case, the clear sky acted as a "buffer" between the two clouds, setting the heating/cooling rates back to clear sky values.

CHAPTER 8

Summary and Conclusions

8.1 Summary of Data Analysis

210 megabytes of SGP-CART Central Facility ARM observations, from the October/ November 1994 IOP, have been analyzed to give, as much as possible, a comprehensive picture of the vertical meteorology and radiation fluxes for each hour of the IOP. Each dataset was individually analyzed, by calculating statistics and averaging or interpolating to one hour intervals. Then data from different datasets were compared. The MPL and the BLC both computed cloud base, but because the MPL could measure higher altitude clouds, the MPL dataset was used for further analyses. The BSRN and SIROS were both systems of radiometers; but because the SIROS data-set had substantial bad or missing data, the BSRN surface fluxes were used. It turned out that "temporal" cloud fraction (calculated from MPL data) and "spatial" cloud fraction (calculated by Minnis) were highly correlated and showed a definite diurnal variation. Comparing the SIROS and SMOS measurements of skin temperature showed that the SIROS temperature is a better estimate of "skin" temperature; but due to the large amount of missing data, the SMOS data proved better to input into the radiation parameterization.

Even though for most of the IOP, a clear visual picture of the cloud, water, and radiation properties could be produced, there were was some bad or missing data. Following are some problems with the data and how they were solved or skirted:

1) *Bad or missing data, especially from the SIROS, the satellite-derived cloud products (Minnis) and upper atmosphere profiles from the soundings:* Scratched the SIROS data and the missing Minnis data, and tried to insert reasonable values for upper level temperature and vapor profiles.

2) *Inconsistent time intervals of observations.* Interpolated or averaged to one hour intervals

3) *No vertical profiles of ozone or ice.* Assumed characteristic climatological values and profiles of each.

4) *No observations of optical parameters such as single scatter albedo, asymmetry parameter, and effective radius.* Assumed characteristic values.

5) *No differentiation of cloud to whether it was ice or water.* Assumed ice for temperatures below 253 K, and water above 253 K.

6) *Substantial time periods when the MPL registered a cloud base above Minnis' cloud top.* Scratched all of these cases. However, valid cloud bases and tops for a these periods still might be calculated from the soundings.

7) *Time intervals when the MWR registered above-legal values of liquid water path.* Scratched these cases, unless Jim Liljigren gave revised values.

8) *Intervals when both the MPL and Minnis recorded multiple cloud levels* (for example, 3 tops and 3 bases during an hour and no telling which bases and tops correspond to each other). Complicated cases were scratched, but there were a few cases where multiple cloud bases and tops could be matched i.e, when the differentiation was small or only slightly varying.

8.2 Summary of parameterization results

Even with all the missing data and manipulation of the data, the parameterization was run successfully for the whole IOP, and some of the resulting calculations appeared to compare well to observations. Sensitivity tests to cloud-base, cloud-top, and optical parameters were run for a few IOP periods.

8.2.1 Clear Sky

Clear sky (as determined from the MPL data) cases showed the best fit to observations, with almost all calculations (direct, diffuse and global shortwave, downward, net and outgoing longwave) within 10-20% of the perfect fit line. Global (total) solar fluxes were consistently calculated higher than observed, due to the simplified atmosphere (only three gases, no aerosols, and no high levels) and the simplified mathematics. The longwave parameterization consistently over-estimated the outgoing longwave (relative to observations) and under-estimated the downward longwave (and thus over-estimated the net longwave). These discrepancies could be related to the discrepancies in the shortwave (from least to most likely), including faulty observations by one or more of the instruments, setting the model top at 37.5 (or 45) millibars to ignore upper atmosphere (stratosphere, mesosphere, etc.) effects, under-estimating the water vapor or ozone amounts and radiative effects in the upper troposphere, or over-simplifying the radiative effects throughout the whole atmosphere.

8.2.2 Cloudy Sky

Interpretation of the cloudy sky results was much less straightforward, especially due to the lack of ice and water information in the cloud and the inaccuracies of the cloud-base and top estimations. Some assumptions included ice/water differentiation at 253 K, linear distributions of water and ice, and default parameters of cloud optical properties.

8.2.2.1 One-layer clouds

Modeled whole-sky shortwave albedo compared well to the Minnis whole-sky shortwave albedo. Under liquid cloud conditions, the albedo calculations were fairly good (correlated well with observations and produced a near one-to-one regression line), but for ice-only conditions the parameterization performed poorly. The similarity of the correlations and regression lines, of the liquid-only to the mixed-phase clouds shows that the liquid water regions have a more powerful effect on albedo.

The longwave parameterization produced fluxes similar to observations on average, but like the clear sky cases, the parameterization consistently over-estimated the outgoing longwave (relative to observations) and under-estimated the downward longwave (and thus over-estimated the net longwave). There was improvement if the sonde's estimates of cloud top and cloud base were used instead of the MPL-Minnis estimates. Possible explanations for these problems include all the ones for the clear-sky calculations, plus poor estimates (too low) for the cloud tops, insufficient knowledge of the ice content and the distributions of both water and ice content, and the use of "default" optical properties to describe all clouds. Because the cloud-base levels were the most trustworthy ARM dataset, the downward longwave fluxes produced the best fit.

The shortwave parameterization did not fare nearly as well, producing deviations from the observed fluxes nearly equal in magnitude to the observed fluxes themselves. The best fit was to the total shortwave, which was good because the total solar radiation is what heats the surface and atmosphere and therefore more important. Again, there was little noticeable improvement when the model was changed to a finer grid, but some improvement was noticed when the cloud base and cloud top were estimated by the lidars instead of the soundings. However, because there are fewer valid cloud-base/cloud-top estimates from the lidars than from the soundings, this improvement might be illusory.

Radiative fluxes are extremely sensitive to the cloud optical parameters (asymmetry parameter, single scatter albedo, and effective radius of the cloud particles). While the default values of cloud optical parameters usually produced reasonable fluxes, for many cases these default values were not adequate for describing the observed radiative fluxes. Because clouds form at various levels, temperature, pressure, and by various processes, it is reasonable to expect that default values would not do a very good job for individual cases.

8.2.2.2 Multi-level clouds

As expected, multi-level clouds proved to be very difficult to identify and to input into the radiation parameterization. Because Pat Minnis' satellite retrievals grouped cloud-tops into "bins," the MPL cloud-bases were grouped into bins as well. Without knowledge of which cloud base corresponded to which cloud top and how to distribute a liquid water column through multiple clouds, simplifying assumptions were made about the cloud positions and the water content. For a few cases, this method worked very well.

8.2.3 Heating Profiles

Heating profiles were calculated for different cases (such as clear, single-level liquid-only, and multi-level clouds). Clear skies produced longwave cooling about 1°C for the depth of the atmosphere, but individual layers were warmer or cooler depending on the relative maxima of relative humidity or temperatures in the layers. High clouds produced a little less net (longwave + shortwave) cooling in the lower atmosphere over clear sky, while low clouds caused net warming just below themselves and larger cooling just above them. Overall, clouds have a tendency to decrease both the longwave cooling and the shortwave heating in the atmosphere below them, increase both the longwave cooling and the shortwave heating within the cloud, and cause little or no affect well above the cloud. Obviously, because there is no shortwave at night, the cloud has no effect on night-time SW heating. Whether the cloud produces a net change in the heating of the whole atmosphere, compared to the clear sky, depends on the level and nature (optical depth) of the cloud in question.

The magnitude of heating profile changes, when dividing a single cloud layer into two cloud layers, were surprisingly large. The cloud system as a whole (especially the ice/water interface) produced strong heating discontinuities when the cloud was one layer, but produced smaller (and probably more realistic) heating discontinuities when the cloud was split. Unfortunately, without actual observations of heating profiles, it is hard to say that one or the other is the "truth."

8.3 Conclusions

The combination of analyses of the ARM data and tests of the radiation parameterization, produced a reasonably comprehensible picture of the atmospheric flux profile during the IOP, and appeared to simulate some of the cloud and radiation interactions. This comprehensive picture is probably the only one of its kind, especially the visual correlation of the Composite Plots. Some of the parameterized cloud cases, especially those of ice clouds, produced poor results when compared to observations, but others, such as liquid clouds and clear sky cases, produced much better simulations. While many of the poor results are due to model limitations, more consistent data retrievals, and specific added retrievals (such as cloud ice, or presence of multiple clouds) likely would have produced better simulations.

There are many paths for future study, using ARM data and radiation parameterizations. A different radiation parameterization could be used; one that can handle specific cloud-bases and cloud-tops, distribution of ice and water, distribution of optical parameters and more realistic atmospheric constituents and radiative properties. Another future work would use data from a different IOP; one with more consistent data and measurements of variables such as ice content, cloud particle size and ozone profiles. Instruments such as cloud radar and airplane-based lidars would improve the cloud-base and top estimates and clearly detect multiple cloud levels.

Appendices

A NetCDF

NetCDF (written by Unidata, and sponsored by the National Science Foundation) is an interface designed to be *self-describing* (the file includes *meta-data*, data about the data) and *network-transparent* (accessible by all operating systems). The NetCDF implements an *abstract data type*, meaning that all operations to access and manipulate data in a NetCDF file must only use a set of functions provided in a library. Thus the user writes his/her own interface to access these functions and thus data can be stored or manipulated without affecting these library programs.

A NetCDF file has *dimensions, variables and attributes*, which together, these components capture the meaning and relation of the data in the data-set. A *dimension* is a named integer used to specify the shape of a variable in the dataset. The dimension can represent a physical dimension such as time, latitude, longitude, or level, or could index more abstract properties such as view, or spectral channel. Some NetCDF files have one dimension and others have more. For examples, the dimension "ntime" would represent the number of observations in time for a variable in the NetCDF file, and the dimension "longitude" would describe the number of longitude values that a parameter is being measured (longitude = 3 means 3 different longitudes) A *variable* is a named multidimensional array of values of a certain type (integer, real, character, etc.). For example, temperature(longitude, latitude, ntime) is an arrary of temperature having dimensions of longitude, latitude and time. An *attribute* is meant to contain information about a netCDF variable or about the global (entire) NetCDF file. For example, a variable attribute might state a variable's units, length, or valid maximum and minimums, while a global attribute might describe the contents of the file or a description of the instrument.

:

The NetCDF interface supports direct access to single data values, direct access to hyperslabs of data (a hyperslab is a piece of the multi-dimensioned variable that is specified by giving the corner points of the array), and record-oriented data for a single variable (treating the complete hyperslab as a single entity). Each dimension, variable and attribute in a NetCDF file has an *ID* stored along with it. Therefore, instead of data being manipulated by a NetCDF routine, the data's integer ID's are being manipulated. To read a NetCDF file, a sequence of calls to the NetCDF library might be look like this (along with the corresponding names of the subroutines):

TABLE A.1: Sequence of calls to manipulate a NetCDF file

Task	Subroutine Used
Open existing NetCDF file	NCOPN
Find out what is in the file	NCINQ
Get the DIMENSION names and sizes	NCDINQ
Get the VARIABLE names, types and shapes	NCVINQ
Get ATTRIBUTE names	NCANAM
Get ATTRIBUTE values	NCAINQ
Get VARIABLE values	NCVGT
Close NetCDF file	NCCLOS

Each of these calls is made from a main program, specific to the data set, which the user writes. The specifics of each subroutine can be found in the NetCDF user's manual, which can be found on-line or in published form.

A helpful utility is NCDUMP, where from a terminal window, a user can display the contents of a file, to have an idea what kind of data is in it, before he or she writes the program to manipulate the data in the file.

Unfortunately, my experience with NetCDF was not as straightforward as it should have been, because a few of the NetCDF library subroutines did not compile on the NeXTSTEP's version of FORTRAN. In other words, NetCDF is not completely "network-transparent." I noticed the problem accessing hyperslabs of variables in data-sets that had different values of "ntime". For example, one Microwave Radiometer data-set had 287 water vapor values in the file, and another had 288. Normally, the subroutine NCDINQ (get the dimension name and size) would handle this task, but this subroutine would not compile. Unfortunately, all future subroutines (those to get the variable data) needed to know the dimension size, therefore retrieving needed data was impossible. In essence then, I had to "fool" future NetCDF routines into believing that NCDINQ already returned the correct values. Therefore, I wrote a generic shell script to NCDUMP a series of data-sets (say, all the Microwave Radiometer), to manipulate each data set with terminal-line commands, and to write the filename, file date, and value of ntime to a separate file. Thus my main program could read this separate file and send the proper information to each of the NetCDF subroutines.

B Interpolation of BBSS soundings

Further use of the soundings involved interpolation to uniform grids as well as interpolation to fit missing data. Because clouds are regions of saturated (100% Relative Humidity) air, I decided regions of high relative humidity in the vertical path of the balloon could be interpreted as cloudy layers. Therefore, so that regions of high relative humidity could be easily graphed (i.e. humidity as a 2-Dimensional plot - time and level) I needed to interpolate the balloon soundings to a uniform vertical grid, and uniform horizontal time. I also needed uniform sounding data in order to plug into the radiation parameterization. The result were interpolations to every hour (from the three hour sounding intervals) in time, and 25 meter (to compare with cloud base height measurements) and 25 and 10 millibar interpolations (to fit into the radiation model) in the vertical. Following

:

are some steps I used for these interpolations.

B.1 To a uniform grid (25 mb, 10 mb, or 25 meters)

Because I had already used the hypsometric equation to calculate height, I could use basically the same procedure to interpolate to 25 and 10 millibars and to 25 meters. First, I set up whole IOP arrays of sounding variables (pressure, temperature, dewpoint, relative humidity, and height) with dimensions of day, hour and level. These arrays would hold the values of the corresponding variable for each day of the sounding (22 total - October 24 to November 14), each hour of the day (25 total - from 0 UTCto 24 UTC), and each level of the atmosphere(39 levels for the pressure grid - 37.5 mb to 987.5 mb, 500 levels for the height grid - 0 m to 12,500 m). Then, I set up arrays for individual soundings, that had only the one dimension of datapoint, i.e., each entry row of a sounding data set (like Table 9 above) corresponded to a datapoint. Therefore, because I knew the pressure (or height) of each sounding datapoint, I could easily match each sounding variable into its proper place in the whole IOP sounding pressure-grid arrays (or the height-grid arrays). Finally, I set up arrays of surface temperature and pressure, the values for each day of the IOP and each hour of the day.

Specifically, here is a list of the steps I used in a FORTRAN program to calculate soundings to uniform whole IOP pressure-grid (and height-grid) arrays.

1) Declare 3-Dimensional arrays named (in FORTRAN):

variable_gridded(numdays, 0:numhours, numlevels),

where **variable_gridded(day, hour, level)** stands for the values of pressure, temperature, relative humidity, height or dewpoint (p,t,rh,z or td) at one of the grid points. **Numdays** = 22 (the number of days in the IOP), **numhours** = 24 (number of hours in a day, with 24 yesterday equal to 0 today), and **numlevels** is the number of levels in the grid (=

39 for the 25 mb grid, =500 for the 25 m grid).

For example, **t_gridded(17, 18, 30)** is the temperature on day 17 (November 9), hour 18, and level 30 (762.5 mb for the 25 mb grid, 725 meters for the 25meter grid).

Notes: The pressure grid counts 25 mb intervals from 37.5 mb (level 1) to 962.5 mb (level 38) with the surface pressure corresponding to level 39. The height grid counts 25 meter intervals from 0 meters (level 1) to 12500 meters (level 500).

2) Declare layer-averaged variables named

variable_avg,

which is average of two levels. For example, **t_avg** might be the average between the temperatures at level 29 and 30.

3) Declare 2-dimensional arrays named

variable_surf(numdays, 0:numhours)

where **variable_surf(day, hour)** represents surface temperature or pressure for a particular sounding.

For Example: **t_surf(17, 18)** is the surface temperature on day 17, hour 18.

4) Declare 1-dimensional arrays named

variable_data(numdatapoints)

where **variable_data(datapoint)** holds the values for pressure, height, temperature, relative humidity or dewpoint for each row of the particular sounding's data file. Most soundings have about 2500 datapoints.

For example, **p_data(100), t_data(100),** and **z_data(100)** for the November 9 18Z sounding represent the pressure, temperature and height values from the first row of Table 9 above.

5) Read one sounding data file at a time, fill in the arrays for **variable_data(-datapoint)**, and the values for **t_surf(day, hour)**, and **p_surf(day, hour)**.

6) Set the initial **datapoint** to **numdatapoints** to interpolate the pressure grid

(Set the initial **datapoint** to 0 for the height grid.)

7) Set initial level to **p_gridded(day, hour, level=0)** for the pressure grid.

(Set initial level to **z_gridded (day, hour, level=0)** for the height grid.)

8) Begin counting **datapoint** down (counting **datapoint** up) until...

p_data(datapoint) < p_gridded(day, hour, level) for pressure,

(z_data(datapoint) > z_gridded(day, hour, level) for height,)

9) Average the values for **variable_data(datapoint)** and **variable_data(-datapoint+1)**

(Average the values for **variable_data(datapoint)** and **variable_data(datapoint-1)**)

to get the values for **variable_gridded(day, hour, level)**.

10) Repeat steps 8) and 9) with **level = level + 1**, until **level = numlevels**.

B.2 To a uniform 1 hour grid, and to fill in missing values.

Once I had the soundings interpolated to uniform grids, interpolation between soundings and filling in missing data was much easier. Because the other data sets had time intervals of one hour or smaller, I thought it useful to interpolate the soundings to one hour intervals, rather than three hours. Basically, if legitimate data existed at a certain level for two subsequent three-hourly soundings, then a simple weighting function could be used to fill in the hourly soundings. For example, if **variable_gridded(day, hour, level)** and

variable_gridded(day, hour+3, level) both exist, then

variable_gridded(day, hour+1, level) =

2/3 *(**variable_gridded(day, hour, level)**) + 1/3 *(**variable_gridded(day, hour+3, level)**)

and

variable_gridded(day, hour+2, level) =

1/3 *(**variable_gridded(day, hour, level)**) + 2/3 *(**variable_gridded(day, hour+3, level)**)

Because **variable_gridded(day-1, 24, level) = variable_gridded(day, 0, level)**, calculations for the hours between 21Z and 03Z were simple as well.

If data was missing for either of the original three hour soundings, then decent data was inserted before making the hourly soundings. A similar algorithm to the hourly interpolation was used to fill in the missing data. For example, if the data for **variable_gridded(day, hour, level)** was missing, then it would be filled in with

variable_gridded(day, hour, level) =

3/6*(**variable_gridded(day, hour-3, level)**) + 3/6*(**variable_gridded(day, hour+3, level)**).

If either of these values didn't exist, then I would try

variable_gridded(day, hour, level) =

3/9*(**variable_gridded(day, hour-6, level)**) + 6/9 *(**variable_gridded(day, hour+3, level)**

:

or

variable_gridded(day, hour, level) =

6/9 *(**variable_gridded(day, hour-3, level)**) + 3/9 *(**variable_gridded(day, hour+6, level)**)

and further and further intervals, until I found existing data points. If I couldn't find existing data within a twelve hour interval, I set **variable_gridded(day, hour, level)** equal to -999.

C Composite Plots

The following are the time series for the whole IOP of cloud position, MWR water data and BSRN radiation fluxes.

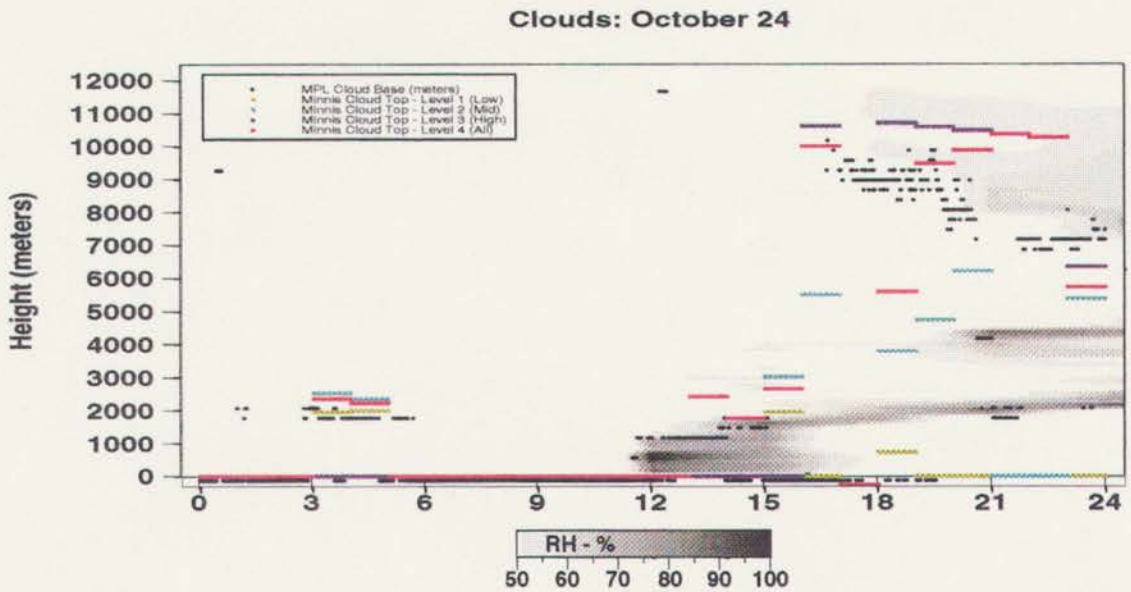
Clouds: October 24
MPL Cloud Base (meters)
Minnis Cloud Top - Level 1 (Low)
Minnis Cloud Top - Level 2 (Mid)
Minnis Cloud Top - Level 3 (High)
Minnis Cloud Top - Level 4 (All)
Height (meters)
RH - %
50 60 70 80 90 100

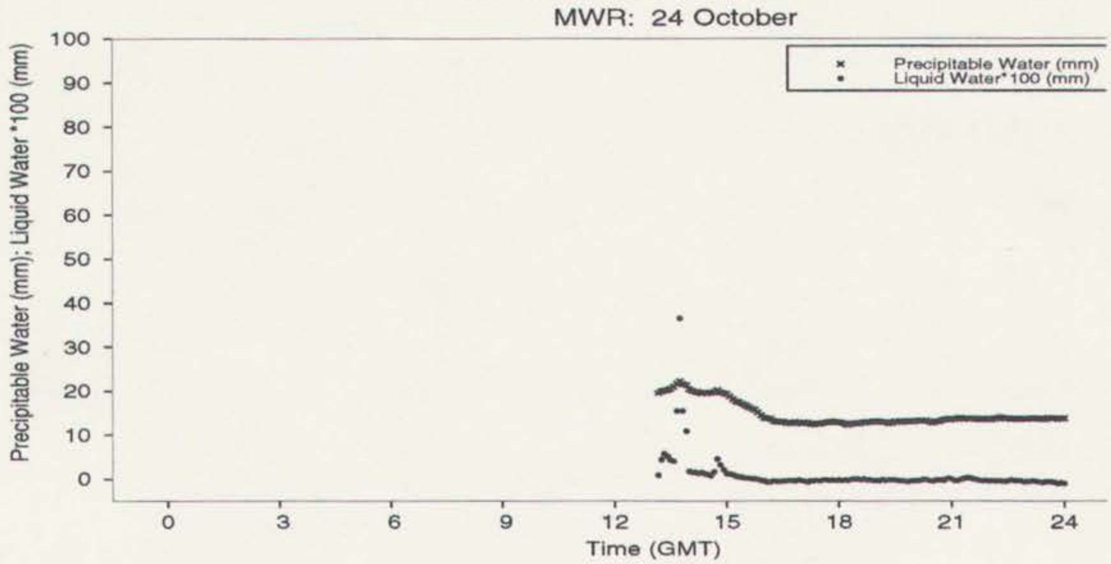
MWR: 24 October
Precipitable Water (mm)
Liquid Water*100 (mm)
Precipitable Water (mm); Liquid Water *100 (mm)
Time (GMT)

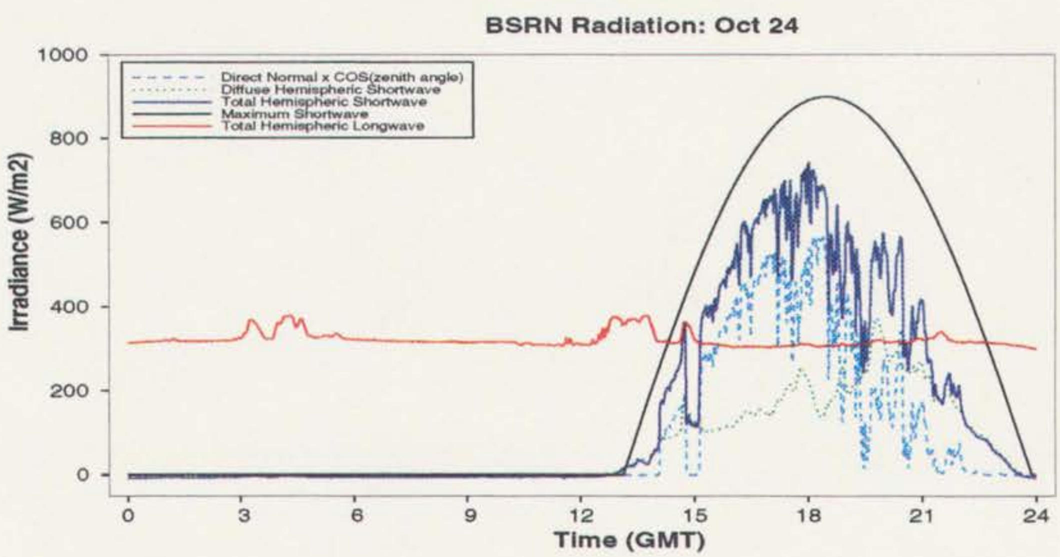
BSRN Radiation: Oct 24
Direct Normal x COS(zenith angle)
Diffuse Hemispheric Shortwave
Total Hemispheric Shortwave
Maximum Shortwave
Total Hemispheric Longwave
Irradiance (W/m2)
Time (GMT)

Clouds: October 25

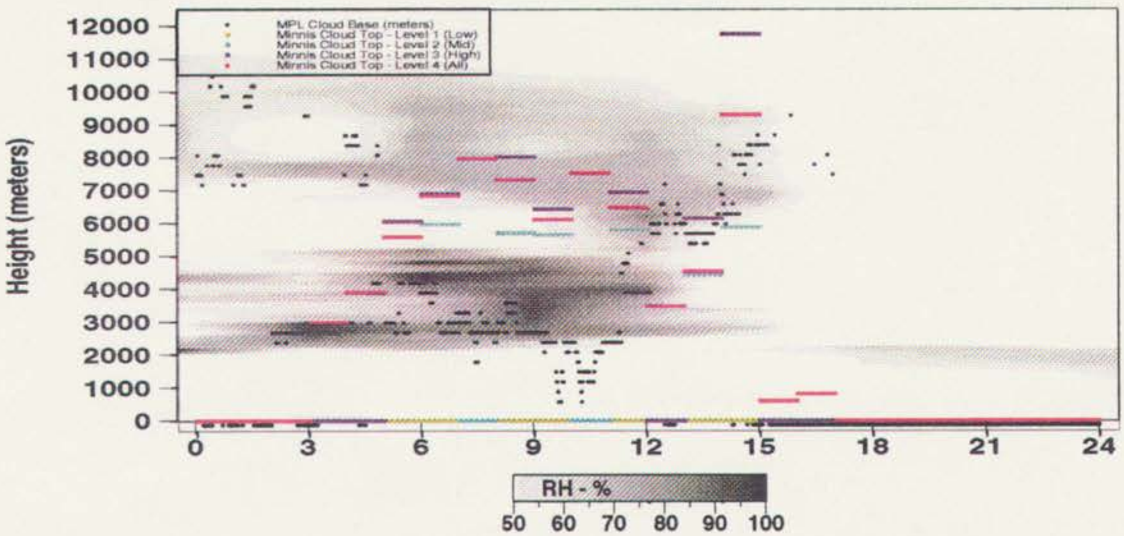

MWR: 25 october

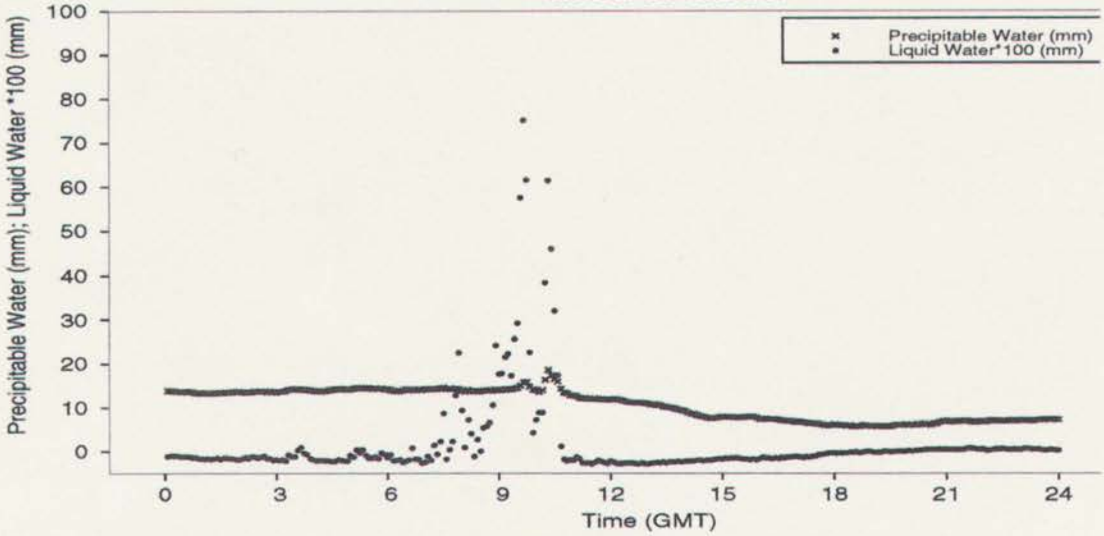

BSRN Radiation: Oct 25

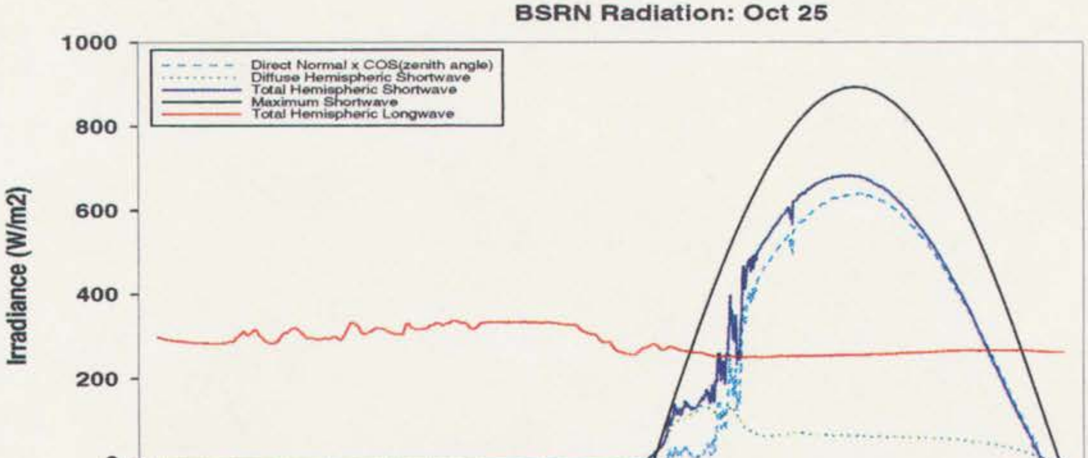

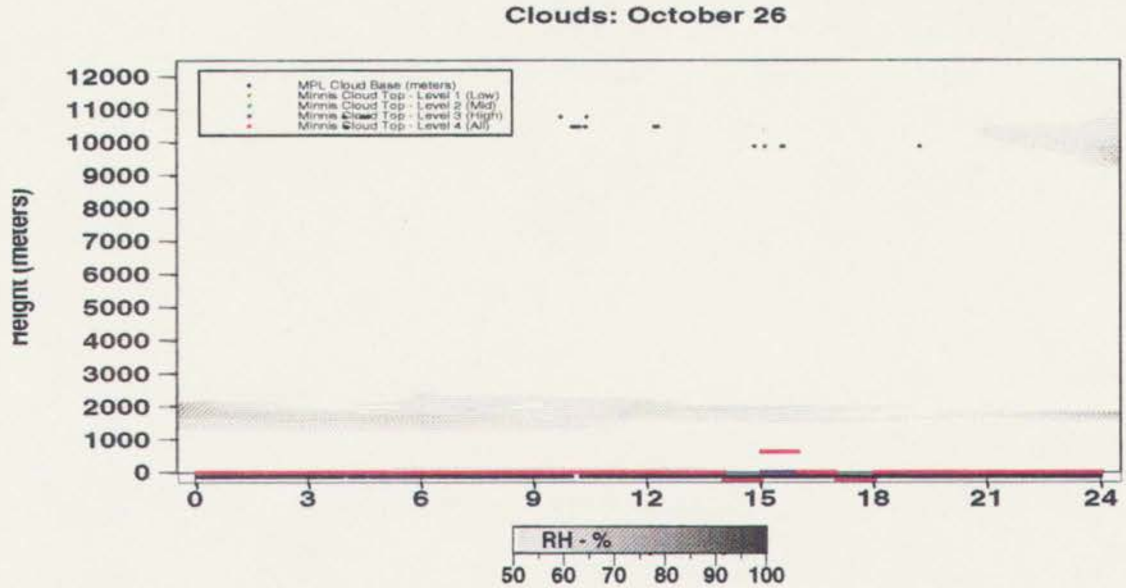
Clouds: October 26
MPL Cloud Base (meters)
Minnis Cloud Top - Level 1 (Low)
Minnis Cloud Top - Level 2 (Mid)
Minnis Cloud Top - Level 3 (High)
Minnis Cloud Top - Level 4 (All)
Height (meters)
RH - %
50 60 70 80 90 100

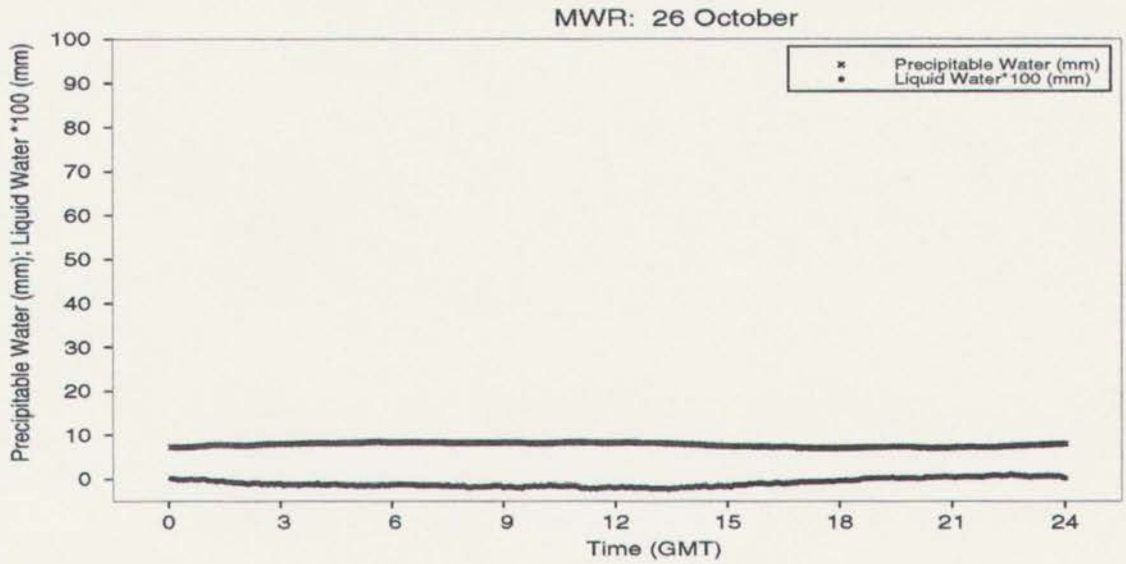
MWR: 26 October
Precipitable Water (mm)
Liquid Water*100 (mm)
Precipitable Water (mm); Liquid Water *100 (mm)
Time (GMT)

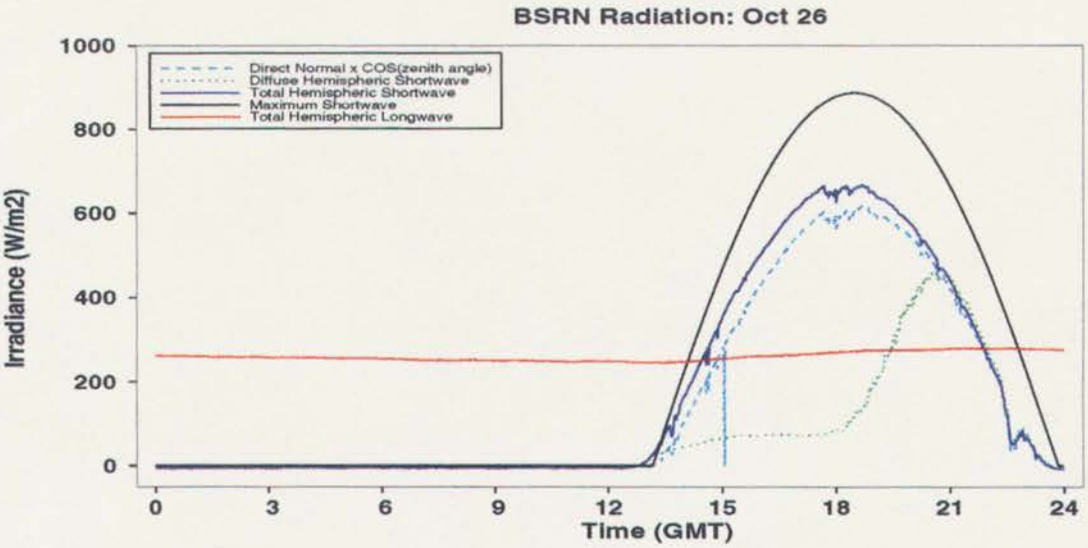
BSRN Radiation: Oct 26
Direct Normal x COS(zenith angle)
Diffuse Hemispheric Shortwave
Total Hemispheric Shortwave
Maximum Shortwave
Total Hemispheric Longwave
Irradiance (W/m2)
Time (GMT)

Clouds: October 27

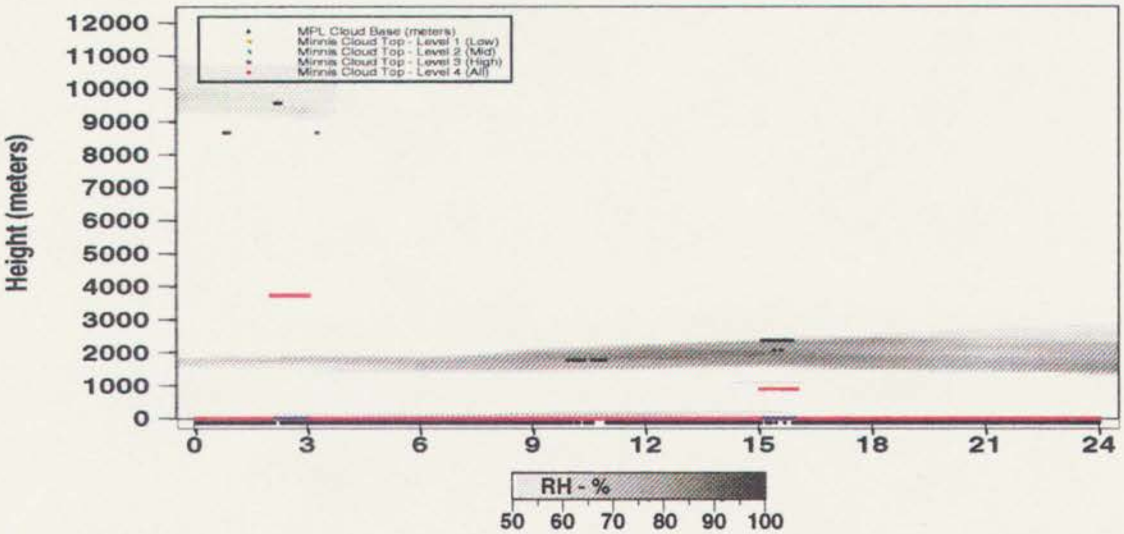

MWR: 27 October

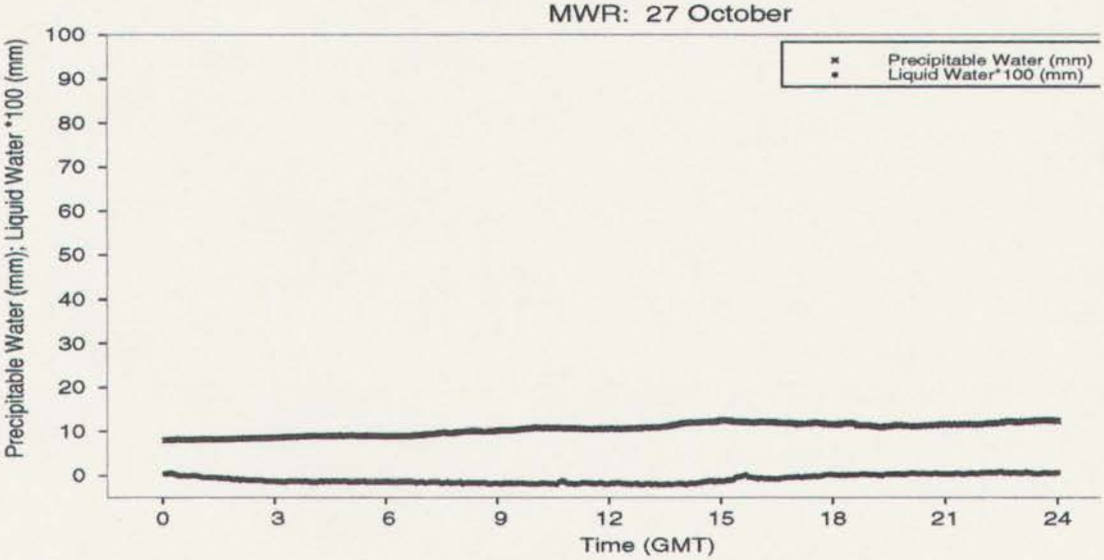

BSRN Radiation: Oct 27

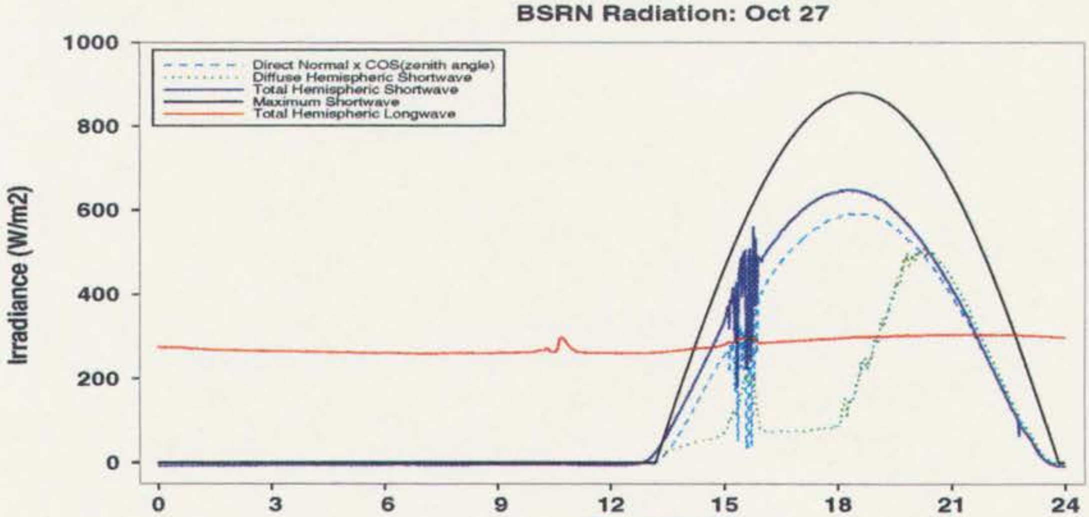

Clouds: October 28

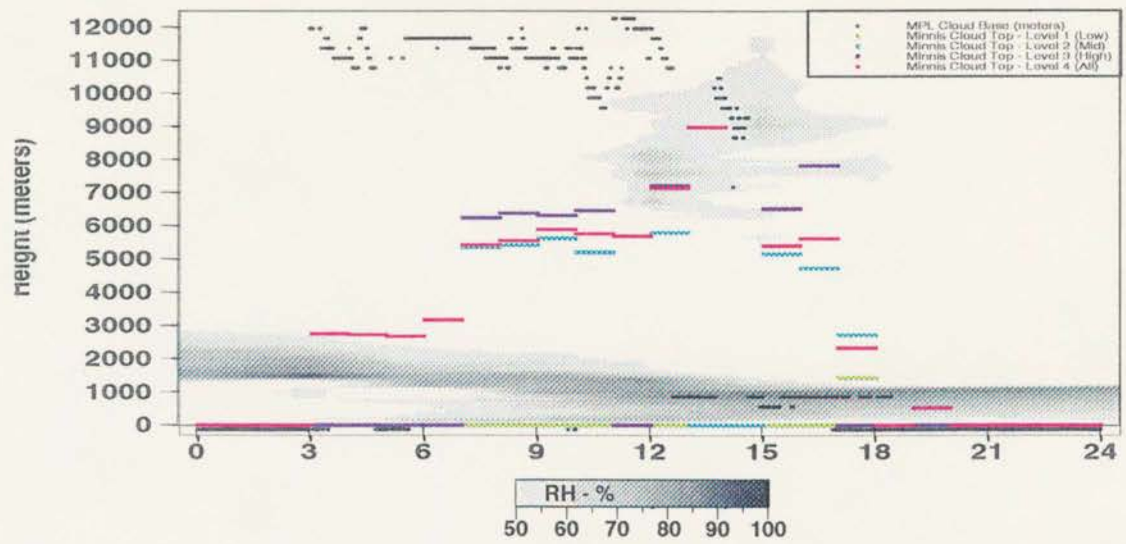

MWR: 28 October

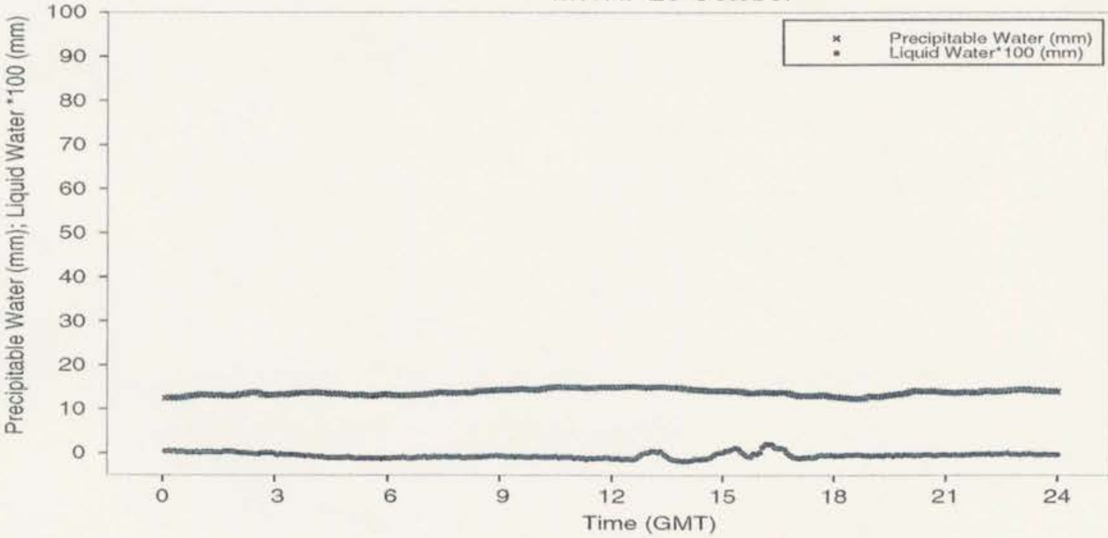

BSRN Radiation: Oct 28

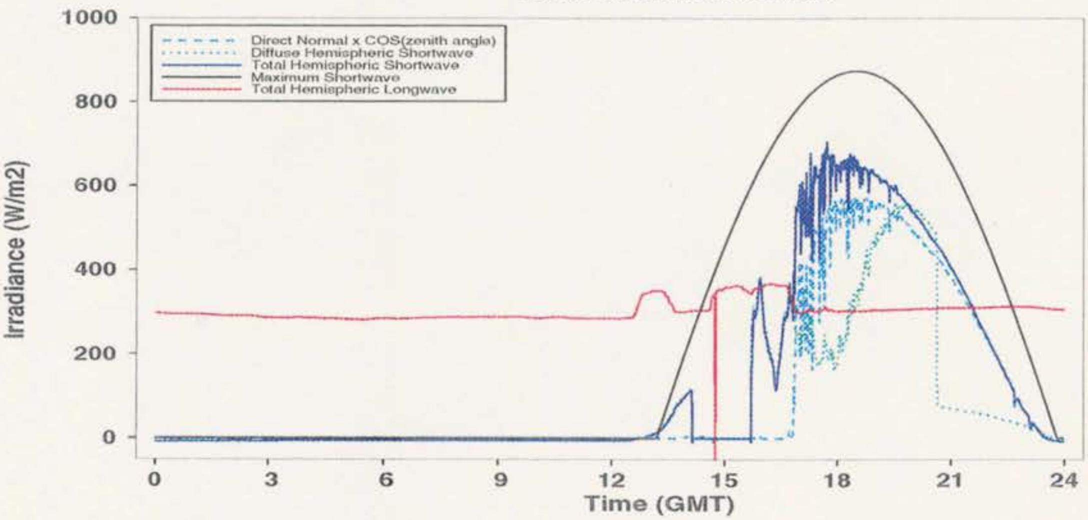

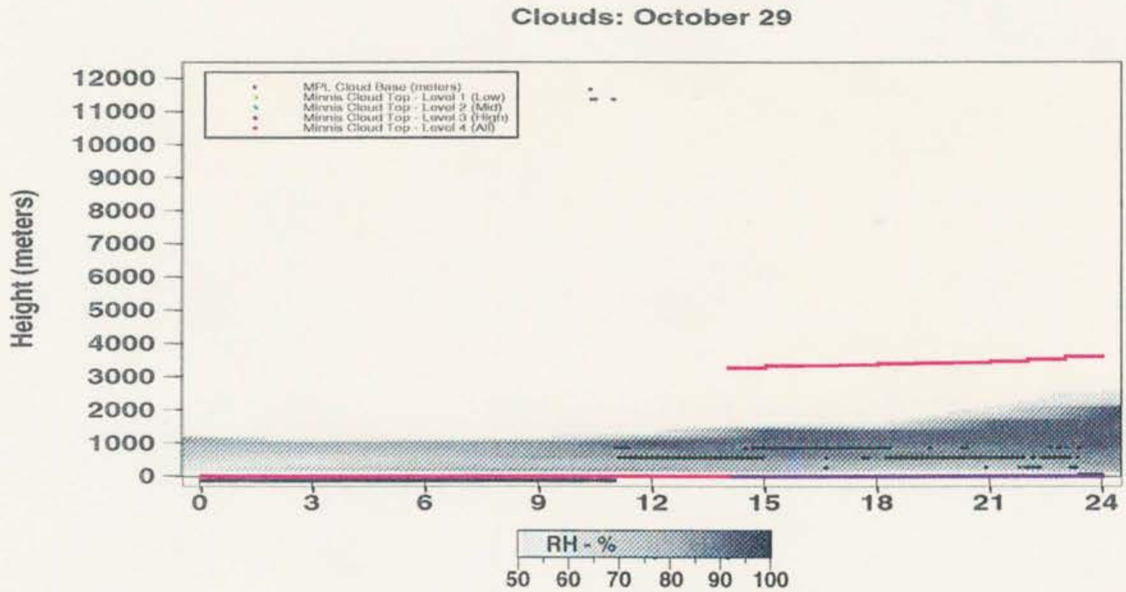
Clouds: October 29
Height (meters)
MPL Cloud Base (meters)
Minnis Cloud Top - Level 1 (Low)
Minnis Cloud Top - Level 2 (Mid)
Minnis Cloud Top - Level 3 (High)
Minnis Cloud Top - Level 4 (All)
RH - %
50 60 70 80 90 100

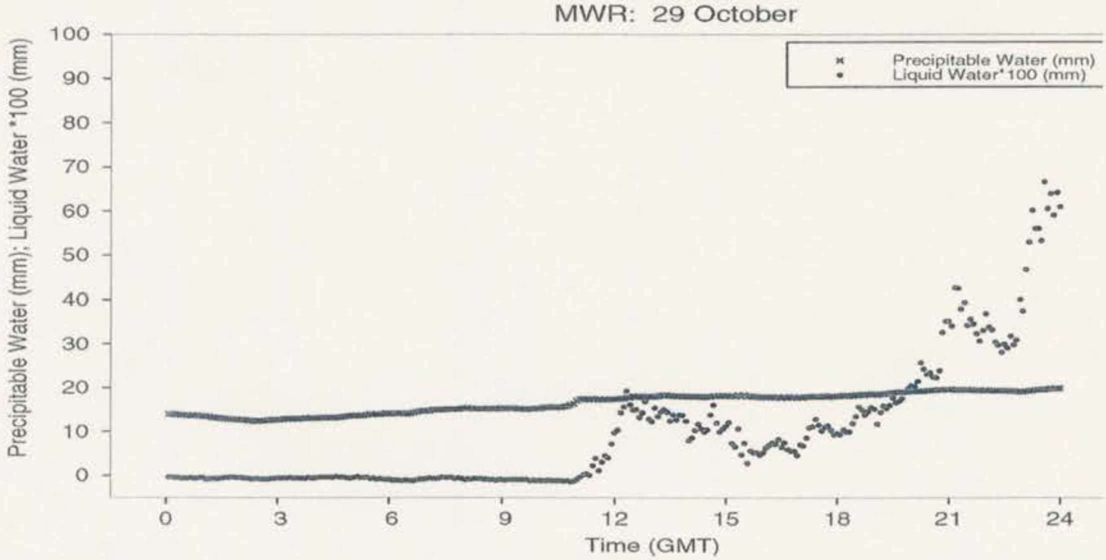
MWR: 29 October
Precipitable Water (mm); Liquid Water *100 (mm)
Precipitable Water (mm)
Liquid Water*100 (mm)
Time (GMT)

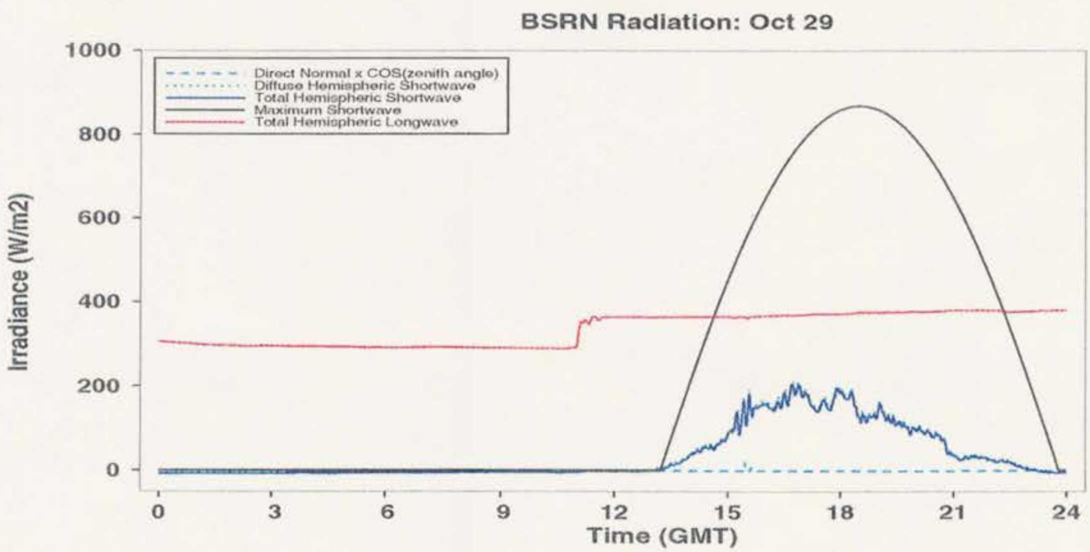
BSRN Radiation: Oct 29
Irradiance (W/m2)
Direct Normal x COS(zenith angle)
Diffuse Hemispheric Shortwave
Total Hemispheric Shortwave
Maximum Shortwave
Total Hemispheric Longwave
Time (GMT)

Clouds: October 30

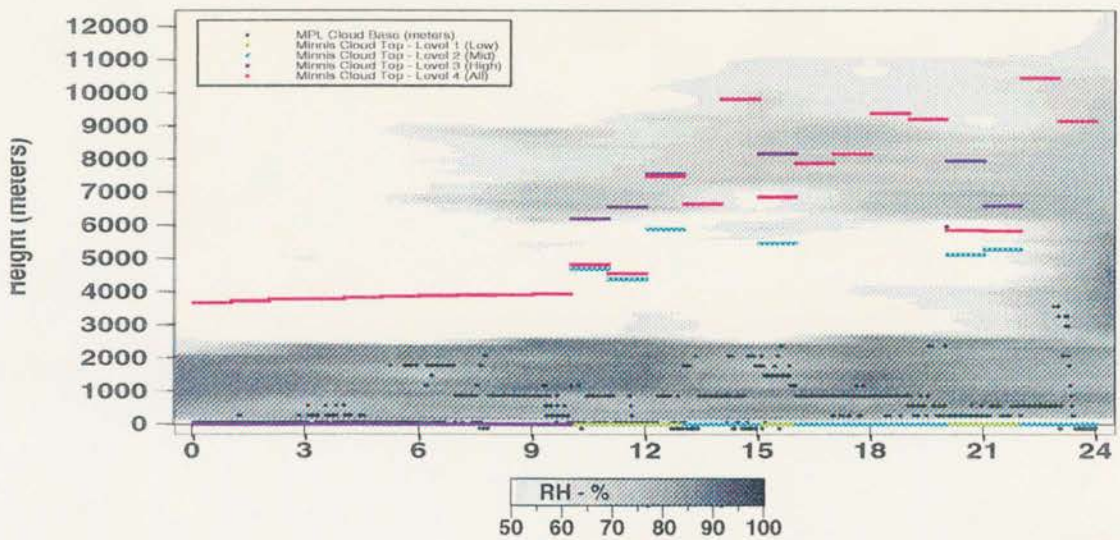

MWR: 30 October

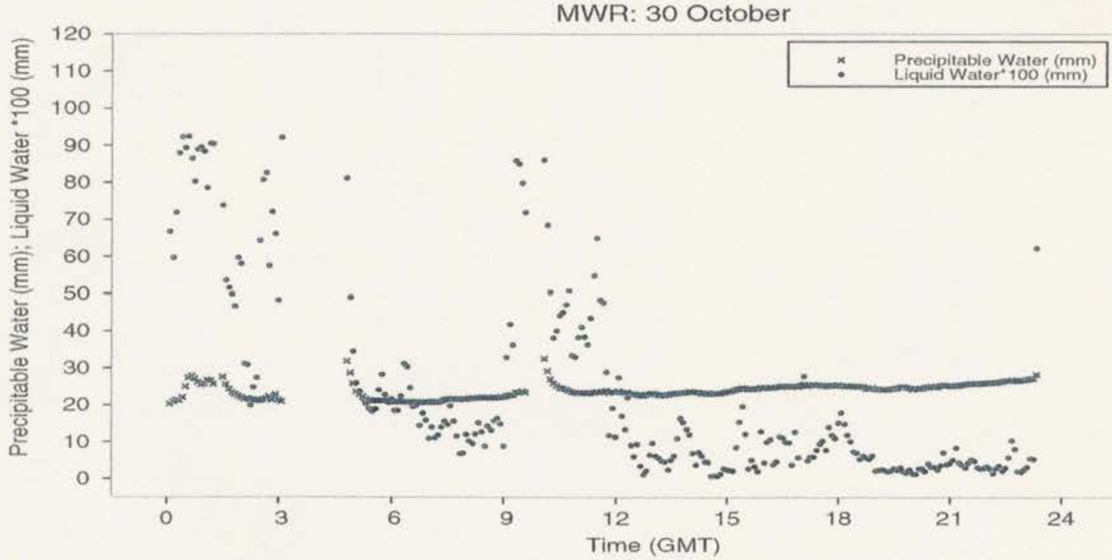

BSRN Radiation: Oct 30

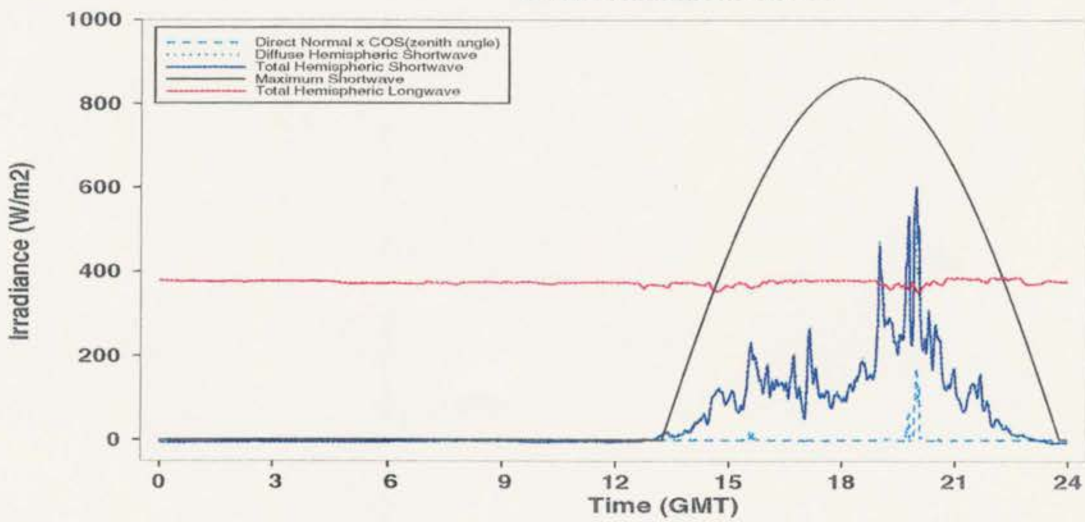

Clouds: October 31

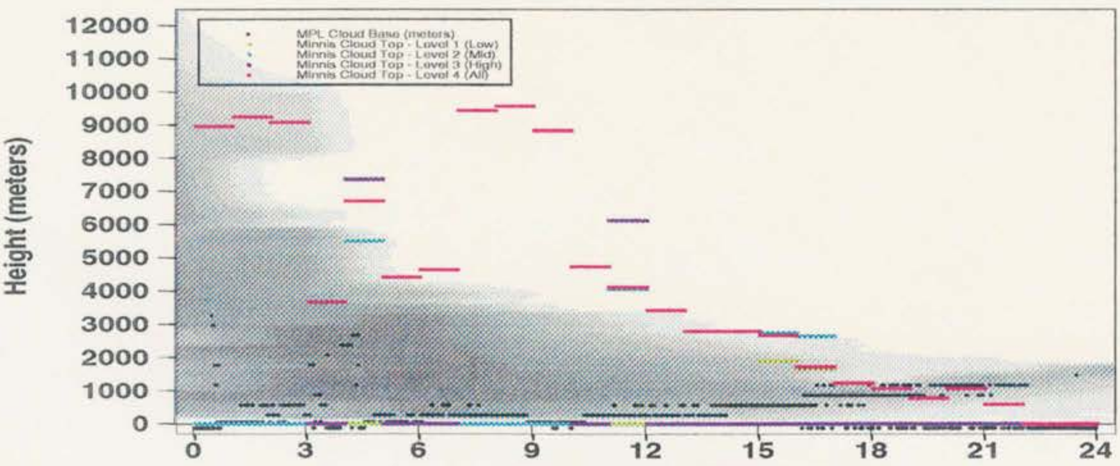

MWR: 31 October

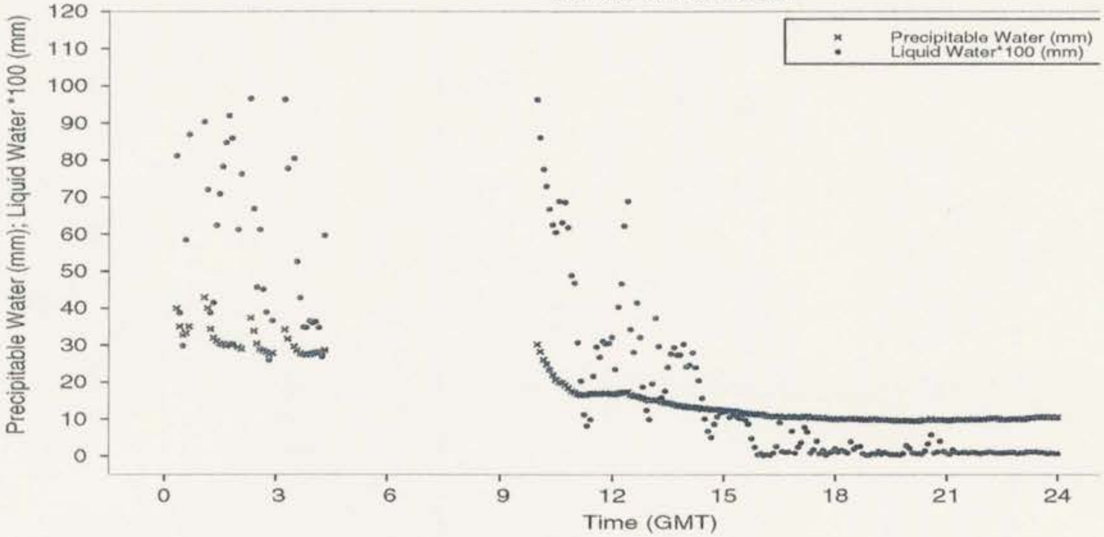

BSRN Radiation: Oct 31

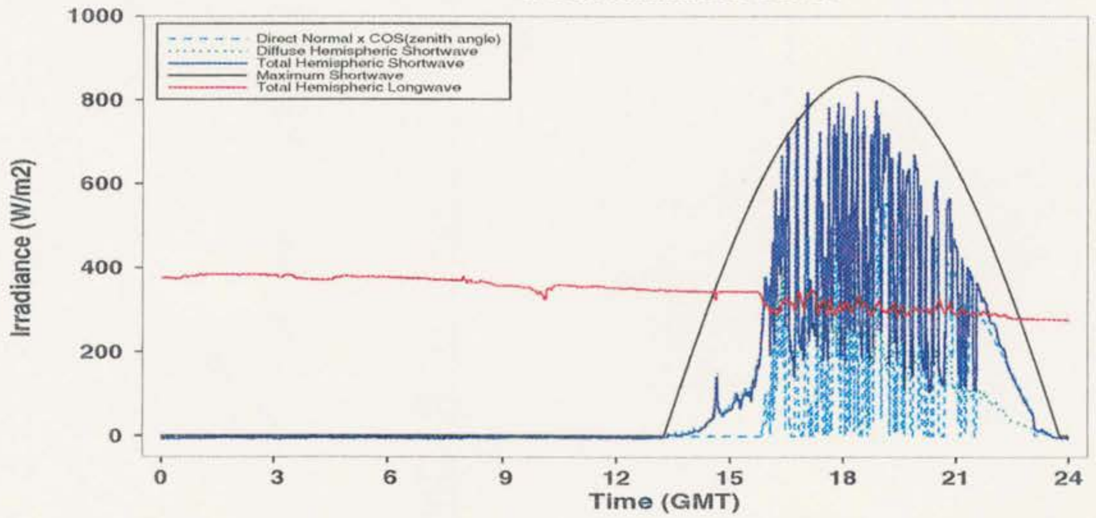

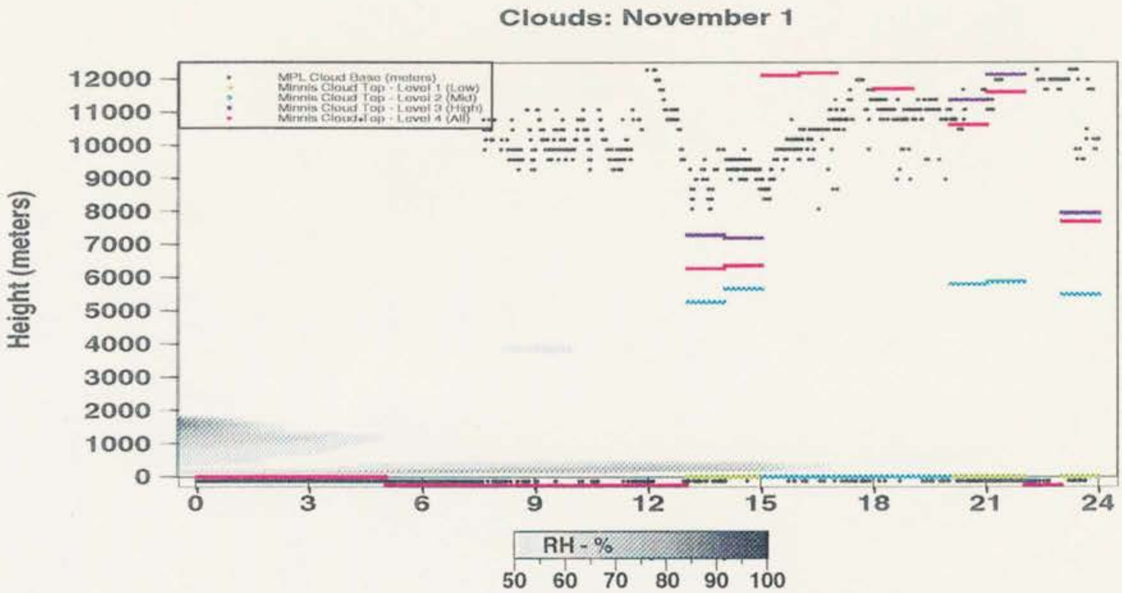
Clouds: November 1
Height (meters)
MPL Cloud Base (meters)
Minnis Cloud Top - Level 1 (Low)
Minnis Cloud Top - Level 2 (Mid)
Minnis Cloud Top - Level 3 (High)
Minnis Cloud Top - Level 4 (All)
RH - %
50 60 70 80 90 100

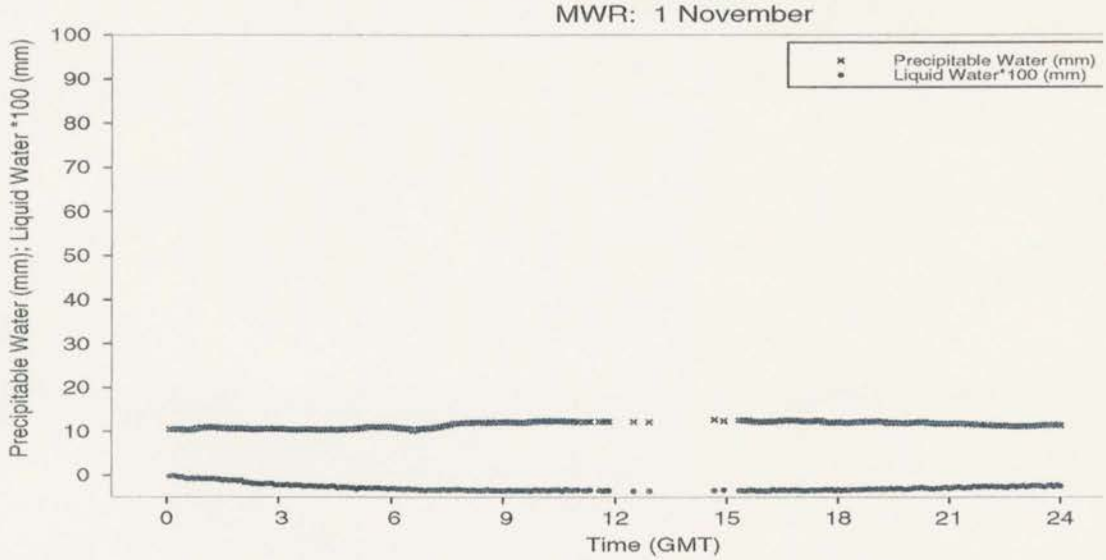
MWR: 1 November
Precipitable Water (mm); Liquid Water *100 (mm)
Precipitable Water (mm)
Liquid Water*100 (mm)
Time (GMT)

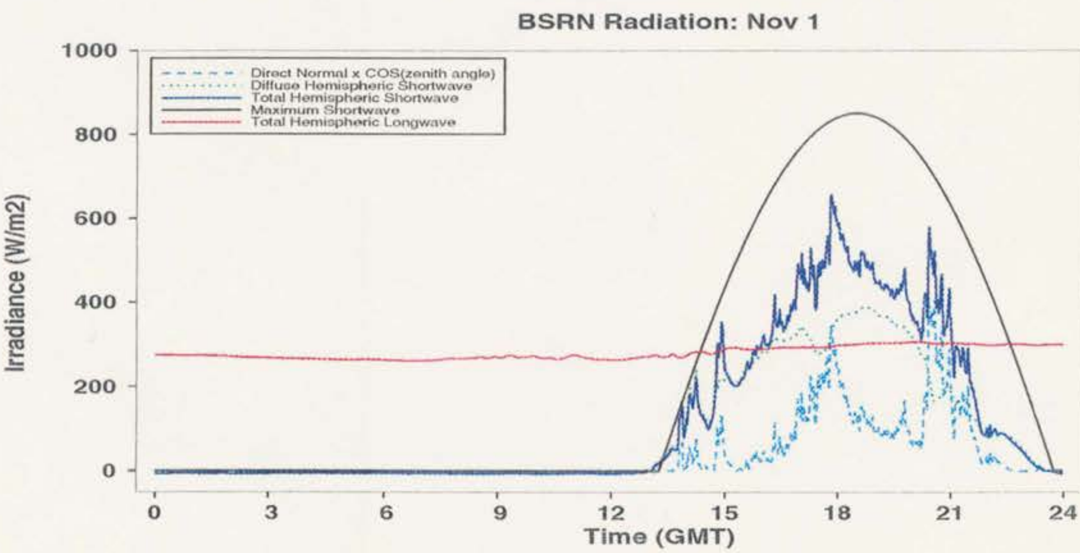
BSRN Radiation: Nov 1
Irradiance (W/m2)
Direct Normal x COS(zenith angle)
Diffuse Hemispheric Shortwave
Total Hemispheric Shortwave
Maximum Shortwave
Total Hemispheric Longwave
Time (GMT)

Clouds: November 2

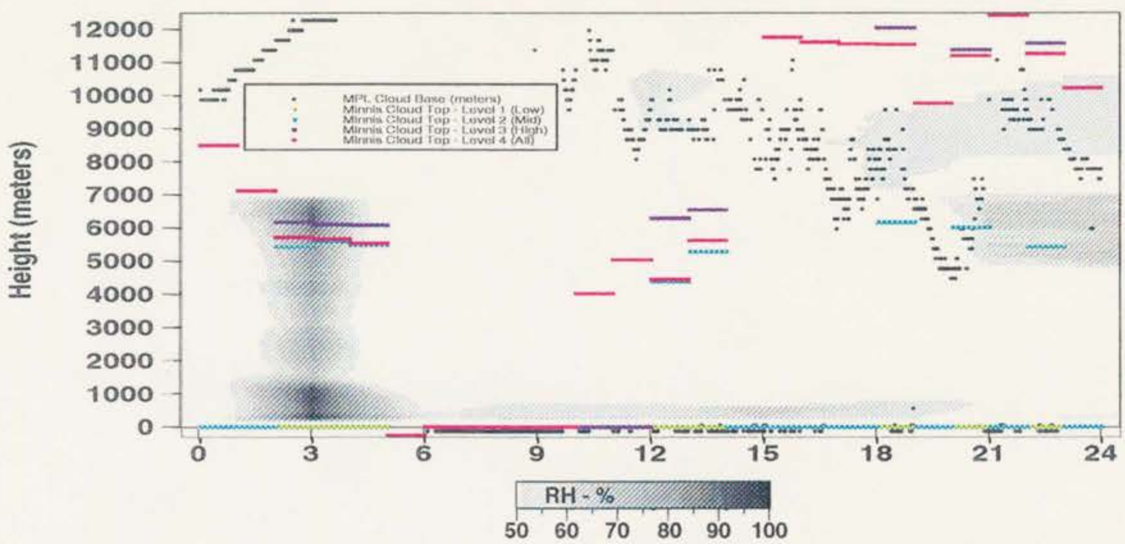

MWR: 2 November

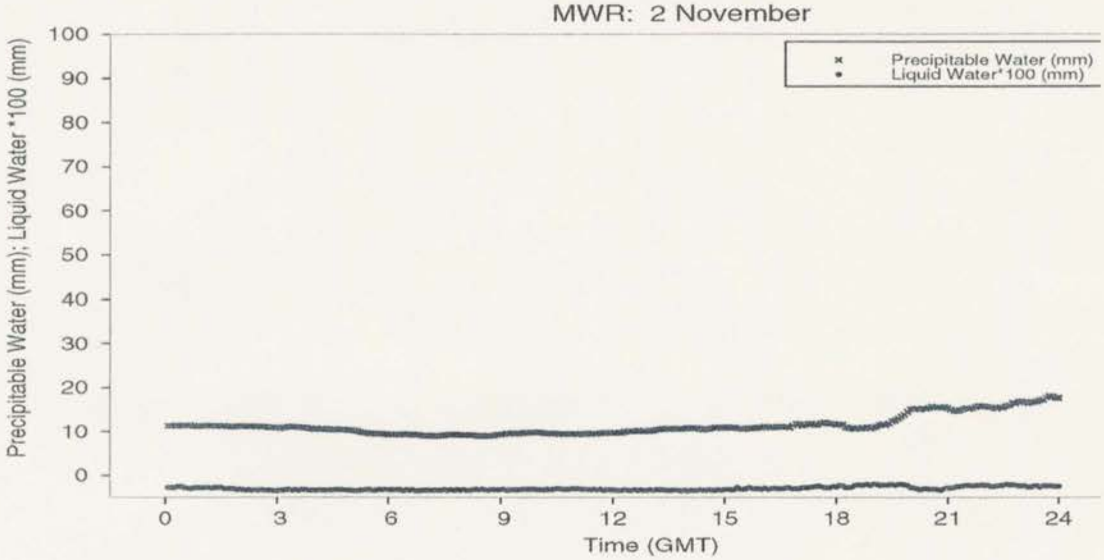

BSRN Radiation: Nov 2

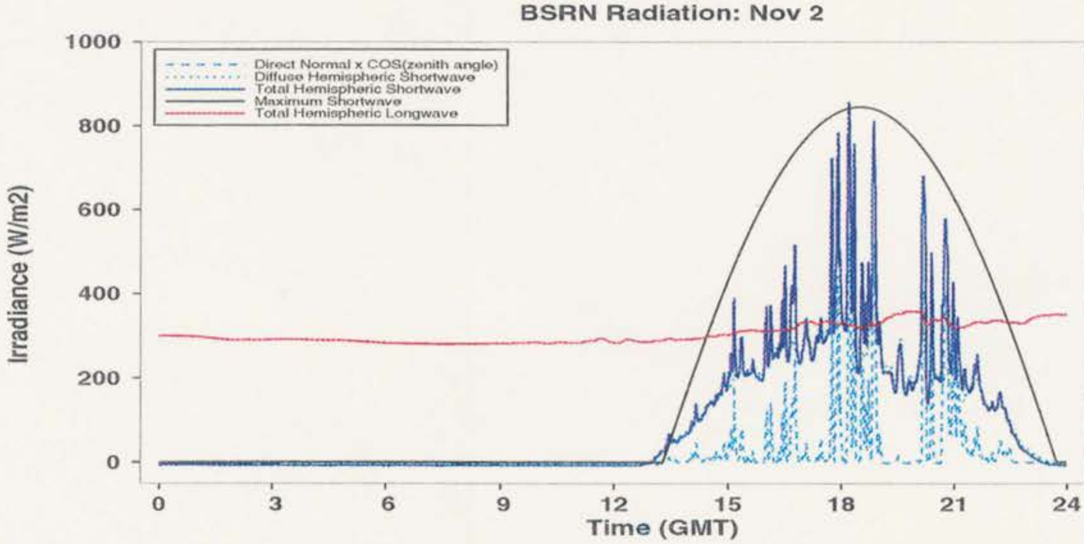

Clouds: November 3

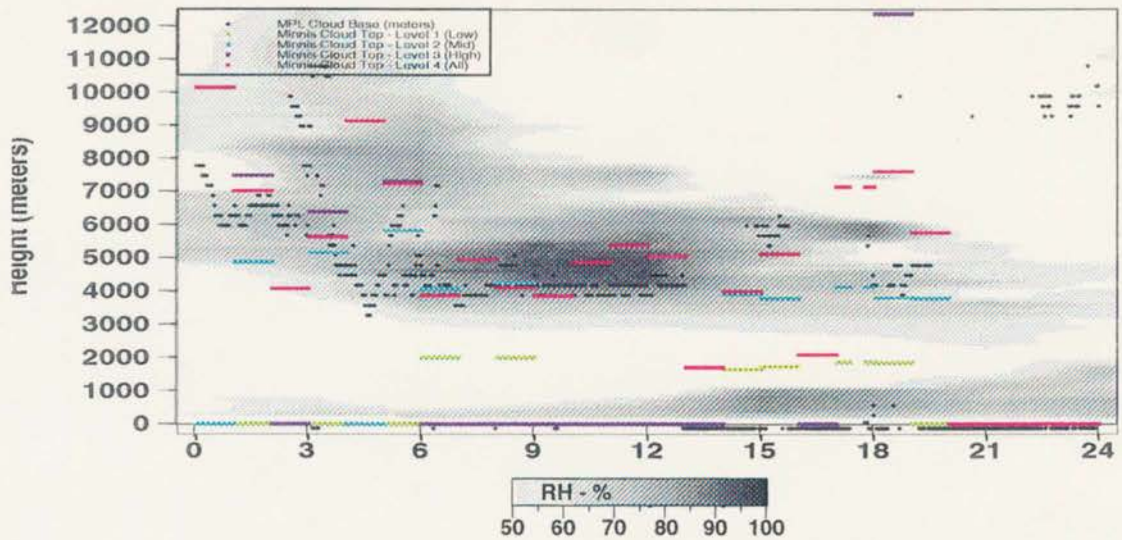

MWR: 2 November

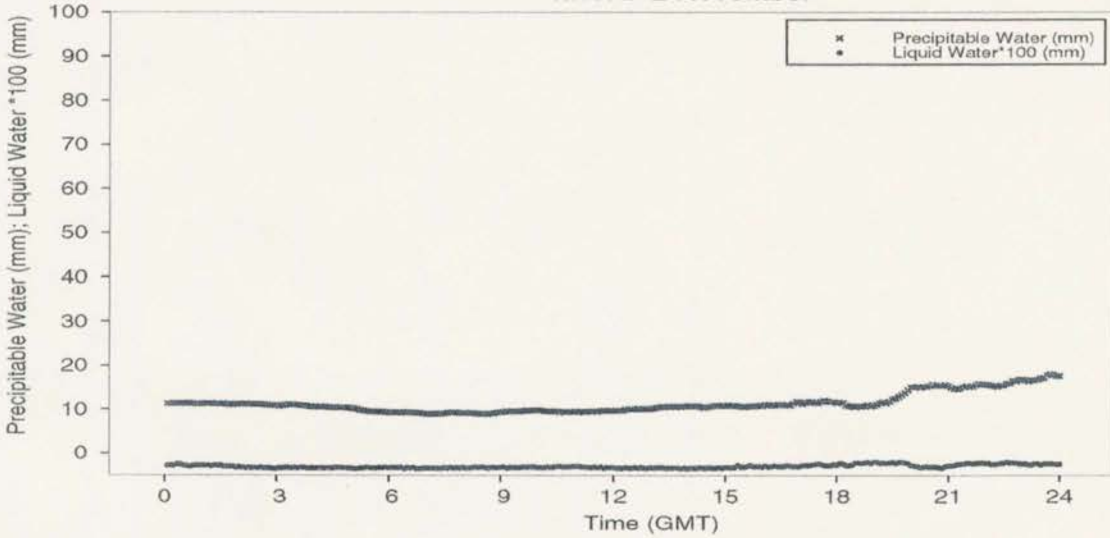

BSRN Radiation: Nov 3

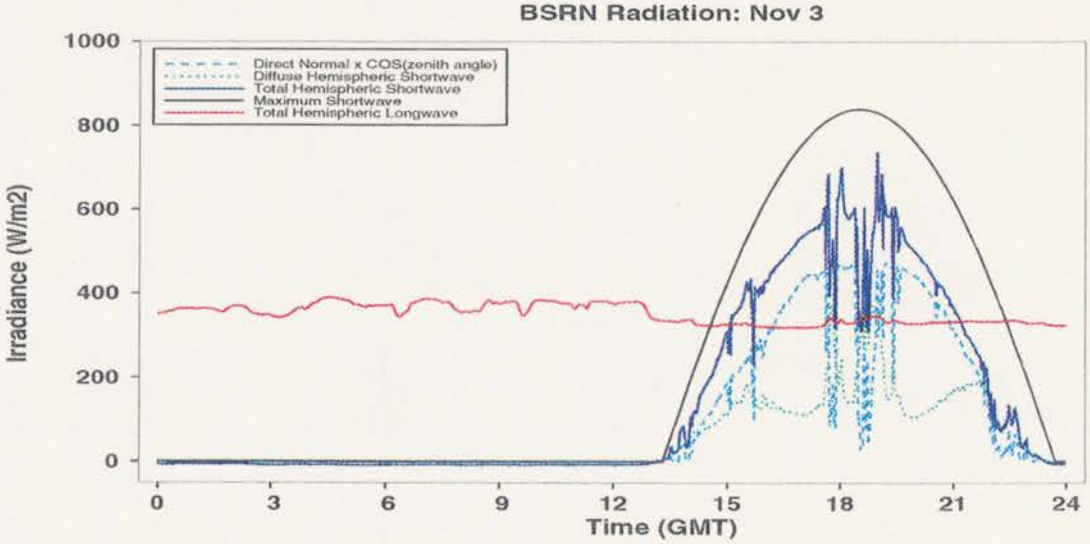

Clouds: November 4

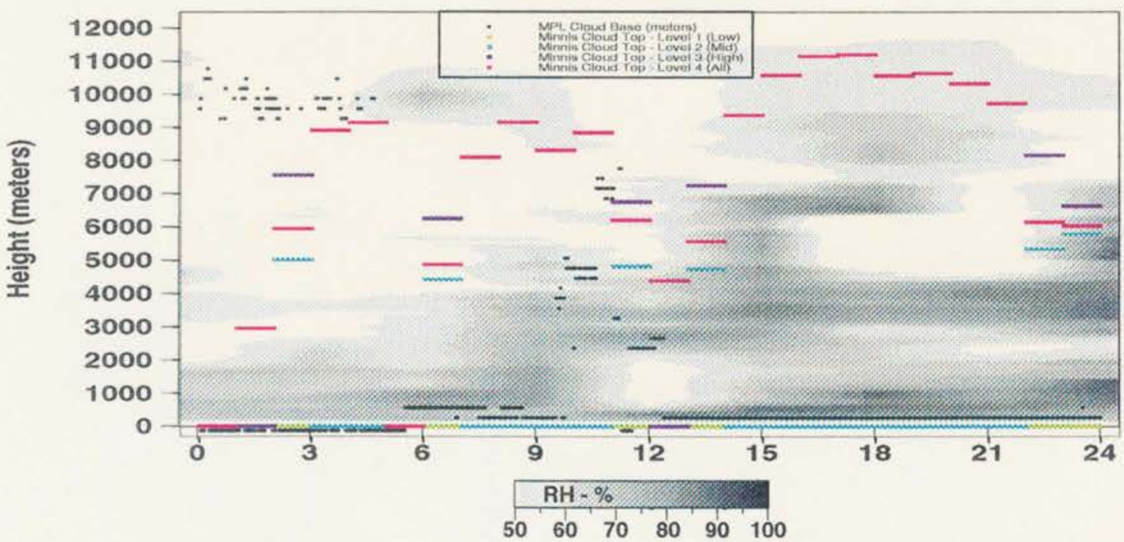

MWR: 4 November

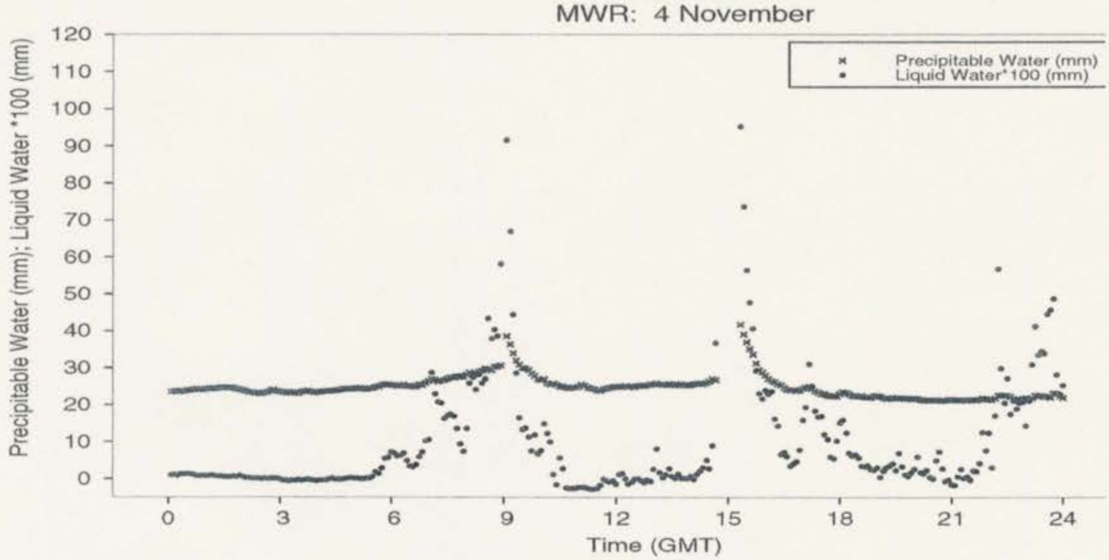

BSRN Radiation: Nov 4

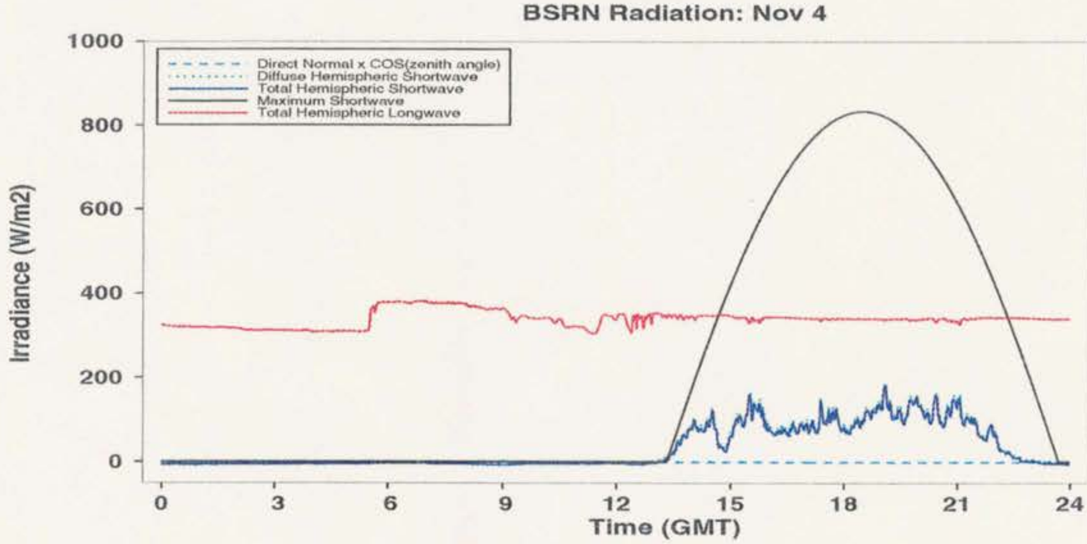

Clouds: November 5

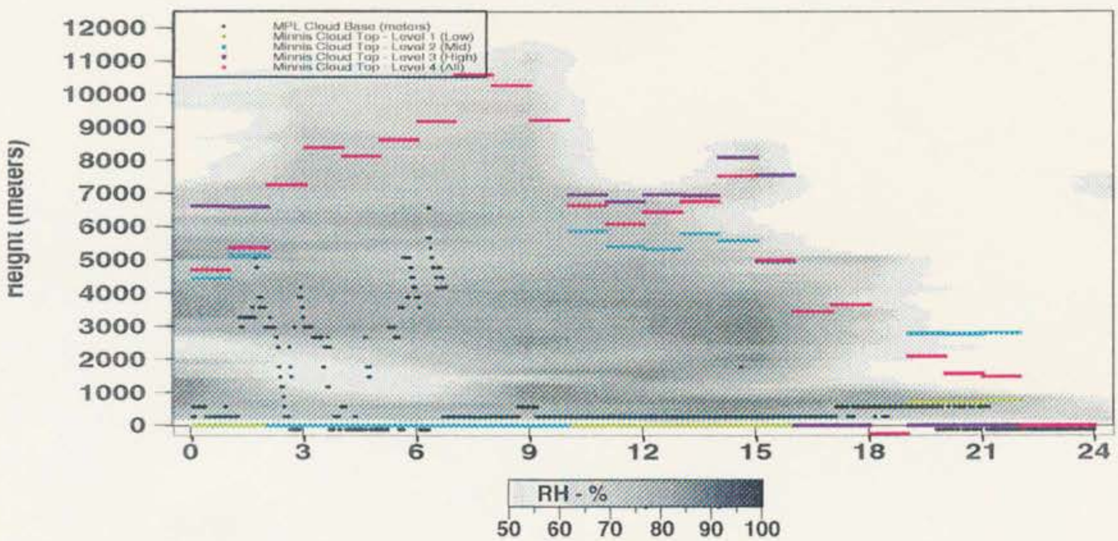

MWR: 5 November

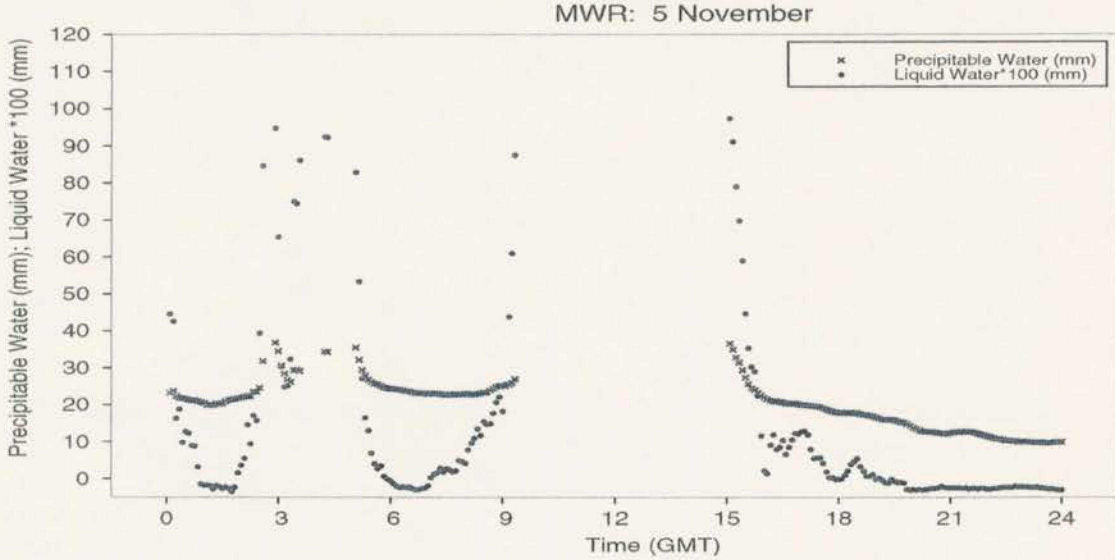

BSRN Radiation: Nov 5

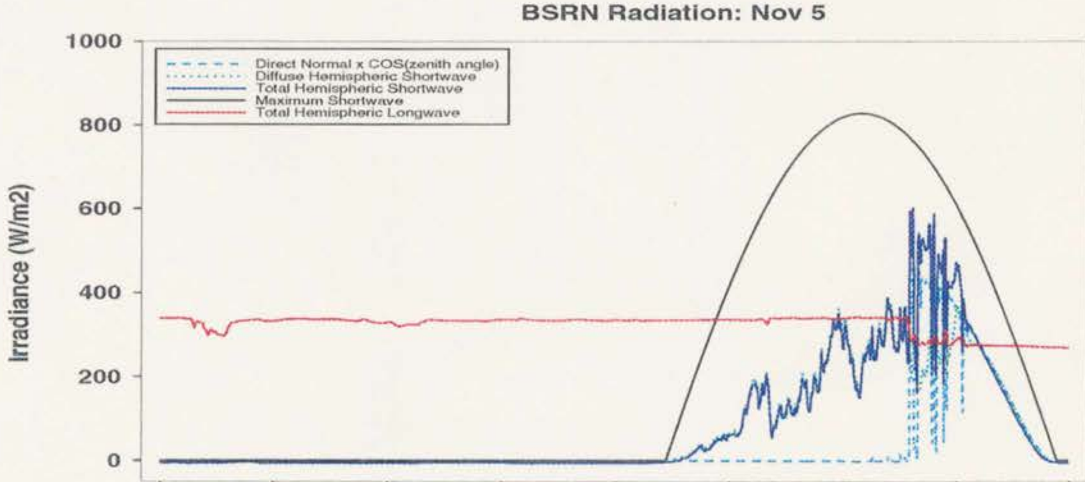

Clouds: November 6

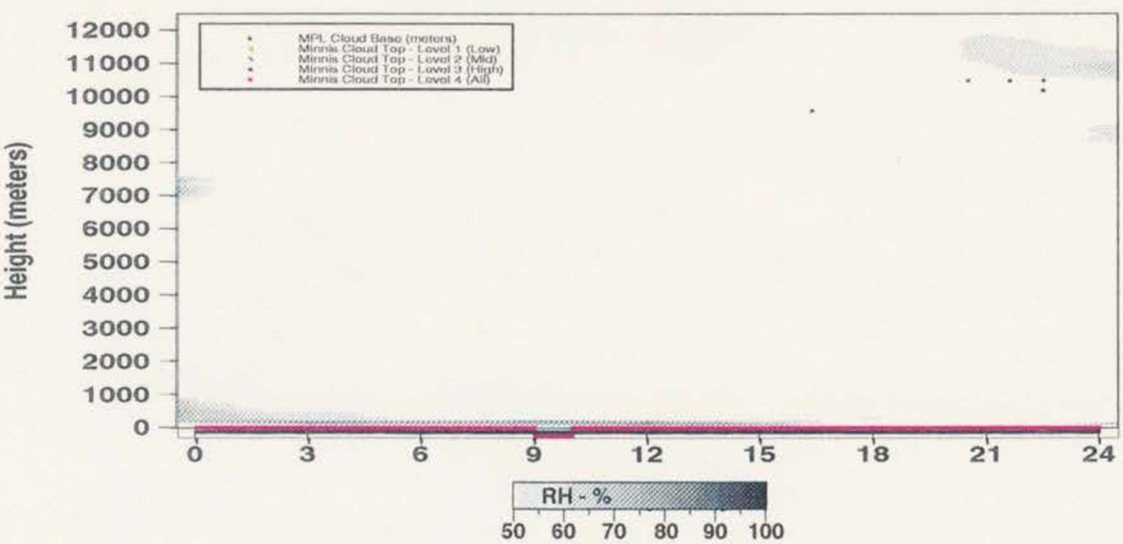

MWR: 6 November

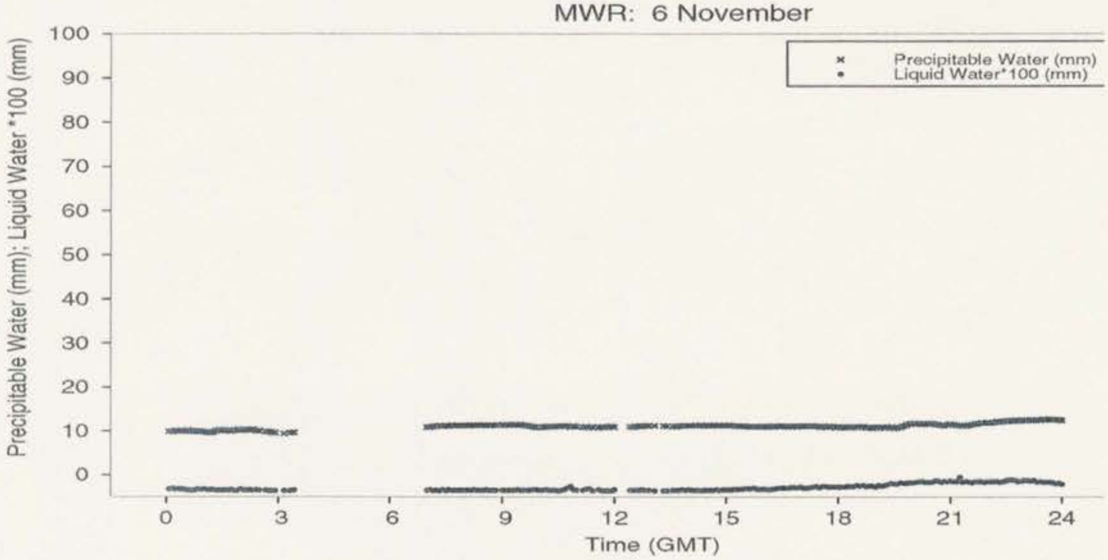

BSRN Radiation: Nov 6

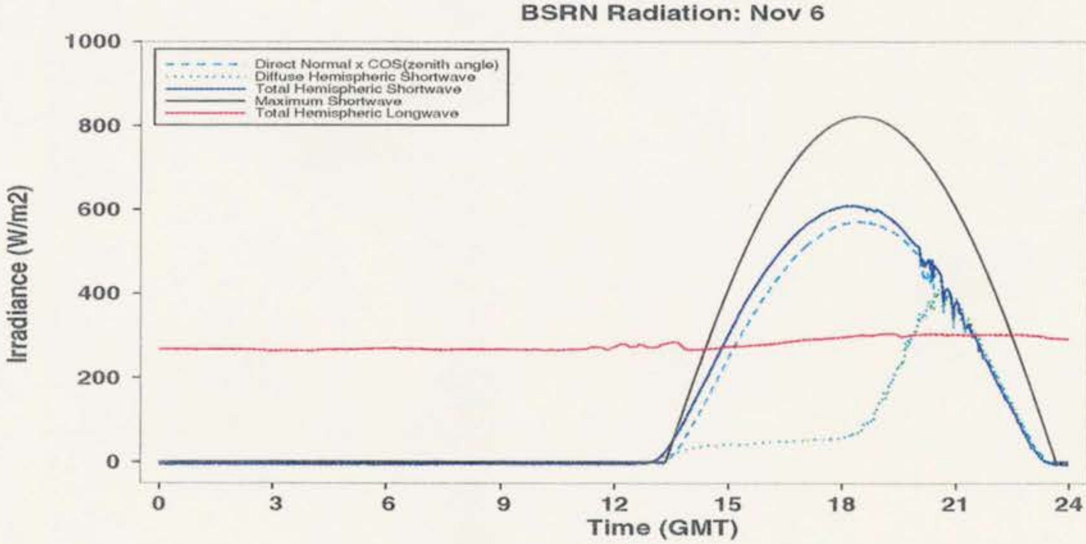

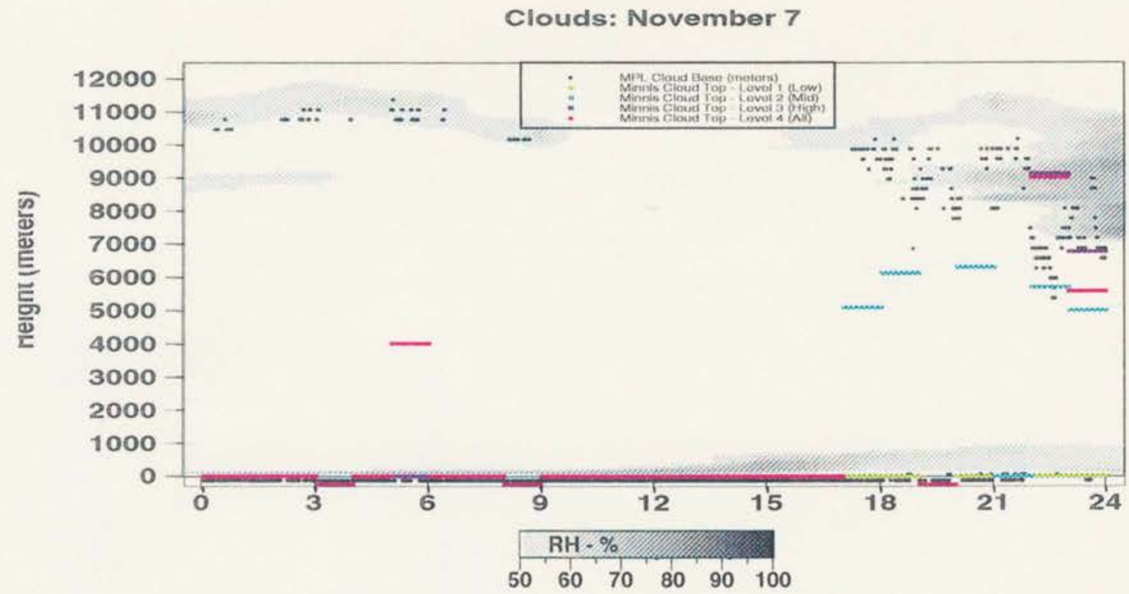
Clouds: November 7
MPL Cloud Base (meters)
Minnis Cloud Top - Level 1 (Low)
Minnis Cloud Top - Level 2 (Mid)
Minnis Cloud Top - Level 3 (High)
Minnis Cloud Top - Level 4 (All)
Height (meters)
RH - %
50 60 70 80 90 100

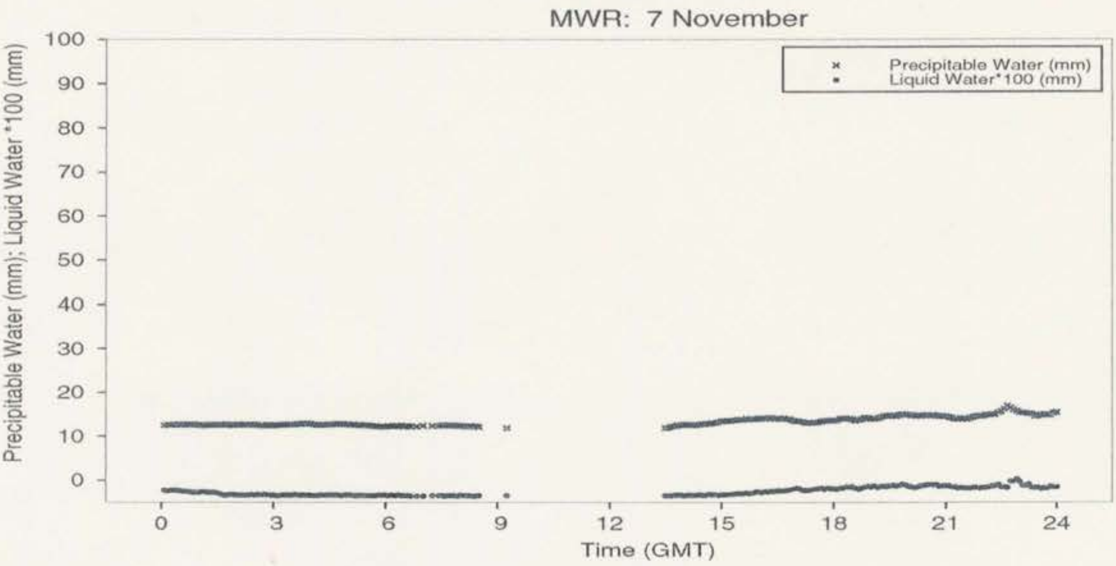
MWR: 7 November
Precipitable Water (mm)
Liquid Water*100 (mm)
Precipitable Water (mm); Liquid Water *100 (mm)
Time (GMT)

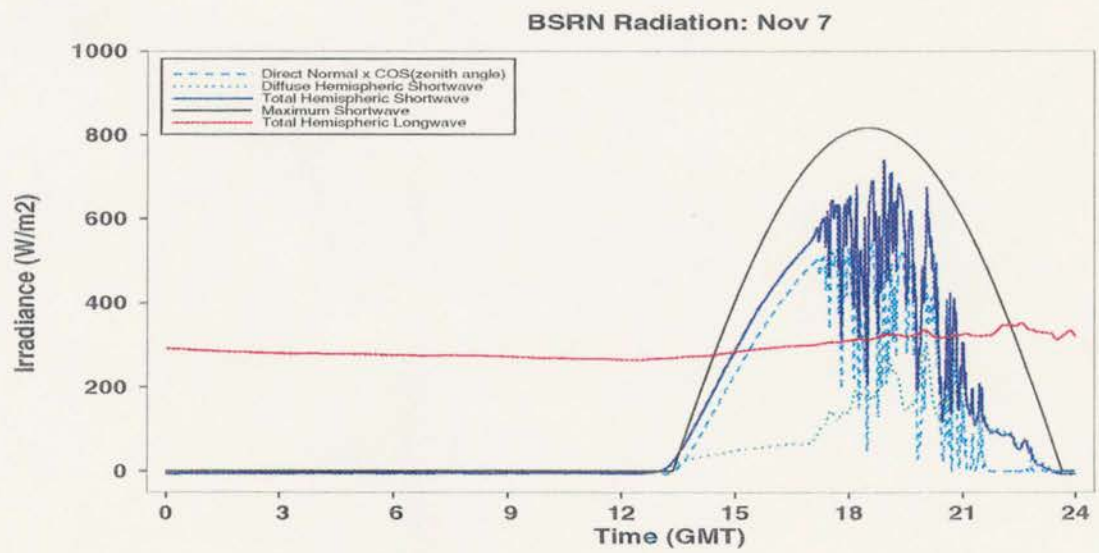
BSRN Radiation: Nov 7
Direct Normal x COS(zenith angle)
Diffuse Hemispheric Shortwave
Total Hemispheric Shortwave
Maximum Shortwave
Total Hemispheric Longwave
Irradiance (W/m2)
Time (GMT)

Clouds: November 8

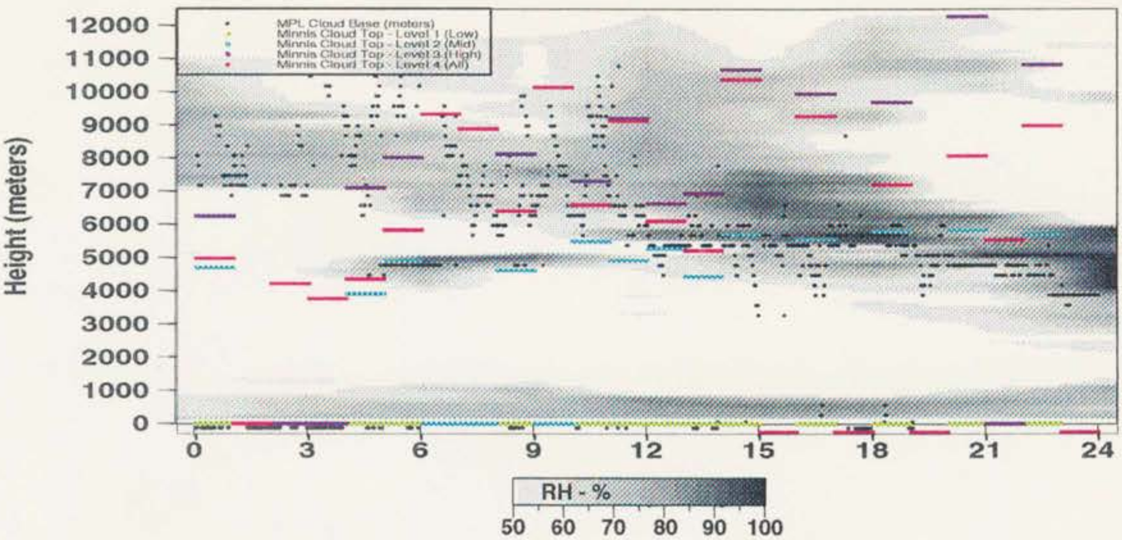

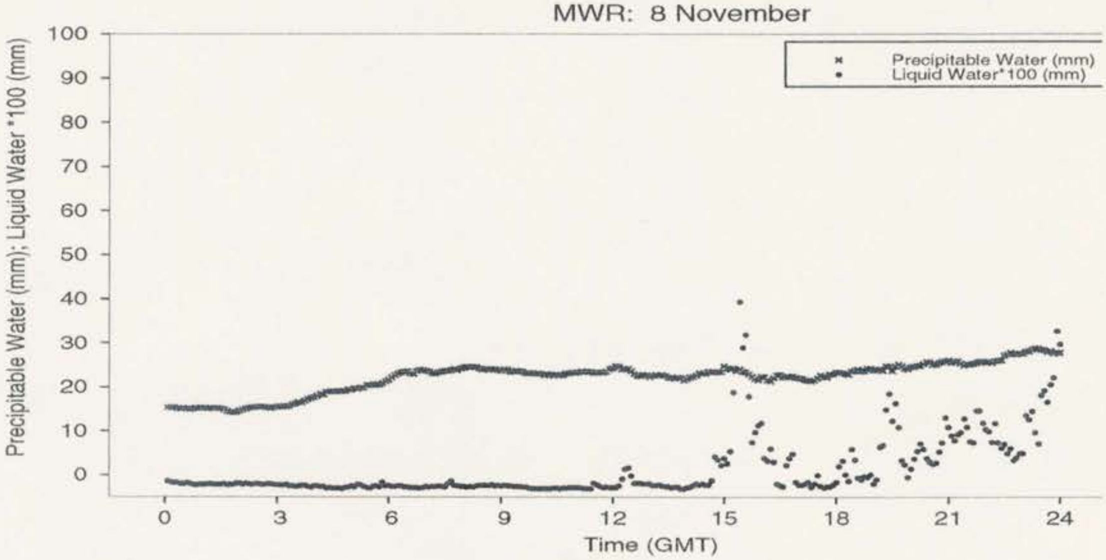

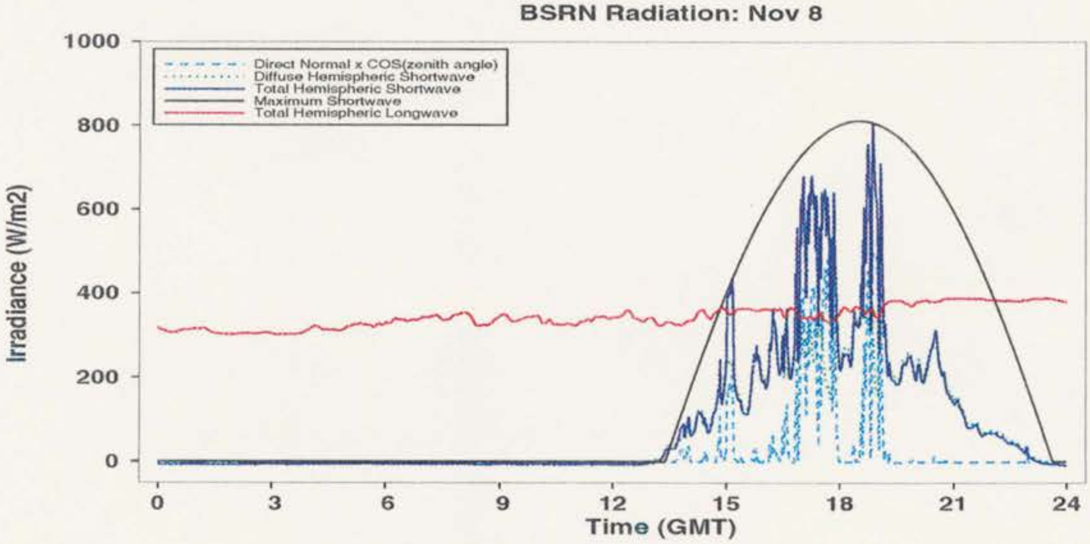

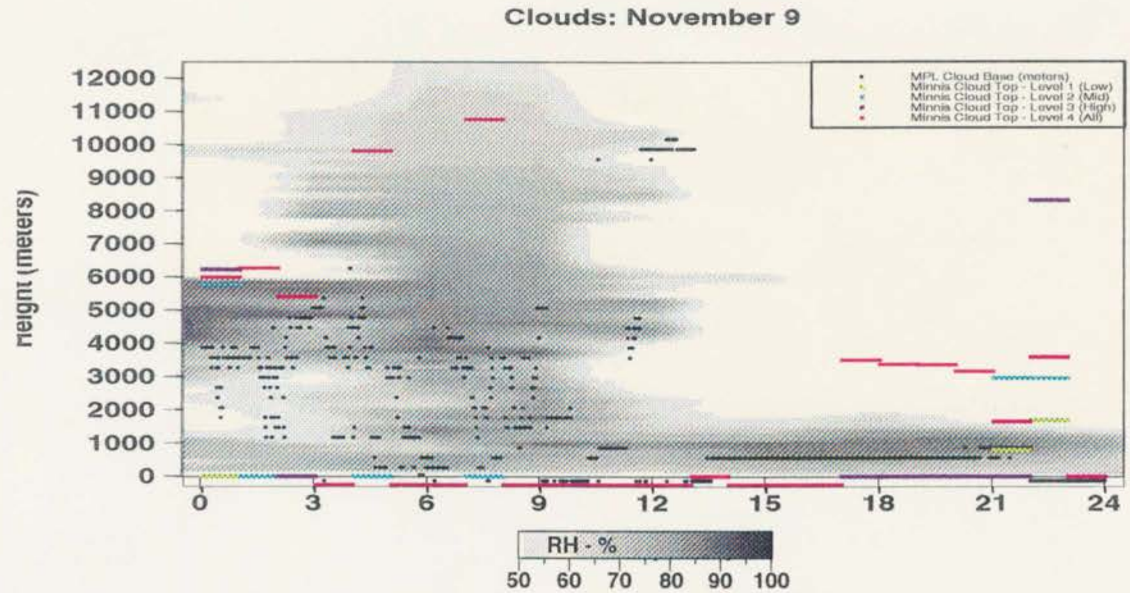
Clouds: November 9
Height (meters)
MPL Cloud Base (meters)
Minnis Cloud Top - Level 1 (Low)
Minnis Cloud Top - Level 2 (Mid)
Minnis Cloud Top - Level 3 (High)
Minnis Cloud Top - Level 4 (All)
RH - %

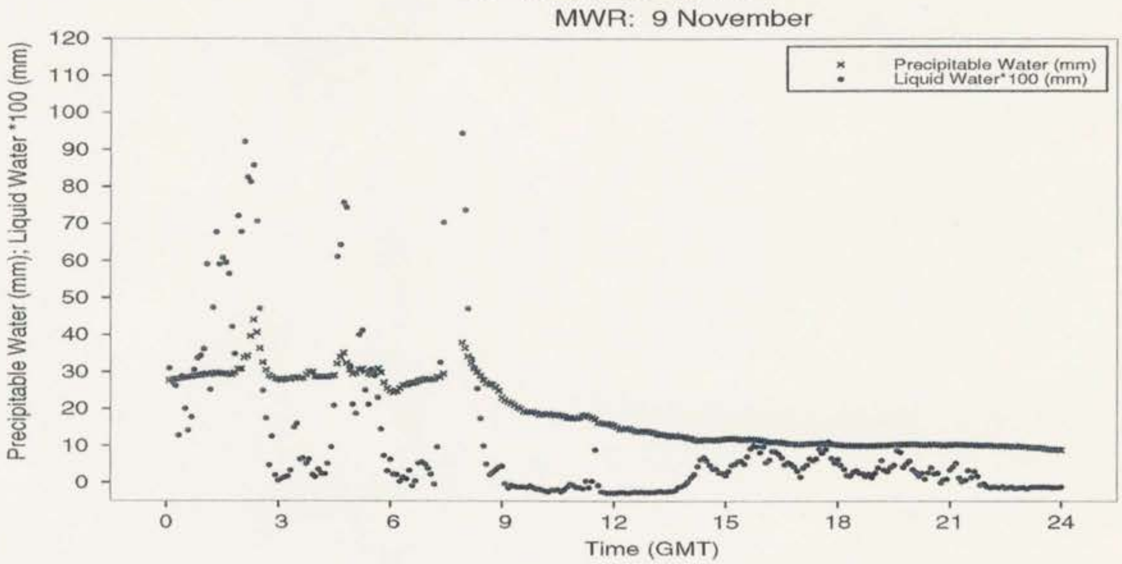
MWR: 9 November
Precipitable Water (mm); Liquid Water *100 (mm)
Precipitable Water (mm)
Liquid Water*100 (mm)
Time (GMT)

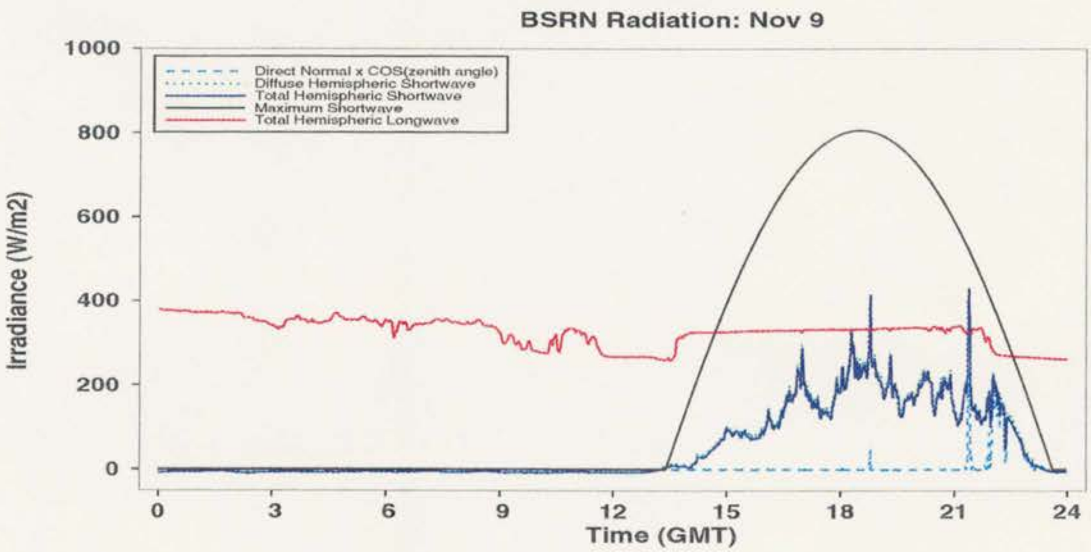
BSRN Radiation: Nov 9
Irradiance (W/m2)
Direct Normal x COS(zenith angle)
Diffuse Hemispheric Shortwave
Total Hemispheric Shortwave
Maximum Shortwave
Total Hemispheric Longwave
Time (GMT)

Clouds: November 10

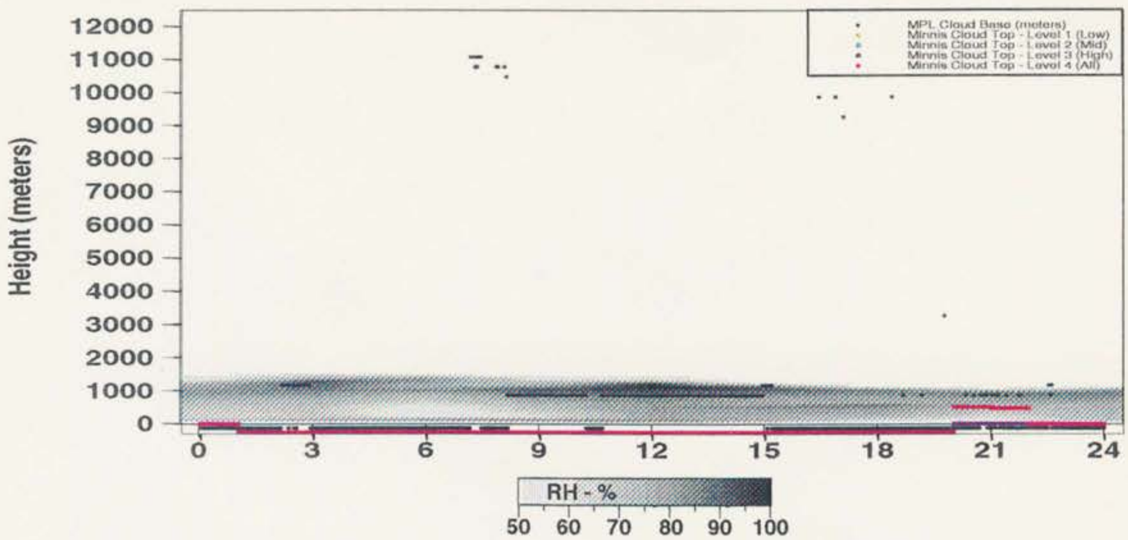

MWR: 10 November

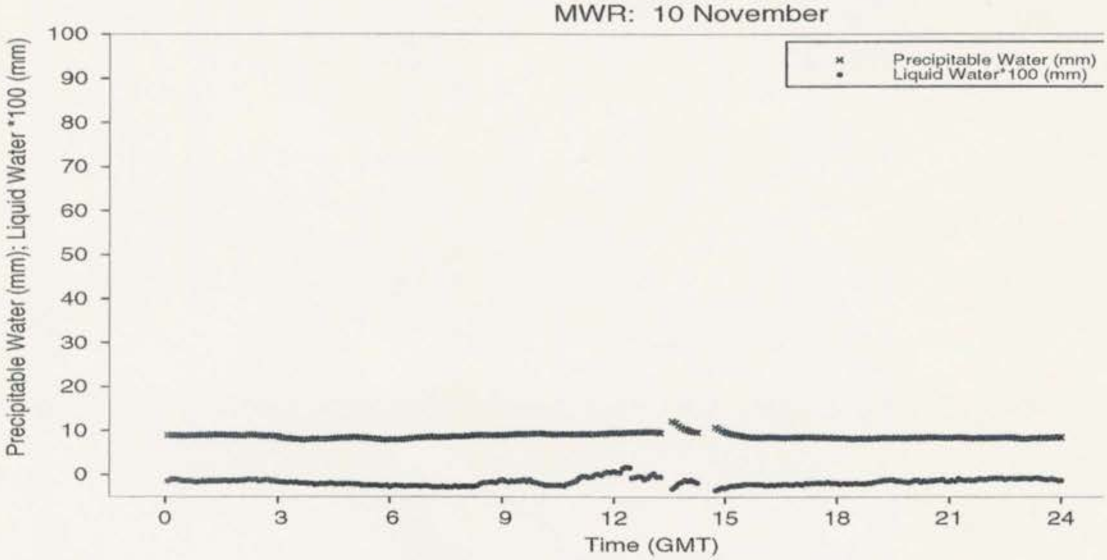

BSRN Radiation: Nov 10

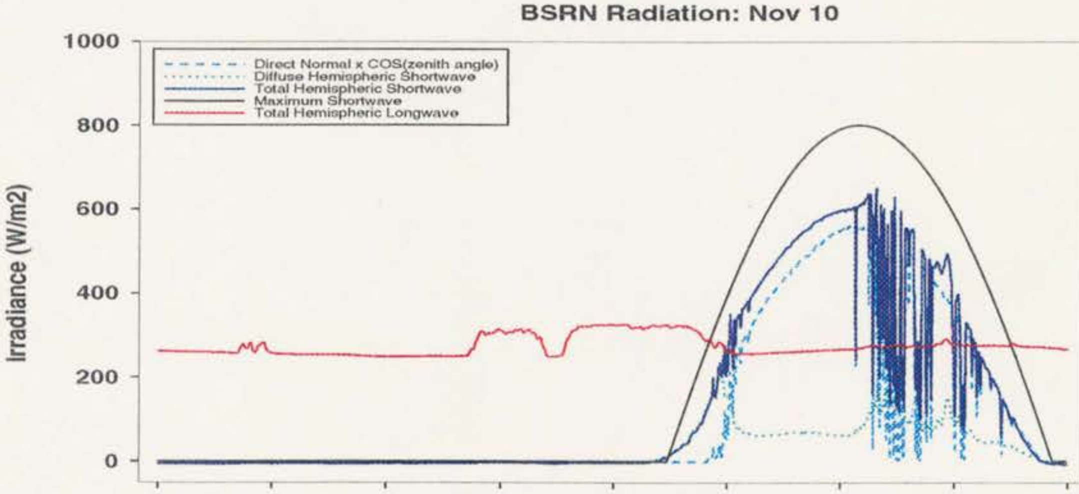

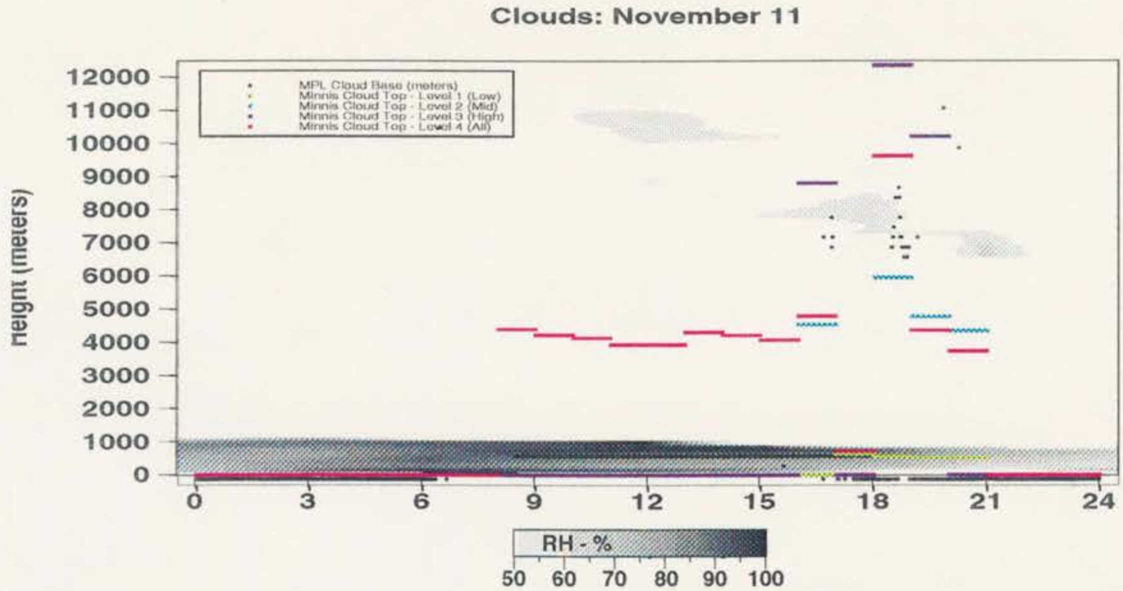
Clouds: November 11
MPL Cloud Base (meters)
Minnis Cloud Top - Level 1 (Low)
Minnis Cloud Top - Level 2 (Mid)
Minnis Cloud Top - Level 3 (High)
Minnis Cloud Top - Level 4 (All)
Height (meters)
RH - %
50 60 70 80 90 100

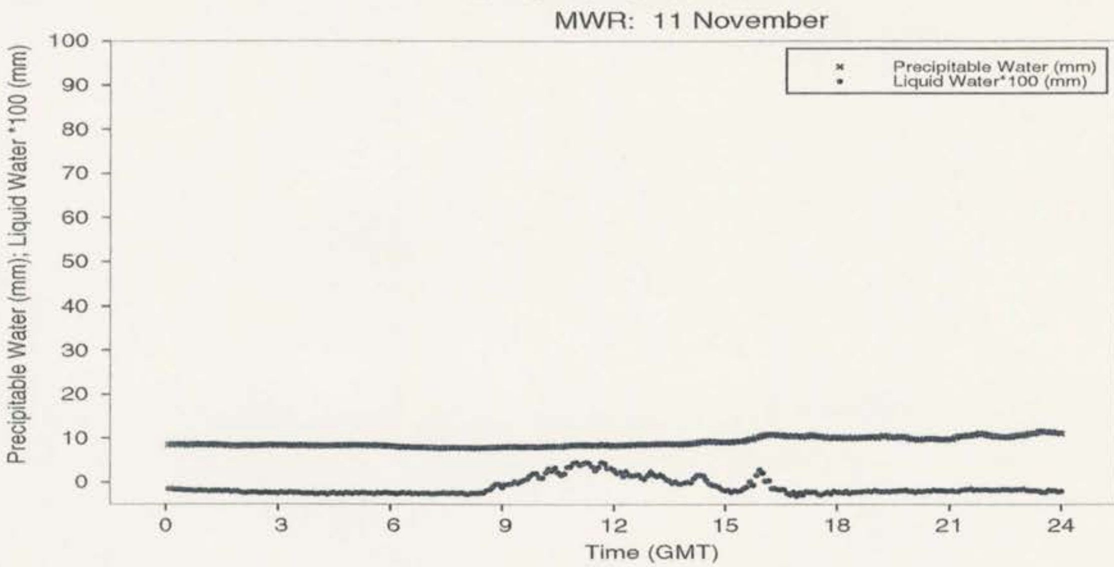
MWR: 11 November
Precipitable Water (mm)
Liquid Water*100 (mm)
Precipitable Water (mm); Liquid Water *100 (mm)
Time (GMT)

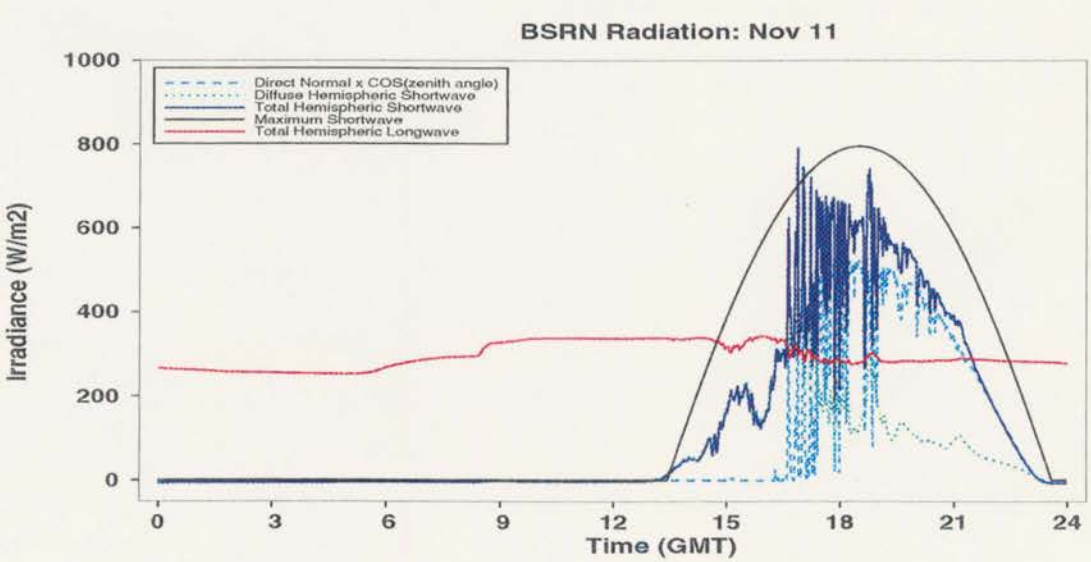
BSRN Radiation: Nov 11
Direct Normal x COS(zenith angle)
Diffuse Hemispheric Shortwave
Total Hemispheric Shortwave
Maximum Shortwave
Total Hemispheric Longwave
Irradiance (W/m2)
Time (GMT)

:

Clouds: November 12

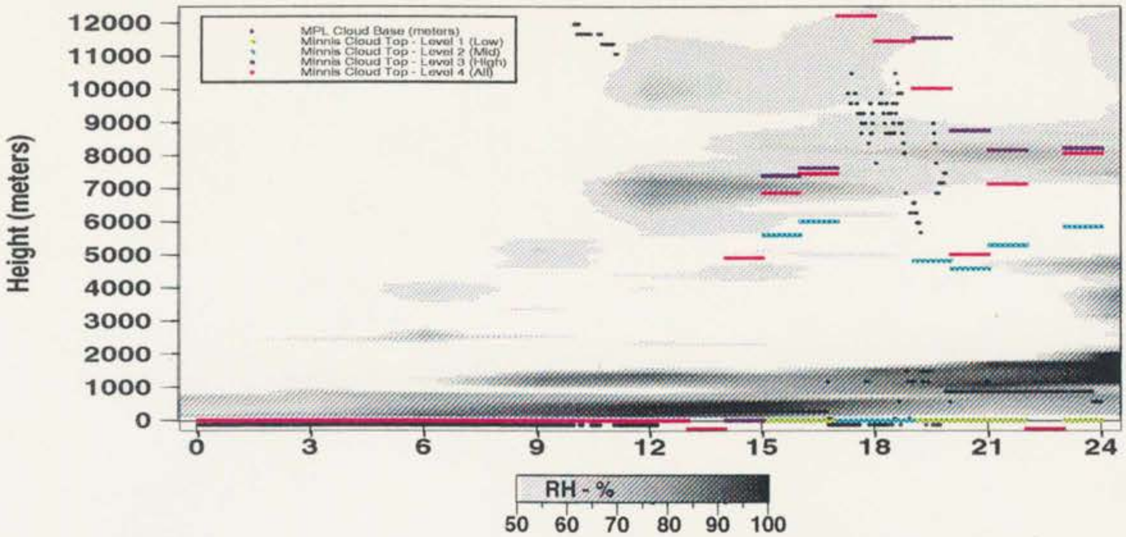

MWR: 12 November

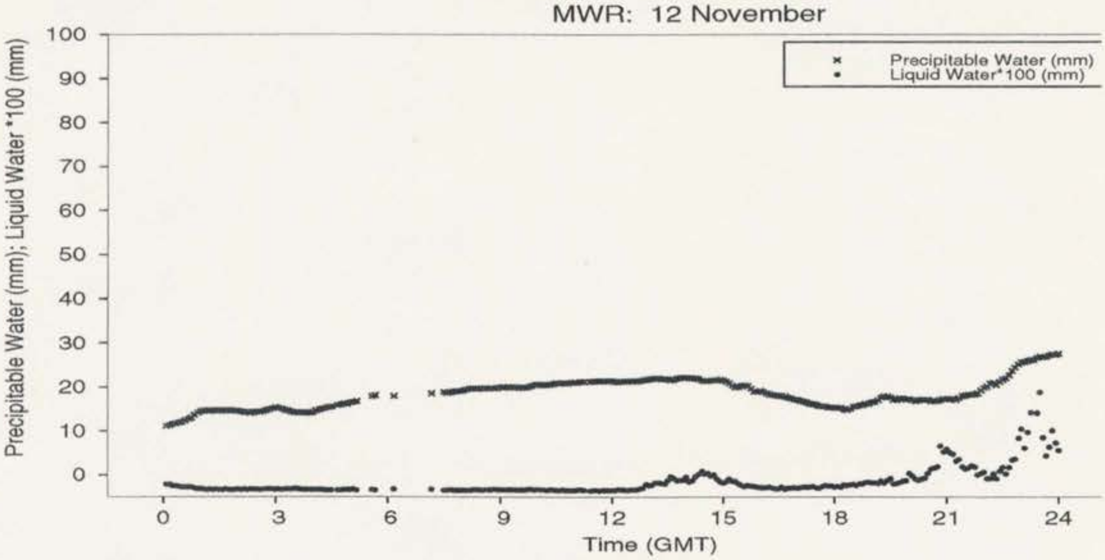

BSRN Radiation: Nov 12

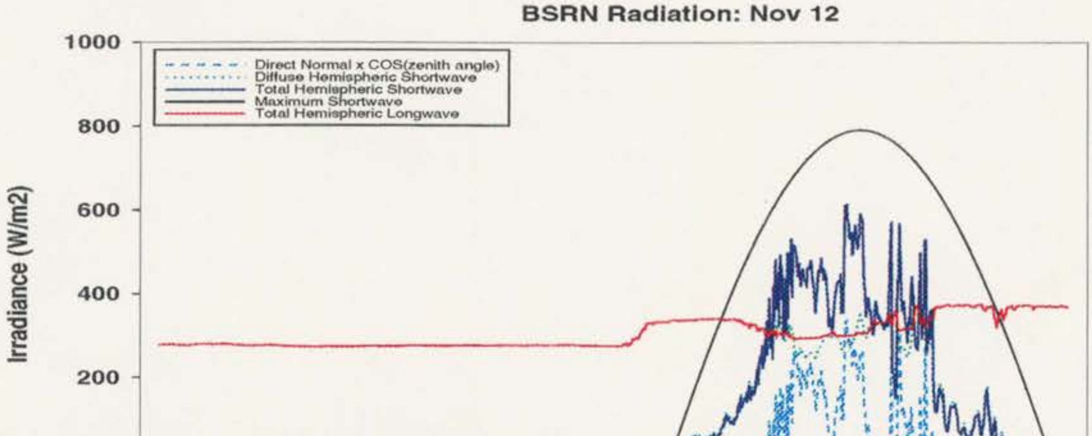

Clouds: November 13

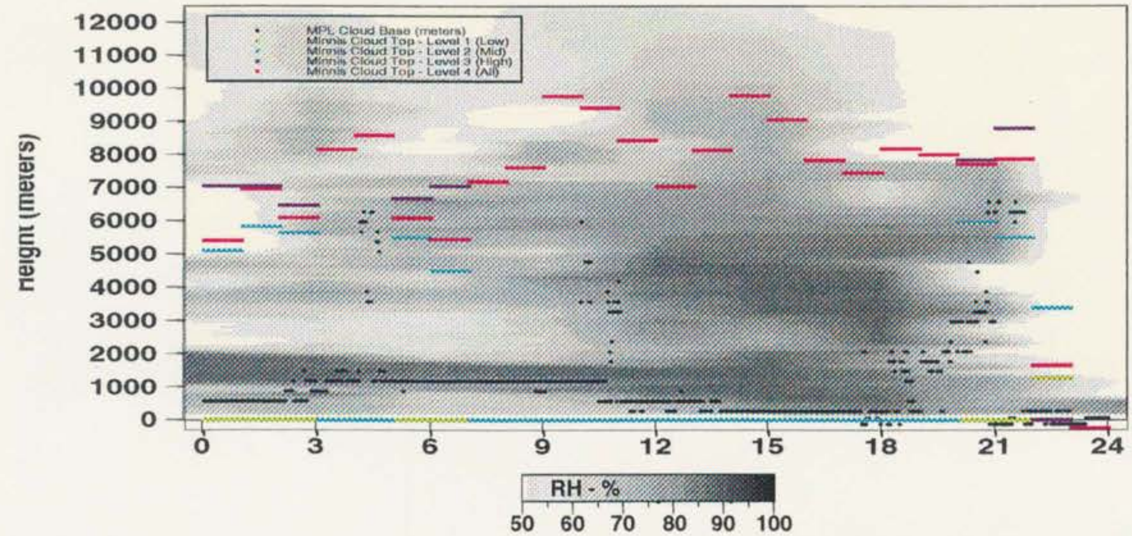

MWR: 13 November

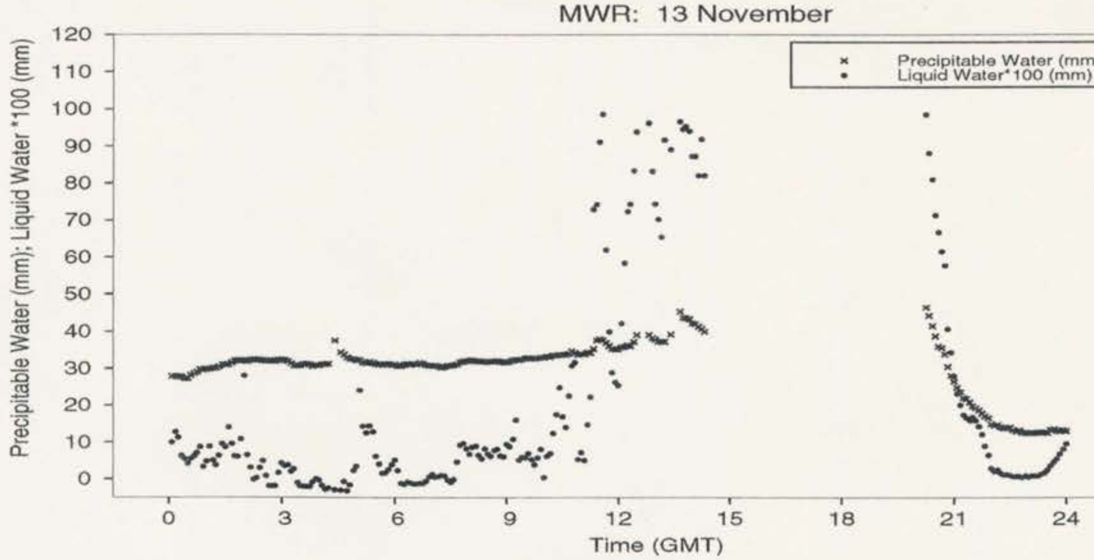

BSRN Radiation: Nov 13

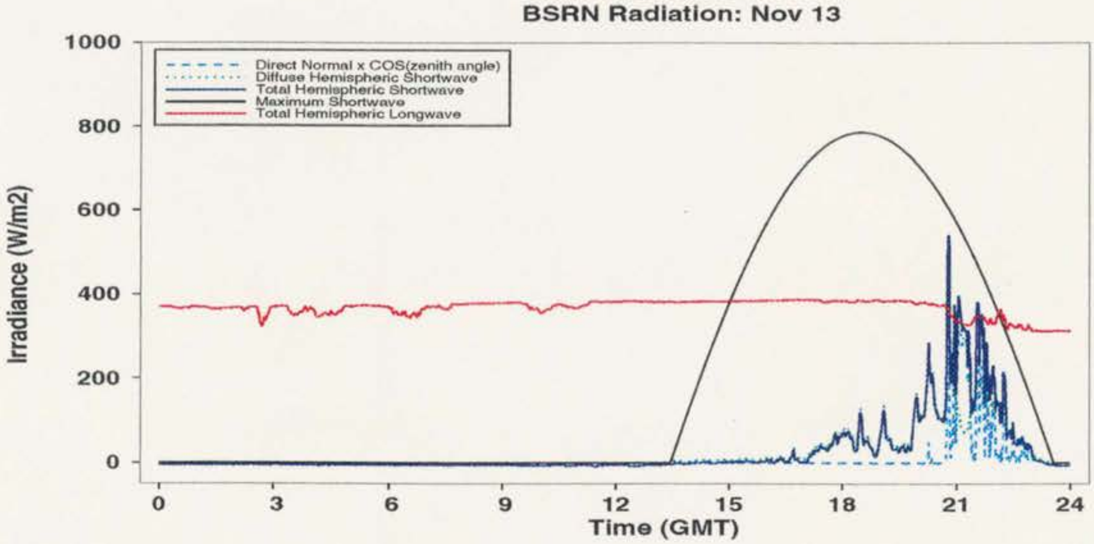

:

Clouds: November 14

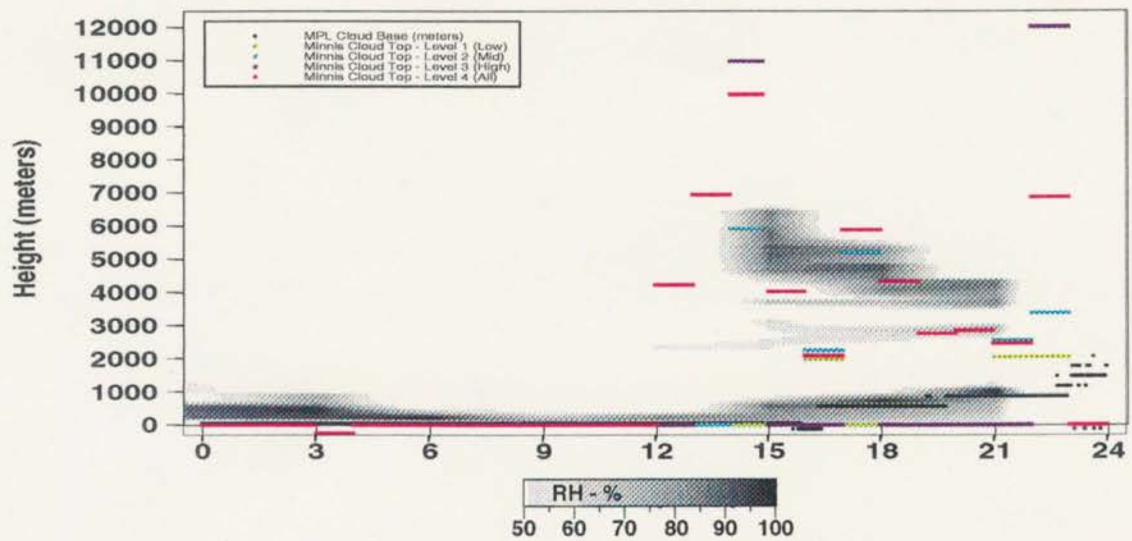

MWR: 14 November

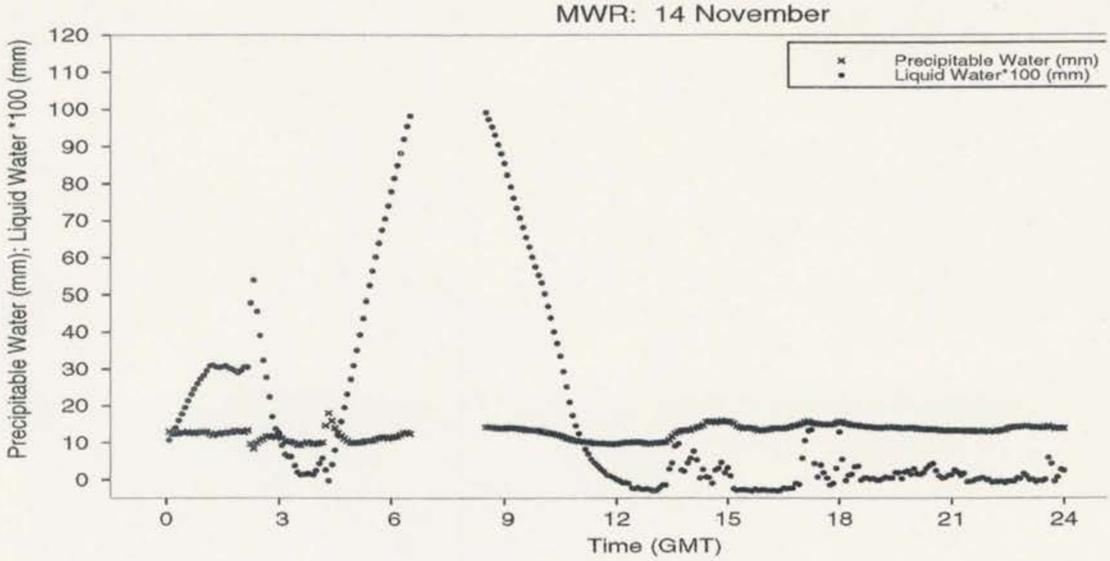

BSRN Radiation: Nov 14

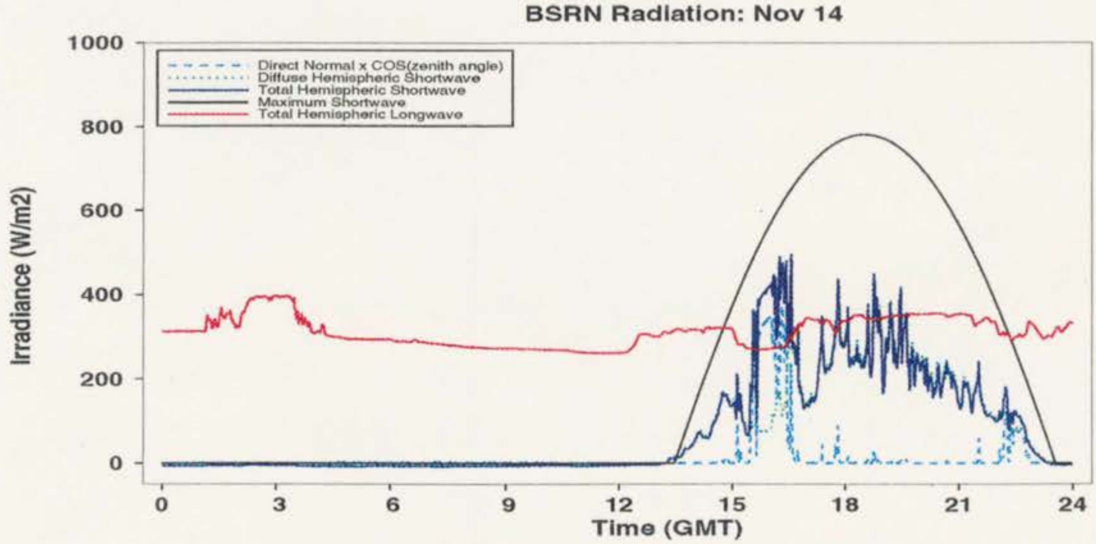

References

The ARM Science Team, 1995. Science Plan for the Atmospheric Radiation Measurement Program (ARM).

Bretherton, C. S., E. Klinker, A.K. Betts and J.A. Coakley, Jr., 1994: Comparison of Ceilometer, Satellite and Synoptic Measurements of Boundary Layer Cloudiness and the ECMWF Diagnostic Cloud Paramaterization Scheme during ASTEX, *J. Atmos. Sci.*.

Briegleb, B.P, P. Minnis, V. Ramanathan, and E. Harrison, 1986: Comparison of Regional Clear-Sky Albedos Inferred from Satellite Observations and Model Computations, *J. Climate Appl. Meteor.*, **25**, 214-226.

Cripe, D. G., 1994: Investigation of GCAPE Quasi-Equilibrium in the Midlatitudes. Colorado State Department of Atmospheric Science Paper No. 568, 221 pages.

Dowling, D. R. and L.F. Radke, 1990: A Summary of the Physical Properties of Cirrus Clouds, *J. Appl. Meteor.*, **29**, 970-978.

Fowler, L. D. and D.A. Randall, 1996: Liquid and Ice Cloud Microphysics in the CSU General Circulation Model. Part III: Sensitivity to Modeling Assumptions, *J. Climate*, **9**, 561-586.

Goody, R.M. and Y.L. Yung, 1989. *Atmospheric Radiation, Theoretical Basis*. Oxford University Press, New York, 520 pages.

Harshvardhan, R. Davies, D. A. Randall and T. G. Corsetti, 1987: A fast radiation parameterization for atmospheric circulation models. *J. Geophys. Res.*, **92**, 1009-1016.

Heymsfield, A.J. and C.M. Platt, 1984. A Parameterization of the Particle Size Spectrum of Ice Clouds in Terms of the Ambient Temperature and the Ice Water Content, *J. Atmos. Sci.*, **41**, 846-855.

:

Levy, R., D. Randall and W. Schubert, 1993: An Overview of the ASTEX Data Collected at Porto Santo, Colorado State Department of Atmospheric Science Paper No. 539, 58 pages.

Liou, Kuo-Nan, 1986: REVIEW: Influence of Cirrus Clouds on Weather and Climate Processes: A Global Perspective, *Mon. Wea. Rev.*, **114**, 1167-1197.

Minnis, P., W. L. Smith, Jr., D. P. Garber, J. K. Ayers, and D. R. Doelling, 1995: Cloud Properties Derived From GOES-7 for Spring 1994 ARM Intensive Observing Period using version 1.0.0 of ARM Satellite Data Analysis Program. *NASA Reference 1366.* 58 pages.

Peixoto, J.P. and A.H. Oort, 1992: *Physics of Climate*. American Institute of Physics, New York, 520 pages.

Platt, C.M. et. al., 1994: The Experimental Cloud Lidar Pilot Study (ECLIPS) for Cloud-Radiation Research, *Bull. Amer. Meteor. Soc.*, **75**, 1635-1654.

Platt, C.M. and Harshvardhan, 1988: Temperature Dependence of Cirrus Extinction: Implications for Climate Feedback, *J. Geophys. Res.*, **93**, 11051-11058.

Randall, D. A., 1989: Cloud Parameterization for Climate Modeling: Status and Prospects, *Atmos. Res.*, **23**, 345-361.

Slingo, A., R. Brown and C.L. Wrench, 1982: A field study of nocturnal stratocumulus; III. High resolution radiative and microphysical observations, *Quart. J. R. Met. Soc.*, **108**, 145-165.

Stackhouse, P., W, and G. Stephens, 1991: A Theoretical and Observational Study of the Radiative Properties of Cirrus: Results from FIRE 1986, *J. Atmos. Sci.*, **48**, 2045-2059.

Stephens, G.L., 1978: Radiation Profiles in Extended Water Clouds II: Parameterization Schemes, *J. Atmos. Sci.*, **35**, 2123-2132.

Stephens, G. L., 1984: REVIEW: The Parameterization of Radiaton for Numerical Weather Prediction and Climate Models, *Mon. Wea. Rev.*, **112**, 826-867.

Splitt, M. E., P. J. Lamb and D. L. Sisterson, 1995: Site Scientific Mission Plan for the Southern Great Plains CART Site, July-December, 1995. U.S. Department of Energy, 53 pages.

Stokes, G. M. and S. E. Schwartz, 1994: The Atmopsheric Radiation Measurement (ARM) Program: Programmatic Background and Design of the Cloud and Radiation Test Bed. *Bull. Amer. Meteor. Soc.*, **75**, 1201-1221

Wallace, J. M. and P.V. Hobbs, 1977: *Atmospheric Science: An Introductory Survey.* Academic Press, New York, 467 pages.